Titre: Title:	Optical Nonlinearities in the Strong Light-Matter Coupling Regime
Auteur: Author:	Fábio Souza Barachati
Date:	2018
Type:	Mémoire ou thèse / Dissertation or Thesis
Référence: Citation:	Souza Barachati, F. (2018). Optical Nonlinearities in the Strong Light-Matter Coupling Regime [Thèse de doctorat, École Polytechnique de Montréal]. PolyPublie. https://publications.polymtl.ca/3717/

URL de PolyPublie: PolyPublie URL:	https://publications.polymtl.ca/3717/
Directeurs de recherche: Advisors:	Stéphane Kéna-Cohen
Programme: Program:	Génie physique

UNIVERSITÉ DE MONTRÉAL

OPTICAL NONLINEARITIES IN THE STRONG LIGHT-MATTER COUPLING REGIME

FÁBIO SOUZA BARACHATI
DÉPARTEMENT DE GÉNIE PHYSIQUE
ÉCOLE POLYTECHNIQUE DE MONTRÉAL

THÈSE PRÉSENTÉE EN VUE DE L'OBTENTION
DU DIPLÔME DE PHILOSOPHIÆ DOCTOR
(GÉNIE PHYSIQUE)
NOVEMBRE 2018

UNIVERSITÉ DE MONTRÉAL

ÉCOLE POLYTECHNIQUE DE MONTRÉAL

Cette thèse intitulée :

OPTICAL NONLINEARITIES IN THE STRONG LIGHT-MATTER COUPLING REGIME

présentée par : SOUZA BARACHATI Fábio
en vue de l'obtention du diplôme de : Philosophiæ Doctor
a été dûment acceptée par le jury d'examen constitué de :

M. FRANCOEUR Sébastien, Ph. D., président
M. KÉNA-COHEN Stéphane, Ph. D., membre et directeur de recherche
M. SELETSKIY Denis, Ph. D., membre
M. RAZZARI Luca, Ph. D., membre externe

ACKNOWLEDGEMENTS

First and foremost I would like to thank my thesis adviser Prof. Stéphane Kéna-Cohen for giving me the opportunity to join his research group at Polytechnique Montréal. Thank you for your continued support, patience and for sharing your vast knowledge with me.

I would like to thank the Fonds de Recherche du Québec - Nature et Technologies (FRQNT) for the financial support I received through the Merit Scholarship Program for Foreign Students (PBEEE), as well as the Ministère des Relations Internationales et Francophonie for awarding me with a Visiting Researcher grant.

To my colleagues, in particular Aravindan Sridharan, Ashutosh Patri, Elad Eizner, John Ibrahim, Julien Brodeur, Soroush Hafezian and Mohammed Zia Ullah Khan, thank you for your friendship and for making our group a great place to work in. To my collaborators, thank you for sharing your knowledge and expertise with me.

I also owe a big thank you to my friends and family back in Brazil. They have always believed in me much more than I have and I could not have completed my studies without their support. Finally, I would like to thank God for all the amazing opportunities and privileges I have been given.

RÉSUMÉ

Dans le régime linéaire, deux faisceaux lumineux se traversent sans être perturbés. Cependant, en présence de non-linéarités optiques, de nombreux effets technologiquement intéressants peuvent être observés, tels que la génération de nouvelles fréquences optiques et le contrôle d'un faisceau par un autre.

En raison des faibles non-linéarités présentes dans les cristaux optiques, des puissances optiques élevées sont généralement requises pour observer de tels effets non linéaires. Dans certaines applications, telles que la génération de lumière cohérente, le fonctionnement à haute puissance n'est pas problématique. En fait, les techniques de mélange de fréquences et de génération d'harmoniques sont amplement utilisées dans les sources lumineuses commerciales avec des longueurs d'onde d'émission allant de l'ultraviolet profond aux régions infrarouges lointaines du spectre.

Il existe toutefois de nombreuses applications en développement dans lesquelles le fonctionnement à faible consommation est essentiel. Dans le domaine du calcul optique, par exemple, des transistors optiques fonctionnant avec des centaines de photons seulement sont nécessaires pour permettre la fabrication de processeurs optiques plus rapides et plus efficaces que les processeurs électroniques. De tels systèmes bénéficieraient également d'une conversion de fréquence à basse puissance afin d'interfacer les signaux optiques de différentes fréquences sur le même circuit photonique.

Pour que le fonctionnement à faible puissance devienne possible, de très grandes non-linéarités optiques sont nécessaires. Un système dans lequel les non-linéarités optiques sont si fortes que l'arrivée d'un seul photon peut bloquer la transmission d'un autre est celui d'un seul émetteur quantique placé dans une cavité optique de haute qualité. Les principaux inconvénients de tels systèmes sont leur complexité technologique, leur faible évolutivité et leur fonctionnement à des températures cryogéniques.

Dans cette thèse, nous étudions une approche alternative pour améliorer les non-linéarités optiques dans laquelle une collection d'émetteurs est amenée à interagir fortement avec la lumière, créant des quasiparticules lumière-matière appelées exciton-polaritons. Par rapport aux systèmes basés sur des émetteurs uniques, notre approche est plus simple et compatible avec le fonctionnement à température ambiante.

Sous excitation résonnante, les polaritons interagissent fortement par leur composante excitonique et ont permis de mettre en évidence un certain nombre d'effets non linéaires à

température ambiante. Après avoir passé en revue les principales propriétés des excitons-polaritons, nous étudions différentes manières d'utiliser les non-linéarités de polaritons pour le mélange de fréquences et la génération d'harmoniques, ainsi que pour mettre en œuvre de nouveaux dispositifs non linéaires basés sur des fluides de polaritons.

Dans le premier cas, nous considérons des systèmes dans lesquels le matériau excitonique incorporé dans une microcavité plane a une importante non-linéarité optique de second ou de troisième ordre. Nous montrons par des calculs numériques et des expériences que les modes polaritoniques présentent de nombreux avantages pour améliorer l'efficacité de processus non linéaires par rapport aux cristaux non linéaires conventionnels. Celles-ci incluent l'amélioration du champ électrique de la cavité, l'absence d'exigences d'accord de phase dues à la courte longueur des microcavités où le bon chevauchement des modes de polaritons devient bénéfique ainsi que l'accordabilité de l'angle.

En présence d'une non-linéarité de second ordre, nos calculs numériques montrent que les modes de polaritons peuvent être utilisés pour générer des rayonnements infrarouges et térahertz accordables. Ensuite, nous fabriquons des microcavités fonctionnant dans le régime de couplage lumière-matière ultra forte contenant un semiconducteur organique non linéaire possédant une grande non-linéarité de troisième ordre. Nous démontrons une génération de troisième harmonique accordable et efficace couvrant tout le spectre visible et nous montrons que la non-linéarité optique du matériau a été transmise aux polaritons à travers leur composante excitonique, constituant ainsi une nouvelle manière d'améliorer les interactions polariton-polariton.

Dans le contexte des fluides de polaritons, nous effectuons des simulations numériques d'une microcavité organique lorsque la densité des polaritons est supérieure à un seuil critique. Au-delà de ce seuil, la dispersion des polaritons par des défauts de l'échantillon est interdite et le liquide de polariton se comporte comme un superfluide. Nous avons réussi à reproduire les résultats expérimentaux de la superfluidité à température ambiante dans un condensat organique de polaritons obtenus par nos collaborateurs et nous avons clarifié la dynamique temporelle complexe du système. De tels systèmes peuvent permettre d'étudier les fluides quantiques à température ambiante et aux futurs appareils à polaritons de fonctionner dans un régime sans dissipation.

Nous concluons notre étude des non-linéarités des polaritons en étudiant une nouvelle classe de matériaux, celle des dichalcogénures de métaux de transition, dont on a prédit une forte non-linéarité excitonique. Nous couplons les excitons dans une monocouche de disulfure de tungstène à une onde de surface se propageant à faible perte et démontrons des polaritons à onde de surface de Bloch avec de grandes distances de propagation. Quand la densité de

polaritons est augmentée, nous observons pour la première fois dans ce matériel un décalage vers le bleu du mode de polariton inférieur, une démonstration claire des non-linéarités de polaritons.

Après avoir quantifié la force de la non-linéarité, nous implémentons une source de polariton non linéaire qui, en fonctionnement à deux pompes, est identique à un transistor à polariton. Nous soulignons que, bien que les besoins en énergie soient encore trop élevés pour des applications pratiques, notre système surpasse déjà les systèmes organiques à température ambiante en termes de stabilité et de distances de propagation. La structure est de fabrication simple et peut être adaptée à d'autres matériaux et même à des hétérostructures multicouches, permettant d'étudier les fluides polaritoniques dans divers systèmes excitoniques.

ABSTRACT

In the linear regime, two light beams will go through one another unperturbed. However, in the presence of optical nonlinearities, many technologically interesting effects can be observed, such as the generation of new optical frequencies and the control of one beam by another.

Due to the small nonlinearities found in optical crystals, high optical powers are typically required to observe such nonlinear effects. In some applications, such as in coherent light generation, high power operation is not problematic. In fact, frequency mixing and harmonic generation techniques are extensively used in commercial light sources with emission wavelengths ranging from the deep ultraviolet to the far infrared regions of the spectrum.

There are, however, many developing applications in which low power operation is critical. In the field of optical computation, for instance, optical transistors operating with only hundreds of photons are required to enable the fabrication of optical processors that are faster and more efficient than electronic ones. Such systems would also benefit from low power frequency conversion in order to interface optical signals of different frequencies to the same photonic circuit.

For low power operation to become feasible, very large optical nonlinearities are required. One system in which optical nonlinearities are so strong that the arrival of a single photon can block the transmission of another is that of a single quantum emitter placed inside a high quality optical cavity. The main drawbacks of such a system are their technological complexity, low scalability and operation at cryogenic temperatures.

In this thesis, we study an alternative approach to enhancing optical nonlinearities, in which a collection of emitters is made to interact strongly with light, creating mixed light-matter quasiparticles called exciton-polaritons. Compared to systems based on single emitters, our approach is of simpler implementation and is compatible with room-temperature operation.

Under resonant excitation, polaritons interact strongly through their excitonic component and have allowed for the demonstration of a number of nonlinear effects at room temperature. After reviewing the main properties of exciton polaritons, we investigate different ways in which polariton nonlinearities can be used for frequency mixing and harmonic generation, as well as for implementing novel nonlinear devices based on interacting polariton fluids.

In the first case, we consider systems in which the excitonic material embedded in a planar microcavity has a large second- or third-order optical nonlinearity. We show through numerical calculations and experiments that polaritonic modes have many advantages for

enhancing the efficiency of nonlinear processes when compared to conventional nonlinear crystals. These include the cavity electric-field enhancement, the absence of phase-matching requirements due to the short length of the microcavities, where the good overlap of polariton modes becomes beneficial, and angle tunability.

In the presence of a second-order nonlinearity, our numerical calculations show that polariton modes can be used for the generation of tunable infrared and terahertz radiation. Then, we fabricate microcavities operating in the ultrastrong light-matter coupling regime containing an organic nonlinear dye possessing a large third-order nonlinearity. We demonstrate efficient tunable third-harmonic generation spanning the entire visible spectrum and show that the optical nonlinearity of the dye was imparted onto polaritons via their excitonic component, thus constituting a new way of enhancing polariton-polariton interactions.

In the context of polariton fluids, we perform numerical simulations of an organic microcavity when the density of polaritons is increased above a critical threshold. Above this threshold, scattering of polaritons by defects in the sample becomes energetically forbidden and the polariton liquid behaves as a superfluid. We succeed in reproducing the experimental results of room-temperature superfluidity in an organic polariton condensate obtained by our collaborators and we shed light onto the complicated time dynamics of the system. Such systems can enable the study of quantum fluids at room-temperature and future polariton devices to operate in a regime without dissipation.

We conclude our study of polariton nonlinearities by investigating a new class of materials, that of atomically-thin transition metal dichalcogenides, which have been predicted to show strong excitonic nonlinearities. We couple the excitons in a monolayer of tungsten disulfide to a low-loss propagating surface wave and demonstrate Bloch surface wave polaritons with large propagation distances. As the density of polaritons is increased, we observe for the first time in this material set a blueshift of the lower polariton mode, a clear demonstration of polariton nonlinearities.

After quantifying the strength of the nonlinearity, we implement a nonlinear polariton source, which under two-pump operation is identical to a polariton transistor. We highlight that although the power requirements are still prohibitively high for practical applications, our system already outperforms organic ones at room temperature in terms of stability and propagation distances. The structure is of simple fabrication and can be tailored to other materials and even multilayer heterostructures, allowing the study of polariton fluids in a variety of excitonic systems.

TABLE OF CONTENTS

LIST OF TABLES

LIST OF FIGURES

LIST OF SYMBOLS AND ABBREVIATIONS

Abbreviations

CNR	Italian National Research Council (Consiglio Nazionale delle Ricerche)
TMM	Transfer Matrix Method
TM	Transverse Magnetic
TE	Transverse Electric
DBR	Distributed Bragg Reflector
BSW	Bloch Surface Wave
BSWP	Bloch Surface Wave Polaritons
NA	Numerical Aperture
CT	Charge Transfer
HOMO	Highest Occupied Molecular Orbital
LUMO	Lowest Unoccupied Molecular Orbital
2D	Two Dimensions
TMD	Transition Metal Dichalcogenide
NL	Nonlinear
DFG	Difference-Frequency Generation
SHG	Second-Harmonic Generation
THG	Third-Harmonic Generation
USC	Ultrastrong-Coupling Regime
PSF	Phase-Space Filling
GP	Gross-Pitaevskii
OPO	Optical Parametric Oscillator
BEC	Bose-Einstein Condensation
IR	Infrared
THz	Terahertz
NLO	Nonlinear Optical
BBO	β-Barium Borate
FWHM	Full-Width at Half-Maximum
PL	Photoluminescence
BK7	SCHOTT Borosilicate Crown Glass
CCD	Charge-Coupled Device
BFP	Back Focal Plane
CW	Continuous Wave

1L	Monolayer

Universal constants

$\hbar$	Reduced Planck constant
c	Speed of light in vacuum
ϵ_0	Vacuum permittivity
μ_0	Vacuum permeability
k_B	Boltzmann constant

Materials

Ag	Silver
AlAs	Aluminum arsenide
AlGaAs	Aluminum gallium arsenide
CdS	Cadmium sulfide
CdSe	Cadmium selenide
CdTe	Cadmium telluride
GaAs	Gallium arsenide
GaP	Gallium phosphide
InGaAs	Indium gallium arsenide
$LiNbO_3$	Lithium niobate
$MoSe_2$	Molybdenum diselenide
^{87}Ru	Rubidium
SiO_2	Silicon dioxide
Ta_2O_5	Tantalum pentoxide
ZnTe	Zinc telluride
WS_2	Tungsten disulfide
ZnO	Zinc oxide
GaN	Gallium nitride

Symbols common to all chapters

x, y, z	Cartesian coordinates
r	Polar coordinate
t	Time
L	Cavity thickness
ω	Angular frequency

T	Temperature
$k_\parallel$ or k	Parallel (in-plane) wavevector
E_C	Cavity dispersion
E_X	Exciton energy
E_B	Exciton binding energy
ϵ_r	Relative dielectric permittivity
ϵ	Dielectric permittivity
ϵ_b	Background dielectric permittivity
γ	Exciton absorption full-width at half-maximum
q	Cavity mode number
M_q	Q-th cavity mode
N	Number of excitons
V	Volume
e	Electron charge
f_i or f	Oscillator strength
m_e	Electron mass
Q	Quality factor
$\chi^{(2)}$ or $\chi^{(2)}_{ijk}$	Second-order nonlinear susceptibility
$\chi^{(3)}$ or $\chi^{(3)}_{ijkl}$	Third-order nonlinear susceptibility
Ω_R	Rabi frequency
$\hbar\Omega_R$	Rabi splitting
$\hat{a}_k$	Cavity photon annihilation operator
$\hat{a}_k^\dagger$	Cavity photon creation operator
$\hat{b}_k$	Exciton annihilation operator
$\hat{b}_k^\dagger$	Exciton creation operator
$\hat{p}_k$	Polariton annihilation operator
$\hat{p}_k^\dagger$	Polariton creation operator
X	Exciton Hopfield coefficient in the 2×2 Hamiltonian
C	Photon Hopfield coefficient in the 2×2 Hamiltonian
UP	Upper polariton
LP	Lower polariton
v_g	Group velocity
θ	Angle of incidence
m_{LP}	Lower polariton effective mass
γ_{LP}	Lower polariton decay rate
ω_0	Lower polariton angular frequency at normal incidence

g_{LP}	Lower polariton interaction constant in real space
k_x and k_y	In-plane wavevector components
$\Psi(r,t)$	Lower polariton wavefunction in real space
$P(r,t)$	Driving term in the Gross-Pitaevskii equation
k_p	Pump in-plane wavevector
ω_p	Pump angular frequency
k_0	Wavevector in vacuum
$\Delta E_{LP}(k)$	Lower polariton blueshift in momentum space
$\Delta E_{LP}(r)$	Lower polariton blueshift in real space
$V^{PP}_{k,k',q}$	Effective Coulomb interaction potential in momentum space
V_{XX}	Exciton-exciton interaction energy in momentum space
V_{SAT}	Saturation interaction energy in momentum space
Ψ_k	Lower polariton wavefunction in momentum space
g_{XX}	Exciton-exciton interaction constant in real space
g_{SAT}	Saturation interaction constant in momentum space
k^{NL}	Perpendicular nonlinear wavevector
E	Electric field amplitude
d	Total thickness of optical elements
GVD	Group-velocity dispersion
σ_t	Intensity full-width at half-maximum
t_0	Pump arrival time

Symbols related to planar optical microcavities

n	Real part of the refractive index
κ	Imaginary part of the refractive index
$\tilde{n}$	Complex refractive index
r_M	Mirror reflection coefficient
$r_M(0)$	Mirror reflection coefficient at normal incidence
$\vec{k}$ or $\mathbf{k}$	Wavevector
$k_\perp$	Perpendicular wavevector
$\mathbf{k_c}$	Cavity wavevector
$k_{c\parallel}$	Cavity in-plane wavevector
$k_{c\perp}$	Cavity perpendicular wavevector
$E_C(0)$	Cavity energy at normal incidence
ω_0	Cavity mode angular frequency
$\Delta\omega$	Cavity mode angular frequency full-width at half-maximum

$m_{\parallel}$	Photon effective mass
$\tilde{c}$	Speed of light in a dielectric
τ_c	Cavity photon lifetime
E_0	Incident electric field amplitude
E_S	Surface electric field amplitude
λ	Wavelength of light
$n_{eff,TE}$	Effective TE refractive index
$n_{eff,TM}$	Effective TM refractive index
d_p	Plasmonic penetration depth
ω_p	Plasma frequency
n_H	High refractive index in a DBR
n_L	Low refractive index in a DBR
r_{DBR}	DBR reflection coefficient
N	Number of periods in a DBR
ω_s	Stop band center angular frequency
$\Delta\omega_s$	Stop band angular frequency full-width at half-maximum
L_{DBR}	DBR penetration depth
θ_H	Angle of incidence inside a high-index layer in a DBR
θ_L	Angle of incidence inside a low-index layer in a DBR
ω_q	DBR cavity mode angular frequency
$\|R\|^2$	Reflectance or reflectivity
L_D	Cavity thickness with metallic mirrors
L_D	Cavity thickness with dielectric mirrors
n_{glass}	Refractive index of a glass substrate
β	Electric field decay constant
n_{eff}	Effective refractive index
E_{BSW}	Bloch surface wave dispersion

Symbols related to semiconductors and excitons

Ψ_{1s}	1s exciton wavefunction
a_B	Exciton Bohr radius
a_B^{2D}	Two-dimensional exciton Bohr radius
m^*	Reduced exciton mass
m_h	Hole mass
E_B^{2D}	Two-dimensional exciton binding energy
S_0	Singlet ground state

S_1	First excited singlet state
ω_0	Natural angular frequency
$\tilde{x}$	Electron position
x	Electron position amplitude
$\tilde{E}$	Electric field strength
D	Complex denominator function
$\chi^{(1)}$ or $\chi^{(1)}_{ij}$	Linear susceptibility
U	Potential energy
a	Anharmonic correction to a parabolic potential well
b	First order correction to a parabolic potential well
$P^{(1)}$	Linear polarization
$P^{(2)}$	Second-order polarization
$P^{(3)}$	Third-order polarization

Symbols related to cavity exciton-polaritons

$\hat{H}$	Light-matter Hamiltonian
$\hat{H}_{res}$	Resonant light-matter Hamiltonian
$\hat{H}_{antires}$	Anti-resonant light-matter Hamiltonian
$\hat{H}_{A^2}$	Squared vector potential Hamiltonian
$\hat{H}_{Pres}$	Resonant light-matter Hamiltonian in the polariton basis
E_P	Polariton dispersion
$E_{P\pm}$	Positive and negative polariton dispersions
k_{res}	Wavevector where cavity and exciton energies are resonant
D	Light-matter coupling constant
ω_X	Exciton angular frequency
y and z	Anomalous Hopfield coefficients
w	Photon Hopfield coefficient in the 4×4 Hamiltonian
x	Exciton Hopfield coefficient in the 4×4 Hamiltonian
$\|G\rangle$	Polariton ground state
A	Amplitude of the relative dielectric permittivity
ω_C	Cavity angular frequency

Symbols related to polariton interactions

$\hat{H}_{XX}$	Exciton-exciton interaction Hamiltonian
V_q^{XX}	Effective Coulomb interaction potential

k' and q	Two-dimensional in-plane wavevectors
$\hat{H}_{XC}^{sat}$	Saturation interaction Hamiltonian
$\hat{H}_{PP}$	Polariton-polariton interaction Hamiltonian
n_{sat}	Exciton saturation density
E	Energy
ω_{LP}	Lower polariton angular frequency
$\omega_{LP}(0)$	Lower polariton angular frequency at normal incidence
c_s	Speed of sound in the condensate
v_p	Flow velocity in the condensate

Symbols related to difference-frequency generation

$\vec{E}_{1,2}$	Incident pump electric fields
$\omega_{1,2}$	Incident pump angular frequencies
ω_3	Difference-frequency angular frequency
$\hbar\omega_{1,2}$	Incident pump energies
θ_i	Pump angle of incidence
θ_3	Difference-frequency angle of reflectance
N	Number of layers
$\mathcal{E}_i$	Real electric field strength
E_i^+	Complex forward electric field amplitude in layer i or in the nonlinear layer for pump $i = 1, 2$
E_i^-	Complex backward electric field amplitude in layer i or in the nonlinear layer for pump $i = 1, 2$
$\mathbf{E}_i$	Complex field amplitude vector in layer i
$\vec{k}_i$	Wavevector in layer i
k_{iz}	Perpendicular wavevector component in layer i
k_x	In-plane wavevector component
k_{iz}^q	Perpendicular wavevector component in layer i at frequency q
k_x^q	In-plane wavevector component at frequency q
n_i	Complex refractive index in layer i
T_i	Partial transfer matrix across layer i
M_{ij}	Interface transfer matrix between layers i and j
ϕ_i	Propagation transfer matrix inside layer i
T_N	Total transfer matrix
d_i	Thickness of layer i
μ	Magnetic permeability

$\mathcal{P}^{NL}$	Nonlinear polarization source term
$\mathcal{P}^{3}$	Difference-frequency polarization source term
$\mathbf{P}^{NL}$	Nonlinear polarization vector
ω_{NL}	Nonlinear angular frequency
$\mathbf{E}_{1,2}$	Pump field vectors
k_z^{3-}	Perpendicular difference-frequency wavevector for counter-propagating pumps
k_z^{3+}	Perpendicular difference-frequency wavevector for co-propagating pumps
$\mathbf{P}^{3-}$	Difference-frequency polarization vector for counter-propagating pumps
$\mathbf{P}^{3+}$	Difference-frequency polarization vector for co-propagating pumps
$\mathbf{E}_{js}$	Bound field vector in layer j
$\mathbf{S}_j$	Source vector in layer j
M_{js}	Source transfer matrix for layer j
ϕ_{js}	Source propagation matrix for layer j
E_{3T}	Transmitted difference-frequency field
E_{3R}	Reflected difference-frequency field
$R_j^{\pm}$	Auxiliary source vector components in layer j
$\mathbf{R}_j$	Auxiliary source vector in layer j
T_{12} and T_{22}	Components of the total transfer matrix
ω_0	Exciton angular frequency
E_{UP}	Upper-polariton energy
E_{LP}	Lower-polariton energy
E_{Mq}	Energy of the q-th mode
λ_3	Difference-frequency or Rabi wavelength
λ_{LP}	Lower-polariton wavelength
λ_{NL}	Nonlinear wavelength
ν_3	Nonlinear frequency
$\mathbf{k}_p$	Pump in-plane wavevector
$\mathbf{k}_s$	Signal in-plane wavevector
$\mathbf{k}_i$	Idler in-plane wavevector
CE	Conversion efficiency
$I_{1,2}$	Pump irradiances
I_3 or I_{DFG}	Difference-frequency irradiance
L	Crystal length

Symbols related to third-harmonic generation

Δ	Cavity detuning
Q_{LP}	Lower-polariton quality factor
N	Number density of molecules
LPN	N-th lower polariton mode
UPN	N-th upper polariton mode
$P_{3\omega}$	Third-harmonic peak power
P_{ω}	Fundamental peak power
C	Cubic fit coefficient
ω_1	Incident pump angular frequency
ω_4	Third-harmonic angular frequency
$\mathbf{P}^{4-}$	Third-harmonic polarization vector for counter-propagating pumps
$\mathbf{P}^{4+}$	Third-harmonic polarization vector for co-propagating pumps
E_1^+	Pump forward electric field in the nonlinear layer
E_-^+	Pump backward electric field in the nonlinear layer
k_z^1	Pump perpendicular wavevector component
k_z^{4-}	Perpendicular third-harmonic wavevector for counter-propagating pumps
k_z^{4+}	Perpendicular third-harmonic wavevector for co-propagating pumps
P_{4R}	Average third-harmonic power emitted toward the excitation side
E_{R4}	Electric field of the third-harmonic signal emitted toward the excitation side
f	Pump repetition rate
τ_t	Pump pulse duration
τ_r	Third-harmonic spot waist

Symbols related to polariton superfluidity

T_C	Critical temperature
λ_T	Thermal de Broglie wavelength
M	Particle mass
E_p	Pump energy
V	Potential barrier
F_p	Driving term amplitude
I_0	Pump irradiance
C_{k_p}	Lower polariton photon fraction at the pump in-plane wavevector

E_{in}	Incident pump fluence
$FWHM$	Intensity full-width at half maximum
Ψ_{SS}	Steady-state polariton wavefunction
$\mathcal{L}_k$	Linear operator
$\delta\Psi$	Small fluctuation
$\mathcal{U}_k$	Small-fluctuations vector
n_p	Polariton density in real space
$\omega_{LP}^{\pm}$	Positive and negative lower polariton Bogoliubov dispersions

Symbols related to Bloch surface wave polaritons

$\vec{k}_{BSW}$	Bloch surface wave wavevector
E_0	Dispersion fitting parameter
C_k	Lower polariton photon fraction
L_x and L_y	Monolayer dimensions
A	Quantization area
d_{kx} and d_{ky}	Momenta intervals
σ_k	Pump full-width at half-maximum in momentum space
k_{y0}	Pump center wavevector
G	Gaussian distribution in momentum space
E_{in}	Incident energy
f	Pump repetition rate
P_{in}	Average pump power
I_0	Peak incident power
t_{max}	Instant of maximum weighed polariton density
E_{1s}	1s exciton binding energy
λ_X	1s exciton radius
P	Pump fluence

LIST OF APPENDICES

CHAPTER 1 INTRODUCTION

Modern communication networks use optical signals to transmit information because light can propagate unperturbed over large distances and at a very high speed. Such success has motivated the use of optical interconnects also inside integrated circuits, where increasing the operating speed and lowering the heat dissipation are critical. However, the routing and modulation of optical signals at increasingly high speeds poses a technical challenge.

Materials possessing strong optical nonlinearities can enable one light beam to manipulate another almost instantaneously. However, even the best nonlinear optical crystals still require strong optical excitation to produce significant nonlinear effects. Thus, significant attention has been devoted to developing new materials with stronger nonlinearities and to finding new physical systems displaying nonlinear optical behaviour.

One such system consists of a single quantum emitter, such as a quantum dot or a molecule, placed inside a high quality optical resonator [1, 2]. When the cavity mode is resonant with an excitonic transition of the emitter, a photon inside the cavity can be absorbed and re-emitted multiple times before escaping the cavity. This coherent energy exchange is better described not in terms of photons and excitons, but in terms of new half-light, half-matter quasiparticles called exciton-polaritons [3–5]. In the particular case of a single emitter, the effective optical nonlinearity is so large that the presence of a single photon can modify the response of the system.

Because cavity polaritons essentially behave as strongly interacting photons, even for multiple emitters and in the high-excitation regime, they have attracted significant interest both for fundamental studies and for technological applications [6, 7]. These include the study of quantum fluids in room-temperature polariton Bose-Einstein condensates, nonlinear optics by enabling ultra-efficient parametric scattering, amplification [8–10] and bistability [11], solid-state lighting and sensing through low threshold inversionless lasers [12–14] and all-optical polaritonic circuits [15–18].

This thesis was motivated by the unique properties of cavity exciton-polaritons and by their great technological potential. We begin by exploring the use of nonlinear materials to enhance resonant polariton nonlinearities in the context of frequency mixing and harmonic generation. Then, we study two systems in which polaritons propagate in a fluid-like fashion. In the first one, an organic microcavity, we investigate the regime of polariton superfluidity. In the second, we use surface waves to observe polariton nonlinearities in an atomically-thin semiconductor monolayer.

1.1 Outline

We begin our study in Chapter 2 with a review of the fundamental concepts of exciton-polaritons. First, we study the energy dispersion and the main figures of merit of planar microcavities. Then, we introduce the concept of excitons and use it to describe the dielectric response of semiconductors. That allows us to consider the case of a cavity filled with an excitonic material and to treat the coupling of light and matter explicitly. Finally, we discuss the origin of polariton-polariton and polariton-exciton interactions and present a short literature review of the main nonlinear effects observed in polaritonic systems.

In Chapter 3 we consider the case when the semiconductor layer inside the cavity is non-centrosymmetric and possesses an intrinsic second-order susceptibility. We numerically investigate the use of polaritonic modes to allow for the generation of tunable infrared and terahertz radiation. We show that the generation of Rabi-frequency radiation, a process which is analogous to classical difference-frequency generation (DFG), can have efficiency enhancement factors of up to three orders of magnitude in the polaritonic case compared to bare films. This is shown to be not only due to the enhancement of the electric fields, but also due to the increased modal overlap of polaritonic modes. The discussion presented in this chapter was adapted from the publication [19]

> F. Barachati, S. De Liberato, and S. Kéna-Cohen, "Generation of rabi-frequency radiation using exciton-polaritons", Phys. Rev. A, vol. 92, p. 033828, Sep 2015. Copyright © 2015 by the American Physical Society. DOI: 10.1103/PhysRevA.92.033828.

The three following chapters discuss the effects of third-order nonlinearities. In Chapter 4, we fabricate organic microcavities embedding a nonlinear dye possessing a large optical third-order susceptibility, which leads to enhanced polariton-polariton interactions via their photonic component. The increased nonlinearity is used to demonstrate tunable third-harmonic generation (THG) from polaritons spanning the entire visible spectrum. We also address the peculiarities of the ultrastrong light-matter coupling regime. This chapter was adapted from the publication [20]

> F. Barachati, J. Simon, Y. A. Getmanenko, S. Barlow, S. R. Marder, and S. Kéna-Cohen, "Tunable third-harmonic generation from polaritons in the ultrastrong coupling regime", ACS Photonics, vol. 5, no. 1, pp. 119–125, 2018. Copyright © 2018 by the American Chemical Society. DOI: 10.1021/acsphotonics.7b00305.

Contrary to Chapter 4, most materials have a very low third-order susceptibility. Nonetheless, third-order nonlinear effects are still observed in organic polaritonic systems. To compensate for weak nonlinearities, the density of polaritons must be increased substantially. In Chapter 5, we present the main experimental results obtained by our collaborators in the group of Dr. Daniele Sanvitto (CNR Nanotec institute), which show the first evidence of room-temperature superfluid behavior in an organic polariton condensate. They observed that at sufficiently high densities and for a certain range of group velocities, the polariton flow transitioned from dissipative to scattering-free.

Using their experimental parameters, we perform time-dependent simulations of the polariton fluid, modeled by a mean-field dissipative Gross-Pitaevskii equation. We reproduce the superfluid behaviour and shed light on the complicated temporal dynamics of the system. This chapter focuses on the numerical simulations performed in our group and the results presented here were adapted from the publication [21]

> G. Lerario, A. Fieramosca, F. Barachati, D. Ballarini, K. S. Daskalakis, L. Dominici, M. De Giorgi, S. A. Maier, G. Gigli, S. Kéna-Cohen, and D. Sanvitto, "Room-temperature superfluidity in a polariton condensate", Nature Physics, vol. 13, no. 9, p. 837, 2017. Copyright © 2017 by Springer Nature: Nature Physics. DOI: 10.1038/nphys4147.

Finally, in Chapter 6, we demonstrate strong light-matter coupling between excitons in a monolayer transition metal dichalcogenide and a propagating Bloch surface wave. As a result of the low losses in both the dielectric mirror and the monolayer, the polariton fluid is capable of propagating over macroscopic distances. The increased polariton lifetime due to the low losses and the large electric field enhancement allowed us to perform the first demonstration of polariton nonlinearities in this class of materials. We quantify the nonlinearity and demonstrate a nonlinear polariton source. The discussion presented in this chapter was adapted from the publication [22]

> F. Barachati, A. Fieramosca, S. Hafezian, J. Gu, B. Chakraborty, D. Ballarini, L. Martinu, V. Menon, D. Sanvitto, and S. Kéna-Cohen, "Interacting polariton fluids in a monolayer of tungsten disulfide", Nature Nanotechnology, 2018. Copyright © 2017 by Springer Nature: Nature Nanotechnology. DOI: 10.1038/s41565-018-0219-7.

CHAPTER 2 CAVITY EXCITON-POLARITONS

2.1 Planar optical microcavities

One of the main advantages of confining light within optical resonators is the possibility to enhance the intra-cavity electric field. The field enhancement and spatial confinement lead to stronger light-matter interactions and reduced power and phase-matching constraints for the observation of nonlinear effects. In this section we will focus on planar optical microcavities, typically referred to as Fabry-Perot resonators, and review their main properties.

Consider the simple case of a symmetric microcavity composed of a lossless central layer of thickness L and refractive index n, sandwiched between two identical mirrors with reflection coefficient r_M and surrounded by air. A schematic of this system is shown in Fig. 2.1a.

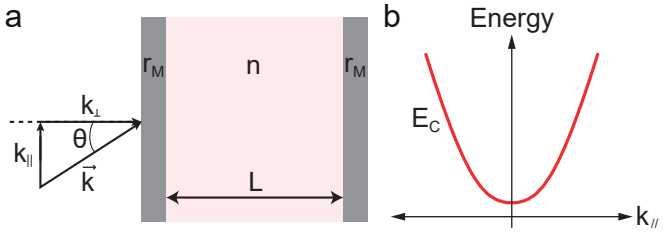

Figure 2.1 (a) Planar microcavity consisting of two flat mirrors and a uniform semiconductor layer. (b) Cavity dispersion as a function of the in-plane wavevector $k_{\|}$, which is related to the angle of incidence θ by $k_{\|} = (\omega/c)\sin\theta$.

It can be shown by the transfer matrix method (TMM), which will be described in detail in Chapter 3, that the optical frequencies supported by this simple resonator are given by [23]

$$r_M^2 e^{2ik_{c\perp}L} = 1. \tag{2.1}$$

We will begin our analysis by considering that the cavity is composed of ideal mirrors, where light is completely reflected at the surface without suffering losses. Then, we will consider the particularities of metallic and dielectric mirrors in terms of losses and field penetration.

2.1.1 Ideal mirrors

For the case of ideal mirrors with $r_M = e^{-i\pi}$, the eigenfrequencies of the $q \geq 1$ supported modes are given by

$$k_{c\perp} L = q\pi. \tag{2.2}$$

From the boundary conditions at the air/mirror and mirror/cavity interfaces, the wavevector components inside the cavity (with superscript c) can be related to those in air by

$$|\mathbf{k_c}|^2 = n^2 |\mathbf{k}|^2 = n^2 (\omega/c)^2, \tag{2.3}$$

$$k_{c\parallel} = k_{\parallel} = (\omega/c)\sin\theta, \tag{2.4}$$

and

$$k_{c\perp} = \sqrt{|\mathbf{k_c}|^2 - k_{c\parallel}^2} = \sqrt{n^2(\omega/c)^2 - (\omega/c)^2 \sin^2\theta} = (\omega/c)\sqrt{n^2 - \sin^2\theta}. \tag{2.5}$$

For simplicity, whenever possible we will represent vector quantities in regular text (e.g. $\mathbf{k} \equiv k$,$\mathbf{r} \equiv r$) throughout this manuscript. Combining Eqs. (2.2) and (2.5), we obtain the following relationship

$$\frac{\omega}{c}\sqrt{n^2 - \sin^2\theta} = \frac{q\pi}{L}, \tag{2.6}$$

which can be rewritten as

$$\omega(k_{\parallel}) = \sqrt{\left(\frac{q\pi c}{nL}\right)^2 + \left(\frac{ck_{\parallel}}{n}\right)^2}. \tag{2.7}$$

If we define $E_C(0) = \frac{\hbar q\pi c}{nL}$ as the cavity energy at normal incidence, the cavity dispersion relation can be written as

$$E_C(k_{\parallel}) = \sqrt{E_C^2(0) + \left(\frac{\hbar c k_{\parallel}}{n}\right)^2}. \tag{2.8}$$

The dispersion given by Eq. (2.8) has a parabolic shape as a function of $k_{\parallel}$ and is illustrated in Fig. 2.1b. By performing a Taylor expansion on Eq. (2.8) we obtain

$$E_C(k_{\parallel}) = E_C(0) + \frac{\hbar^2 c^2 k_{\parallel}^2}{2n^2 E_C(0)} = E_C(0) + \frac{\hbar^2 k_{\parallel}^2}{2m_{\parallel}}, \tag{2.9}$$

where $m_{\parallel} = \frac{n^2 E_C(0)}{c^2} = \frac{\hbar q\pi n}{cL}$ is defined as the photon effective mass. Therefore, the dispersion of a cavity photon in an ideal planar microcavity resembles that of a free particle with mass $m_{\parallel}$ in the region $\hbar(c/n)k_{\parallel} \ll E_C(0)$, what is commonly referred to as the effective

mass approximation. The extremely low effective mass of cavity photons, of the order of $10^{-10} \sim 10^{-7}$ times the electron mass, will play an important role in the nonlinear properties of cavity exciton-polaritons in the context of Bose-Einstein condensation.

Finally, it is interesting to rewrite the dispersion shown in Eq. (2.7) also including the effective mass

$$[\hbar\omega]^2 = \left[m_{\parallel}\tilde{c}^2\right]^2 + \left[\hbar\tilde{c}k_{\parallel}\right]^2. \tag{2.10}$$

According to special relativity, this is exactly the dispersion of a relativistic particle of mass $m_{\parallel}$ moving at a speed $\tilde{c} = c/n$ [24].

2.1.2 Metallic mirrors

In the previous section we considered ideal mirrors with reflection coefficient $r_M = e^{-i\pi}$. The π phase change is responsible for the vanishing of the cavity electric field at the surface of the mirrors while $|r_M|^2 = 1$ indicates the absence of losses. In practice though, both the losses and the finite penetration of the electric field in the mirror must be taken into account.

To include material losses we introduce an imaginary contribution to the now complex refractive index

$$n = \tilde{n} + i\kappa. \tag{2.11}$$

At normal incidence, the Fresnel reflection coefficient at the air interface of a material with index n is given by [25]

$$r_M(0) = \frac{1 - \tilde{n} - i\kappa}{1 + \tilde{n} + i\kappa}. \tag{2.12}$$

The refractive index of metals is characterized by a large imaginary part and a small real part. For example, the refractive index of thermally-evaporated silver at a wavelength of 1 μm is $n = 0.12 + 7.15i$ and the corresponding reflection coefficient is $r_M(0) = -0.96 - 0.27i = 0.995e^{-i0.9\pi}$. In the limit $\tilde{n} \to 0$ and $\kappa \to \infty$ we recover the behavior of an ideal mirror.

Aside from limiting the electric field enhancement, metal losses lead to a broadening of the mode linewidth. This has a direct impact on the quality factor Q, one of the main figures of merit for optical microcavities in the presence of losses. It quantifies the amount of energy stored inside the resonator compared to that lost in each round-trip and is defined as

$$Q = \frac{\omega_0}{\Delta\omega}, \tag{2.13}$$

where ω_0 and $\Delta\omega$ are the cavity mode frequency and full-width at half-maximum (FWHM),

respectively. The high losses stemming from metallic mirrors typically limit the quality factors of single-mode planar microcavities to $Q < 200$. The quality factor is also connected to the cavity photon lifetime

$$\tau_c = \frac{Q}{\omega_0}, \tag{2.14}$$

with typical values of the order of $\tau_c \sim 100$ fs. Such short lifetimes typically make the observation of nonlinear polariton effects in metallic cavities challenging due to the difficulty in achieving high polariton densities. In contrast, much longer lifetimes (> 100 ps) can be attained through the use of low loss dielectric mirrors [26].

The penetration of the electric field into metallic mirrors is limited by an exponential decay of the form

$$E(x) = E_0 e^{2\pi\kappa x/\lambda}, \tag{2.15}$$

where E_0 is the incident field, λ the wavelength of light and x the propagation distance from the surface of the mirror. For a thermally-evaporated silver mirror, the field falls to $E_0/2$ in ~ 15 nm, a distance much smaller than the wavelength. Therefore, for metallic microcavities, the resonance frequency is dictated by the cavity length, which for a single-mode cavity is given by $L = \lambda/(2n)$.

At high angles of incidence, the longer field penetration for the transverse magnetic (TM) component compared to the transverse electric (TE) one leads to a TE-TM mode splitting. Still, Eq. (2.8) can be used to accurately describe the dispersion in metallic microcavities as long as the refractive index n is replaced by the polarization-dependent effective index [27]

$$n_{eff,TE} = n \tag{2.16}$$

$$n_{eff,TM} = \frac{n(2d_p + L)}{\sqrt{L^2 - (2d_p)^2}}, \tag{2.17}$$

where $d_p = c/\omega_p$ is an effective plasmonic penetration depth (~ 20 nm for silver) and ω_p is the plasma frequency. The effective index for TM polarization can be much larger than that of the cavity material and leads to a flatter dispersion.

2.1.3 Dielectric mirrors

Although metallic mirrors are extremely simple to fabricate, metal losses impose important limitations on the cavity electric field enhancement and quality factor. An attractive alternative of more complex fabrication is found in distributed Bragg reflectors (DBRs), which are

mirrors composed of alternating dielectric layers of high (n_H) and low (n_L) refractive index. When operated in the transparency region of the dielectrics, the mirror losses are extremely low and stem mainly from scattering due to layer roughness and growth imperfections.

Each layer of the periodic stack has a thickness of $\lambda/(4n_{H,L})$, where λ is the design wavelength, such that the constructive interference of successive reflections for waves with wavelength in the vicinity of λ will lead to a high reflectivity. At this wavelength, the reflection coefficient for a DBR surrounded by air and a cavity material of index n at normal incidence is approximately given by [23]

$$r_{DBR} = -\sqrt{1 - 4n\left(\frac{n_L}{n_H}\right)^{2N}}, \tag{2.18}$$

where N is the number of periods. The reflectivity rapidly approaches unity for N large and for dielectric materials with large refractive index contrast. For instance, at a wavelength of $\lambda = 1$ μm, a DBR with 20 pairs of amorphous silicon ($n_H = 3.46$) and silicon dioxide ($n_L = n = 1.50$) has a reflection coefficient of $r_{DBR} = -0.9999998$. Consequently, DBR microcavities enable quality factors and electric field enhancements several orders of magnitude larger than those possible with metallic mirrors.

The range of wavelengths where the mirror reflectivity remains high is known as the stop band. At normal incidence, the center of the stop band is related to the design wavelength by [23]

$$\omega_s = \frac{2\pi c}{\lambda} \tag{2.19}$$

and the width is given by [23]

$$\Delta\omega_s = \omega_s \frac{4}{\pi} \sin^{-1}\left(\frac{n_H - n_L}{n_H + n_L}\right). \tag{2.20}$$

The stop band becomes wider for materials with a high refractive index contrast. This is particularly useful when the cavity or polariton modes of interest span a large energy interval.

Finally, the electric field penetration in the mirrors is characterized by [23]

$$L_{DBR}(\theta) = \frac{\lambda}{2(n_H^2 - n_L^2)}\left(n_H \cos^2\theta_H + n_L \cos^2\theta_L\right), \tag{2.21}$$

where $\theta_{H,L}$ are the angles inside the dielectric layers

$$\theta_{H,L} = \sin^{-1}\left(\frac{\sin\theta}{n_{H,L}}\right). \tag{2.22}$$

For conventional materials with a refractive index contrast of $n_H - n_L = 0.5$, $L_{DBR} \sim \lambda$ and the cavity resonance will not be dictated only by the cavity length L, as in the case for metallic mirrors. Instead, the cavity mode frequencies are given by [23]

$$\omega_q(\theta) = \frac{L\omega(\theta) + L_{DBR}\omega_s(\theta)}{L + L_{DBR}(\theta)}, \tag{2.23}$$

where the full polarization and angle dependence of each term must be taken into account. Since in practice L_{DBR} is typically larger than L, the cavity resonance frequency is more strongly determined by the center of the stop band.

Comparison

To illustrate the concepts described in Sections 2.1.2 and 2.1.3, we show in Fig. 2.2a,b the reflectivity spectra for planar microcavities with dielectric (a) and metallic (b) mirrors. The corresponding quality factors are indicated for the first cavity mode, as well as the position of the stop band in the dielectric case. Figure 2.2c,d shows the corresponding electric field enhancements, where the vertical lines indicate the interfaces of the mirror elements. Note the larger spatial extent and enhancement of the electric field in the dielectric case.

Surface modes

Planar microcavities are by no means the only optical resonator architecture used in the study of strong light-matter coupling. Here we highlight that the dielectric mirrors themselves support confined optical modes, known as Bloch surface waves (BSWs). Dielectric mirrors are typically grown by various techniques on transparent glass substrates. When the angle of incidence of light inside this substrate is higher than $\sin^{-1}(1/n_{glass})$, light will suffer total internal reflection at the top mirror/air surface. The set of angles of incidence and wavelengths where the mode wavevector is larger than the one in air ($k_0 = \omega/c$) constitutes the so-called light line.

It can be shown that the solution of the wave equation for a periodic dielectric structure in contact with a homogeneous medium, such as for a DBR interfaced with air, leads to a set of allowed propagation constants that fall beyond the light line and within the stop band of the

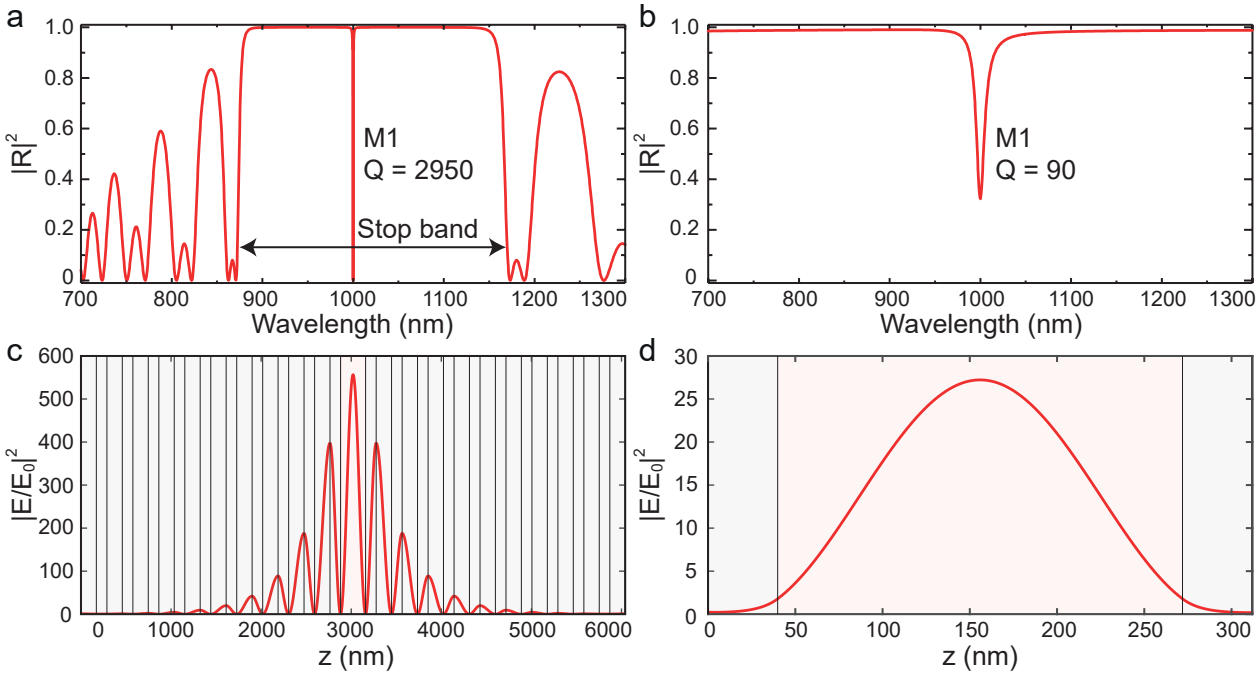

Figure 2.2 Reflectivity spectra for a planar microcavity with (a) dielectric and (b) metallic mirrors. The first cavity mode $M1$ is indicated, as well as the position of the stop band in the DBR case. The DBR consisted of 10 pairs of SiO_2/Ta_2O_5 with thicknesses of 171 nm and 117 nm, respectively, while the silver mirrors were 40 nm thick. The cavity thicknesses were $L_D = 278$ nm and $L_M = 232$ nm for the same background index of $n = 1.8$. Electric field enhancement for the first cavity mode for the (c) dielectric and (d) metallic cases. The vertical lines indicate the interfaces of the mirror elements.

DBR. For these waves, as shown in Fig. 2.3b, the electric field is confined near the surface of the mirror and has an exponential decay in air of the form (for TE polarization) [28]

$$E_y(x, z, t) = E_S e^{-\beta x} e^{i(\omega t - k_{c\|} z)}, \tag{2.24}$$

where E_S is the field amplitude at the surface, β is the field decay constant (perpendicular to the surface) and $k_{c\|}$ is the propagation constant (parallel to the surface). The field decay constant is given by [28]

$$\beta = \sqrt{k_{c\|}^2 - \left(\frac{\omega}{c}\right)^2}. \tag{2.25}$$

An effective refractive index can be associated to the BSW mode from the normalized propagation constant [28]

$$\frac{k_{c\|}}{k_0} = \frac{k_{c\|}}{\omega/c} = n \sin(\theta) = n_{eff}. \tag{2.26}$$

Since $n_{eff} > 1$, BSW modes must be excited through a prism, what is known as the Kretschmann configuration, or through an immersion microscope objective with numerical aperture (NA) larger than n_{eff}.

Figure 2.3a shows the reflectivity of a DBR mirror at increasing normalized momenta. As the angle of incidence θ increases, the stop band of the mirror moves to shorter wavelengths (higher energies). Inside the stop band and above the light line, a very narrow BSW mode can be seen. Figure 2.3b shows the electric field profile and enhancement for the BSW mode at a wavelength of $\lambda = 700$ nm and corresponding angle of incidence of $\theta = 51.27^o$. The field decays to $E_S/2$ in a distance of 36 nm and this is inversely proportional to the magnitude of β. Such BSW modes will propagate on the surface of the sample with a group velocity given by $v_g = \frac{1}{\hbar}\frac{dE_{BSW}(k)}{dk}$ and will be revisited in Chapter 6.

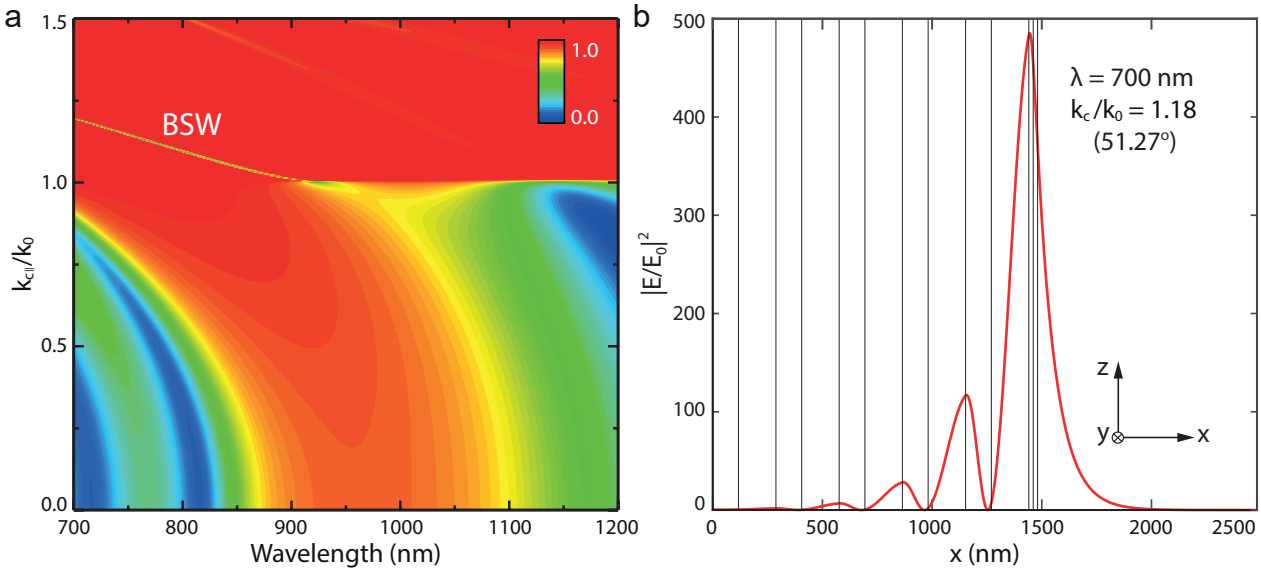

Figure 2.3 (a) Reflectivity of a DBR as a function of normalized in-plane momentum. A narrow Bloch surface wave mode can be seen inside the stop band and above the light line. (b) Irradiance enhancement showing that the field peaks close to the surface and decays exponentially in air. The structure consisted of five pairs of Ta_2O_5/SiO_2 (117 nm/171 nm) followed by a narrower pair (20 nm/20 nm).

2.2 Semiconductors

In this section we will review a few basic properties of semiconductor materials. We will review the main concepts of quasiparticles called excitons, which are bound electron-hole pairs created within these materials, and highlight the main differences in the response of

organic and inorganic semiconductors to light.

2.2.1 Excitons

Following the absorption of a photon in a semiconductor, an electron is promoted to a higher energy band and leaves behind a positively charged vacancy (a hole) in the previously filled lower energy band, as shown in Fig. 2.4. The resulting system is similar to a hydrogen atom, with the main differences being that the Coulomb attraction is now screened by the dielectric medium and that the masses of the proton and electron are replaced by effective hole and electron masses accounting for the specific band structure of the material. The wavefunction of the 1s exciton is given by [25]

$$\Psi(r)_{1s} = \frac{1}{\sqrt{\pi a_B^3}} e^{-r/a_B}, \tag{2.27}$$

where r is the distance between the electron and the hole. The Bohr radius a_B is defined as [25]

$$a_B = \frac{4\pi\epsilon_r\epsilon_0\hbar^2}{m^* e^2}, \tag{2.28}$$

where $m^* = m_e m_h/(m_e + m_h)$ is the reduced exciton mass, $-|e|$ is the electron charge and $\epsilon_r\epsilon_0 = \epsilon$ is the dielectric permittivity.

One of the most important quantities we will also consider is the exciton binding energy E_B, given by [25]

$$E_B = \frac{\hbar^2}{2m^* a_B^2}. \tag{2.29}$$

This is the energy required to ionize the exciton into a free electron and hole. Excitons will auto ionize at temperatures above $T > E_B/k_B$, where k_B is Boltzmann's constant, and this indicates the temperature regime where excitons are stable and can be observed.

These two properties can be used as a starting point to understand excitonic effects in different semiconductor materials. Organic semiconductors have dielectric constants of the order $\epsilon_r \sim 3$, much lower than in their inorganic counterparts where $\epsilon_r \sim 10$. As a consequence, excitons in these materials, called Frenkel excitons, are highly localized. Figure 2.4a shows a schematic of a crystalline organic semiconductor and two types of Frenkel excitons, the first localized on the same molecule and the second, known as a charge transfer (or CT) exciton, shared between two adjacent molecules. In the case of inorganics, shown in Fig. 2.4b, the large Bohr radii means the so-called Wannier-Mott excitons are delocalized over many lattice sites.

This will have important consequences on the exciton-exciton interaction strength in these materials.

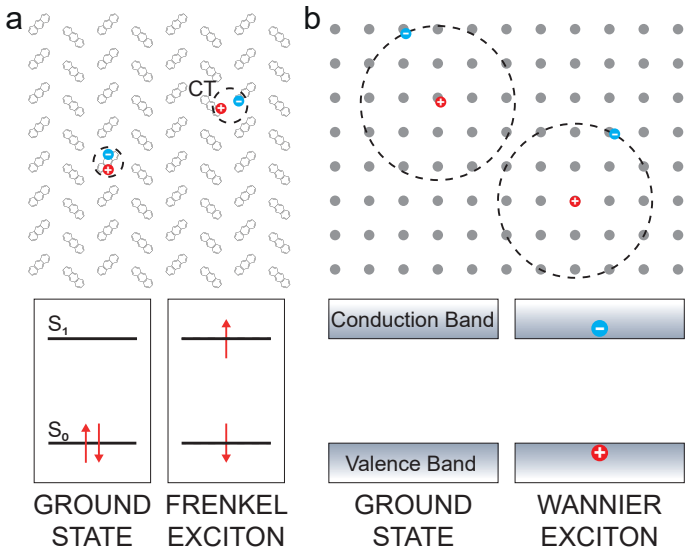

Figure 2.4 (a) Schematic of an organic crystal with low dielectric constant, illustrating Frenkel excitons localized in one molecule or in neighboring molecules (charge transfer or CT exciton). The ground state of a molecule (S_0) has singlet character due to pairing of electronic spins. Absorption of a photon leads the molecule to the first excited singlet state (S_1). Absorption of light occurs between the highest occupied molecular orbital (HOMO) and the lowest unoccupied molecular orbital (LUMO). (b) Schematic of an inorganic crystal with high dielectric constant, illustrating Wannier-Mott excitons delocalized over many lattice sites. Absorption of light promotes an electron from a filled valence band into an empty conduction band. This considers that the semiconductor is at a temperature of 0K.

The much lower dielectric constant in organic semiconductors also leads to an increase in the exciton binding energy to values much larger than $k_BT \sim 25$ meV, even exceeding 1 eV. As a result, the optical properties of organic semiconductors are dictated by Frenkel excitons even at room temperature. In sharp contrast, the binding energies of Wannier-Mott excitons are typically much lower than k_BT and they are only stable at cryogenic temperatures. Organic semiconductors are therefore very attractive for enabling practical excitonic devices operating at room temperature.

The large spatial extent of Wannier-Mott excitons makes them very sensitive to spatial confinement. A typical strategy to stabilize excitons in inorganic semiconductors is to confine them to two dimensions (2D) inside a quantum well, which is typically narrower than the exciton radius [25]. This leads to an enhancement of the binding energy of $E_B^{2D} = 4E_B$ and a reduction of the Bohr radius of $a_B^{2D} = a_B/2$. The limiting case is found in atomically

thin semiconductors, such as transition metal dichalcogenide (TMD) monolayers, for which Wannier-Mott excitons with $E_B > 10k_BT$ are common and therefore stable at room temperature. At the same time, the modified screening in these materials is expected to contribute to enhancing exciton-exciton interactions [29], potentially combining the best properties of organic and inorganic semiconductors for practical nonlinear devices.

2.2.2 Linear response

To describe the interaction of an exciton with light outside a microcavity, we will consider a classical model that, despite its simplicity, will enable us to introduce many important concepts of light-matter interaction. We consider the case of an electron bound to a hole under an applied electric field. The system behaves as a driven damped harmonic oscillator, where the natural frequency ω_0 is equal to the exciton transition frequency and the damping γ stems from interactions with the environment. The position $\tilde{x}$ of the electron is described by [30]

$$\ddot{\tilde{x}} + 2\gamma\dot{\tilde{x}} + \omega_0^2\tilde{x} = -|e|\tilde{E}(t)/m_e. \tag{2.30}$$

If the electric field has the form (we will omit the complex conjugates) [30]

$$\tilde{E}(t) = E(\omega)e^{-i\omega t}, \tag{2.31}$$

the solution to Eq. (2.30) is the so-called linear Lorentz model, which is given by [30]

$$\tilde{x}(t) = x(\omega)e^{-i\omega t}, \tag{2.32}$$

where

$$x(\omega) = -\frac{|e|}{m_e}\frac{E(\omega)}{D(\omega)} \tag{2.33}$$

and with the complex denominator function defined as

$$D(\omega) = \omega_0^2 - \omega^2 - 2i\omega\gamma. \tag{2.34}$$

The total contribution of a number density N/V of excitons to the linear polarization is [30]

$$P^{(1)}(\omega) = -\frac{N|e|}{V}x(\omega). \tag{2.35}$$

We can now introduce the linear susceptibility $\chi^{(1)}$ as [30]

$$P^{(1)}(\omega) = \epsilon_0 \chi^{(1)}(\omega) E(\omega), \tag{2.36}$$

which relates the applied electric field to the resulting polarization. Combining these two expressions we obtain

$$\chi^{(1)}(\omega) = \frac{Ne^2}{V\epsilon_0 m_e} \frac{1}{D(\omega)}. \tag{2.37}$$

The complex dielectric constant can be obtained from

$$\epsilon(\omega) = \epsilon_0(1 + \chi^{(1)}) = \epsilon_0 + \frac{Ne^2}{Vm_e} \frac{1}{D(\omega)}. \tag{2.38}$$

This model considers that all excitons contribute to the oscillator. We can generalize Eq. (2.38) by considering multiple oscillators at different frequencies ω_{0i} and that only a fraction f_i of the excitons contributes to each oscillator. Then,

$$\epsilon(\omega) = \epsilon_0 + \frac{Ne^2}{Vm_e} \sum_i \frac{f_i}{\omega_{0i}^2 - \omega^2 - 2i\omega\gamma_i.}. \tag{2.39}$$

The fraction f_i is called the oscillator strength and will play an important role in the discussion of strong light-matter coupling.

2.2.3 Nonlinear response

When considering Eq. (2.30), we implicitly imposed that the electron was trapped in a symmetric and infinite parabolic potential of the form [30]

$$U(\tilde{x}) = \frac{1}{2} m_e \omega_0^2 \tilde{x}^2. \tag{2.40}$$

A more realistic model would consider the parabolic potential to be a good approximation only for small displacements, while additional correction terms would be required under intense driving. We will now consider a new potential well described by

$$U(\tilde{x}) = \frac{1}{2} m_e \omega_0^2 \tilde{x}^2 + \frac{1}{3} m_e a \tilde{x}^3 - \frac{1}{4} m_e b \tilde{x}^4. \tag{2.41}$$

The second term with $a > 0$ describes an anharmonic correction which is only non-vanishing in non-centrosymmetric systems where $U(\tilde{x}) \neq U(-\tilde{x})$. The last term with $b > 0$ is the lowest

order correction to an ideal parabolic potential well. Since the first term was associated with a linear polarization $P^{(1)}(\omega)$ and susceptibility $\chi^{(1)}(\omega)$, the correction terms will give rise to second- and third-order polarization contributions [30], such as for example

$$P^{(2)}(2\omega) = \epsilon_0 \chi^{(2)}(2\omega;\omega,\omega)E^2(\omega) \tag{2.42}$$

$$P^{(3)}(3\omega) = \epsilon_0 \chi^{(3)}(3\omega;\omega,\omega,\omega)E^3(\omega) \tag{2.43}$$

and their corresponding susceptibilities [30]

$$\chi^{(2)}(2\omega;\omega,\omega) = \frac{N|e|^3 a}{\epsilon_0 V m_e^2} \frac{1}{D(2\omega)D^2(\omega)} \tag{2.44}$$

$$\chi^{(3)}(3\omega;\omega,\omega,\omega) = \frac{N|e|^4 b}{\epsilon_0 V m_e^3} \frac{1}{D(3\omega)D^3(\omega)}. \tag{2.45}$$

When the incident electric field only contains a single frequency $\omega = \omega_1$, the above nonlinear susceptibilities are responsible for the generation of new frequency components with two and three times the fundamental frequency, which is referred to as second- and third-harmonic generation. When more frequency components are present (e.g. ω_2 and ω_3), several additional nonlinear mixing processes can take place, such as sum- (e.g. $\omega_1+\omega_2$) and difference-frequency (e.g. $\omega_1 - \omega_2$) generation and parametric scattering (e.g. $\omega_1 + \omega_2 - \omega_3$). The processes of difference-frequency generation and third-harmonic generation will be explored further in Chapters 3 and 4, respectively.

In this simplified analysis we have neglected the tensor nature of the susceptibilities ($\chi^{(1)}_{ij}$, $\chi^{(2)}_{ijk}$ and $\chi^{(3)}_{ijkl}$, where $ijkl \in xyz$. The tensor elements will depend on the intrinsic symmetry of the system and will typically set important constraints on the polarization of the incident electric fields in order to enable or maximize different nonlinear processes.

2.3 Cavity exciton-polaritons

Having introduced the basic properties of planar optical microcavities and of semiconductor excitons separately, we are now ready to revisit the system shown in Fig. 2.1a. We will see that the strong coupling of the light and matter components leads to the creation of hybrid quasiparticles called exciton-polaritons, which are part photon and part exciton.

In the nonrelativistic regime, the interaction energy of an electron with an electric field,

described by a vector field $\hat{A}$ in the Coulomb gauge, is given by [31]

$$\hat{H} = \frac{1}{2m_e}\left(\hat{p} + |e|\hat{A}\right)^2. \tag{2.46}$$

In addition to the kinetic energy of the electron, this Hamiltonian contains terms proportional to $\hat{p}\cdot\hat{A}$, representing the interaction of light and matter, and terms proportional to $\hat{A}^2$, describing a renormalization of the electric field. Similarly, we will represent the exciton-photon interaction Hamiltonian as [32]

$$\hat{H} = \hat{H}_{res} + \hat{H}_{antires} + \hat{H}_{A^2}. \tag{2.47}$$

The first two terms arise from the $\hat{p}\cdot\hat{A}$ contribution, where resonant (anti-resonant) terms couple states with same (opposite) in-plane momenta. The last term arises from the contribution of the squared vector potential and contains both resonant and anti-resonant terms. First, we will consider the strong coupling regime, where only the first term in Eq. (2.47) is non-negligible. Then, the full Hamiltonian will be discussed in the context of the ultrastrong coupling regime (USC). The extreme cases of weak and deep coupling will not be considered here but have been reviewed extensively in the literature [25, 33].

2.3.1 Strong coupling regime

The resonant term in Eq. (2.47) can be written as [34]

$$\hat{H}_{res} = \sum_k E_C(k)\hat{a}_k^\dagger\hat{a}_k + \sum_k E_X\hat{b}_k^\dagger\hat{b}_k + \sum_k \frac{\hbar\Omega_R}{2}\left(\hat{a}_k^\dagger\hat{b}_k + \hat{a}_k\hat{b}_k^\dagger\right), \tag{2.48}$$

where $E_C(k)$ is the cavity dispersion, E_X is the exciton energy,[1] $\hbar\Omega_R$ is the so-called Rabi splitting and $\hat{a}_k$ ($\hat{b}_k$) is the annihilation operator for a cavity photon (semiconductor exciton) with in-plane momentum k, which is a good quantum number due to the invariance of the system under in-plane translations. For simplicity, we will omit the $\|$ symbol. The first two terms in Eq. (2.48) correspond to the kinetic energies of the bare (uncoupled) particles, while the last corresponds to a coherent energy exchange process in which a photon is created (destroyed) and an exciton with the same wavevector (hence resonant) is destroyed (created).

[1] We neglect the dispersion of E_X because the exciton effective mass is several orders of magnitude larger than that of the cavity photon.

This Hamiltonian can be written in diagonal form [34]

$$\hat{H}_{Pres} = \sum_k E_P(k)\hat{p}_k^\dagger \hat{p}_k, \tag{2.49}$$

if we introduce a polariton annihilation operator $\hat{p}_k$ defined as [34]

$$\hat{p}_k = X(k)\hat{b}_k + C(k)\hat{a}_k. \tag{2.50}$$

To ensure the equivalence of the Hamiltonians, the complex coefficients $X(k)$ and $C(k)$ are chosen such that $\hat{p}_k$ satisfies Bose commutation relations

$$[\hat{p}_k, \hat{p}_k^\dagger] = |X(k)|^2 + |C(k)|^2 = 1 \tag{2.51}$$

and that [34]

$$[\hat{p}_k, \hat{H}_{Pres}] = [\hat{p}_k, \hat{H}_{res}], \tag{2.52}$$

for which we obtain

$$E_P(k)\left[X_k\hat{b}_k + C_k\hat{a}_k\right] = X(k)E_X\hat{b}_k + C(k)E_C(k)\hat{a}_k + \frac{\hbar\Omega_R}{2}\left[X(k)\hat{a}_k + C(k)\hat{b}_k\right]. \tag{2.53}$$

By comparing the coefficients of the single-particle operators, Eq. (2.53) can be recast in matrix form

$$\begin{pmatrix} E_P(k) - E_X & -\frac{\hbar\Omega_R}{2} \\ -\frac{\hbar\Omega_R}{2} & E_P(k) - E_C(k) \end{pmatrix} \begin{pmatrix} X(k) \\ C(k) \end{pmatrix} = 0. \tag{2.54}$$

Finally, by imposing that the determinant of Eq. (2.54) vanishes, we obtain the simple quadratic equation

$$[E_P(k) - E_X]\,[E_P(k) - E_C(k)] - \frac{\hbar^2\Omega_R^2}{4} = 0. \tag{2.55}$$

The two solutions are shown in Fig. 2.5a and describe the energy dispersion of the polariton modes

$$E_{P\pm}(k) = \frac{E_C(k) + E_X}{2} \pm \frac{1}{2}\sqrt{[E_C(k) - E_X]^2 + \hbar^2\Omega_R^2}, \tag{2.56}$$

where the positive and negative signs correspond to the upper (UP) and lower (LP) polariton modes or branches.

The quantities $X(k)$ and $C(k)$ are called Hopfield coefficients. The polariton exciton (photon) content is defined as the fraction of the matter (light) contribution to the polariton state and

is simply given by $|X(k)|^2$ ($|C(k)|^2 = 1 - |X(k)|^2$), which through Eqs. (2.54) and (2.56) can be expressed for the lower polariton mode as [34]

$$|X(k)|^2 = \frac{1}{1 + \left(\frac{\hbar\Omega_R}{2[E_{LP}(k) - E_C(k)]}\right)^2}. \tag{2.57}$$

The momentum dependence of the light and matter content is shown in Fig. 2.5b. On resonance, where $E_X = E_C(k_{res})$, the polariton modes are half light, half matter

$$|X(k_{res})|^2 = |C(k_{res})|^2 = \frac{1}{2} \tag{2.58}$$

and are separated in energy by the Rabi splitting

$$E_{UP}(k_{res}) - E_{LP}(k_{res}) = \hbar\Omega_R. \tag{2.59}$$

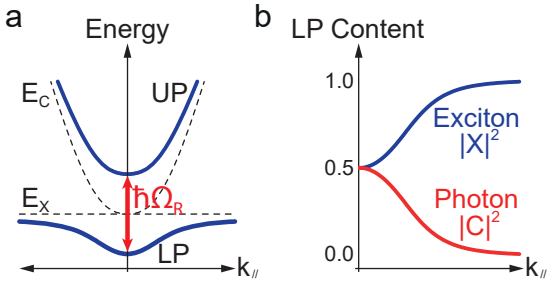

Figure 2.5 (a) Dispersion of the bare and polariton modes. In the example, the bare modes are resonant at normal incidence ($k_{\|} = 0$), where the polariton modes are separated in energy by the Rabi splitting $\hbar\Omega_R$. (b) Corresponding exciton and photon contents for the lower polariton mode. On resonance, the mode is half light-, half matter-like. At higher momenta, the LP becomes more exciton-like. The opposite behaviour occurs for the upper mode.

2.3.2 Ultrastrong coupling regime

We now consider the contributions of the last two terms in Eq. (2.47), namely [32]

$$\hat{H}_{antires} = \sum_k \frac{\hbar\Omega_R}{2} \left(\hat{a}_k \hat{b}_{-k} + \hat{a}_k^\dagger \hat{b}_{-k}^\dagger\right) \tag{2.60}$$

and

$$\hat{H}_{A^2} = \sum_k D\left(\hat{a}_k^\dagger \hat{a}_k + \hat{a}_k \hat{a}_k^\dagger + \hat{a}_k \hat{a}_{-k} + \hat{a}_k^\dagger \hat{a}_{-k}^\dagger\right). \tag{2.61}$$

The Hamiltonian $\hat{H}_{antires}$ contains the anti-resonant light-matter terms, which involve the creation and annihilation of particles with opposite in-plane momenta. The terms originating from the squared vector potential are contained in the Hamiltonian $\hat{H}_{A^2}$ and are proportional to the light-matter coupling constant $D = \hbar\Omega_R^2/4\omega_X$ ($\omega_X = E_X/\hbar$) [32]. This last Hamiltonian describes a renormalization of the electric field. Although this effect is typically observed in strongly driven systems (high electric field strength), here the field is renormalized as a consequence of the interaction with matter.

Neglecting the terms in Eqs. (2.60) and (2.61) is commonly known as the rotating wave approximation, which is valid when the light and matter systems are close to resonance ($E_C - E_X \ll E_C, E_X$) and the coupling between them is weak ($\hbar\Omega_R \ll E_C, E_X$). For an accurate description of systems in the ultrastrong coupling regime, where the normalized coupling strength ($\hbar\Omega_R/E_X$) is greater than ~ 0.1, the full Hamiltonian shown in Eq. (2.47) must be considered and a similar approach from Section 2.3.1 can be used to find the new eigenstates. The polariton annihilation operator is now defined as [32, 35]

$$\hat{p}_k = w(k)\hat{a}_k + x(k)\hat{b}_k + y(k)\hat{a}_{-k}^\dagger + z(k)\hat{b}_{-k}^\dagger \tag{2.62}$$

yielding a matrix Hamiltonian of the form [32]

$$\begin{pmatrix} E_C(k) + 2D - E_P(k) & \Omega_R/2 & 2D & \Omega_R/2 \\ \Omega_R/2 & E_X - E_P(k) & \Omega_R/2 & 0 \\ -2D & -\Omega_R/2 & -E_C(k) - 2D - E_P(k) & -\Omega_R/2 \\ -\Omega_R/2 & 0 & -\Omega_R/2 & -E_X - E_P(k) \end{pmatrix}. \tag{2.63}$$

In addition to an asymmetric anti-crossing behaviour, the presence of anti-resonant terms and of terms arising from the squared vector potential leads to a blueshift of the cavity mode, which through Eq. (2.57) increases the LP matter content, even on resonance. The normalization condition for the new polariton operator is given by [32]

$$|w(k)|^2 + |x(k)|^2 - |y(k)|^2 - |z(k)|^2 = 1, \tag{2.64}$$

where $y(k)$ and $z(k)$ are referred to as the anomalous Hopfield coefficients. A consequence of these terms is that the ground state of the system $|G\rangle$, which corresponds to the polariton

vacuum,

$$\hat{p}_{k(LP,UP)} \left|G\right\rangle = 0, \tag{2.65}$$

acquires a finite number of cavity photons and semiconductor excitons per mode [32]

$$\left\langle G\right| \hat{a}_k^\dagger \hat{a}_k \left|G\right\rangle = |y_{LP}(k)|^2 + |y_{UP}(k)|^2 \tag{2.66}$$

$$\left\langle G\right| \hat{b}_k^\dagger \hat{b}_k \left|G\right\rangle = |z_{LP}(k)|^2 + |z_{UP}(k)|^2. \tag{2.67}$$

It has been proposed that these virtual excitations may be released if the light-matter coupling strength can be modulated non-adiabatically [32]. The generated photons would then be expected to exhibit non-classical correlations and could be useful for the generation of correlated photon pairs.

In the past, the USC regime was only achieved when coupling to intersubband transitions in the mid-infrared part of the spectrum [36]. Today, organic microcavities with metallic mirrors show Rabi splittings of the order of ~ 1 eV and allow the USC regime to be easily achieved. The narrow linewidths observed in the USC regime have been employed as a means of obtaining narrow emission spectra and flat angular dispersions in light-emitting structures [20, 37], while the large Rabi splittings have been used to extend the spectral response of organic photodiodes [38]. The modification of material properties under strong and ultrastrong light-matter coupling is currently a subject of intense scientific interest and will be further addressed in Chapter 4 [39–41].

2.3.3 Semiclassical treatment

In this section, we address the system shown in Fig. 2.1a in a semiclassical way, where we treat the cavity field classically and maintain the exciton picture in the dielectric response of the medium. We begin by rewriting Eq. (2.7) to describe the dispersion of a planar microcavity filled with a semiconductor material with background refractive index $n = \sqrt{\epsilon_b}$,

$$\frac{\epsilon_b \omega_C^2}{c^2} = \left(\frac{q\pi}{L}\right)^2 + \left(k_\parallel\right)^2. \tag{2.68}$$

We now introduce an excitonic absorption, such that the relative permittivity obtained from Eq. (2.38) is given by

$$\epsilon_r(\omega) = \epsilon_b + \frac{A}{\omega_X^2 - \omega^2}, \tag{2.69}$$

where for simplicity we took $\gamma = 0$ and defined $A = \frac{Ne^2 f}{V m_e}$. The filled cavity dispersion is

given by [27]

$$\frac{\omega^2}{c^2}\left(\epsilon_b + \frac{A}{\omega_X^2 - \omega^2}\right) = \left(\frac{q\pi}{L}\right)^2 + \left(k_\parallel\right)^2, \tag{2.70}$$

where we obtain

$$\omega^2\left(\epsilon_b + \frac{A}{\omega_X^2 - \omega^2}\right) = \epsilon_b\omega_C^2. \tag{2.71}$$

This corresponds to the dispersion equation

$$\omega^4 - \omega^2(\omega_C^2 + \omega_X^2 + A/\epsilon_b) + \omega_C^2\omega_X^2 = 0, \tag{2.72}$$

which is identical to the one given by the full Hopfield Hamiltonian shown in Eq. (2.63) if we make the correspondence [27]

$$\hbar\Omega_R = \sqrt{4\hbar^2 A/\epsilon_b} = \sqrt{\frac{4\hbar^2 N e^2 f}{V m_e \epsilon_b}}. \tag{2.73}$$

We can see that the Rabi splitting scales as the square root of the oscillator strength and of the density of absorbers inside the cavity. Note that the same result is obtained through a complete quantum electrodynamics treatment of light-matter interaction [25].

2.4 Polariton nonlinearities

As we have seen in the previous section, exciton-polaritons are hybrid light-matter quasiparticles. On one hand, due to their photonic component, polaritons can be excited, manipulated and detected optically. On the other hand, the excitonic component of polaritons can lead to strong interparticle interactions. The resulting strong optical nonlinearities have allowed for the demonstration of many fascinating nonlinear effects. Here, we briefly review the mechanisms through which exciton-polaritons interact and discuss some of the main nonlinear experiments in planar microcavities.

2.4.1 Theory

At low densities, exciton-polaritons behave as ideal non-interacting bosons. At moderate densities, the bosonic treatment remains valid once fermionic effects are accounted for as an effective interaction between excitons (and polaritons) [34]. Using the same formalism as in Section 2.3, the effective exciton-exciton interaction Hamiltonian, corresponding to a

hard-sphere contact interaction, can be written in momentum space as [34]

$$\hat{H}_{XX} = \frac{1}{2}\sum_{k,k',q} V_q^{XX}\hat{b}^\dagger_{k+q}\hat{b}^\dagger_{k'-q}\hat{b}_k\hat{b}_{k'}, \tag{2.74}$$

where V_q^{XX} is the effective Coulomb interaction potential and k, k', q are 2D vectors. At high exciton densities, the Pauli exclusion principle leads to a saturation of the exciton-photon coupling, corresponding to a decrease in light absorption, and also referred to as phase-space filling (PSF). The resulting anharmonic interaction term is given by

$$\hat{H}_{XC}^{sat} = -\sum_{k,k',q} \frac{\hbar\Omega_R}{2n_{sat}}\hat{a}^\dagger_{k+q}\hat{b}^\dagger_{k'-q}\hat{b}_k\hat{b}_{k'} + \text{h.c.}, \tag{2.75}$$

where n_{sat} is the exciton saturation number. Considering the typical case when the LP mode is excited resonantly (or near resonance), these interaction Hamiltonians can be rewritten in terms of the LP operator defined in Eq. (2.62). The resulting polariton-polariton interaction Hamiltonian for the lower branch is given by [34]

$$\hat{H}_{PP} = \frac{1}{2}\sum_{k,k',q} V^{PP}_{k,k',q}\hat{p}^\dagger_{k+q}\hat{p}^\dagger_{k'-q}\hat{p}_k\hat{p}_{k'}. \tag{2.76}$$

The effective polariton-polariton interaction constant includes both exciton-exciton and saturation contributions [34]

$$V^{PP}_{k,k',q} = V_{XX}|X_{k+q}||X_{k'}||X_{k'-q}||X_k| + 2V_{SAT}(|C_{k+q}||X_{k'}| + |C_{k'}||X_{k+q}|)|X_{k'-q}||X_k|. \tag{2.77}$$

Since both contributions are positive, interactions between lower polaritons are repulsive and lead to a power-dependent blueshift $\Delta E_{LP}(k)$ of the polariton modes. This will play an important role in many of the nonlinear polariton effects which will be reviewed in the following sections.

The LP blueshift induced by the interaction Hamiltonian in Eq. (2.76) is given by [34]

$$\Delta E_{LP}(k) = \sum_{k'}(V^{PP}_{k,k',q=0} + V^{PP}_{k,k',q=k'-k})|\Psi_{k'}|^2, \tag{2.78}$$

where $|\Psi_{k'}|^2$ is the number of polaritons in each k state. This general equation can be used when different polariton states are resonantly excited by the pump. When only one k mode is excited, the blueshift can be described in terms of a single interaction constant in real

space coordinates [34]

$$\Delta E_{LP}(r) = g_{LP}|\Psi(r)|^2, \tag{2.79}$$

where $|\Psi(r)|^2$ is the polariton density at position r. This interaction constant can in turn be related to the individual exciton-exciton and PSF interaction mechanisms by [34]

$$g_{XX} = \frac{g_{LP}}{|X|^4} \tag{2.80}$$

and

$$g_{SAT} = \frac{g_{LP}}{4|C||X|^3}. \tag{2.81}$$

A powerful approach for modeling interacting polariton systems in the case of resonant, single-mode excitation is to describe the coherent LP field in real-space $\Psi(r,t)$ through a nonlinear partial differential equation called the Gross-Pitaevskii (GP) equation. In this mean-field description, quantum mechanical operators are replaced by their expectation values and the time dependence of the system is obtained from classical evolution equations [6]. The GP equation is given by [6]

$$i\hbar\frac{\partial\Psi(r,t)}{\delta t} = \left(\hbar\omega_0 - \frac{\hbar^2\nabla^2}{2m_{LP}} - \frac{i\gamma_{LP}}{2} + g_{LP}|\Psi(r,t)|^2\right)\Psi(r,t) + \hbar P(r,t), \tag{2.82}$$

where m_{LP} is the lower polariton effective mass, γ_{LP} is the decay rate, $\hbar\omega_0$ is the LP energy at $k = 0$ and $P(r,t)$ is the driving term. The GP equation provides accurate results as long as the occupation of modes other than the one resonantly pumped remains small. It can be modified to account for spin effects, important in quantum well and atomic monolayer dichalcogenide microcavities, and for the case of non-resonant pumping at higher energies, where it can be solved together with a rate equation describing the dynamics of the exciton reservoir [42].

2.4.2 Parametric scattering

We have seen that the dispersion of a bare cavity photon is approximately quadratic at low in-plane momenta. The same is true for bare excitons and the effective mass approximation is commonly applied. In contrast, polaritons have a non-parabolic dispersion that can enable new scattering mechanisms to take place. In the pioneering works of J. S. Roberts et al. [8, 9, 43], a quantum-well microcavity was pumped resonantly along the lower polariton mode and the angle of incidence was varied. When only the pump beam was incident,

polaritons were found to scatter into a wide range of final states along the LP dispersion via the interaction with phonons. Figure 2.6a shows the experimental LP dispersion measured in reflection in this configuration. Note that polaritons which have scattered into high momenta states appear weaker due to their low photonic content [43].

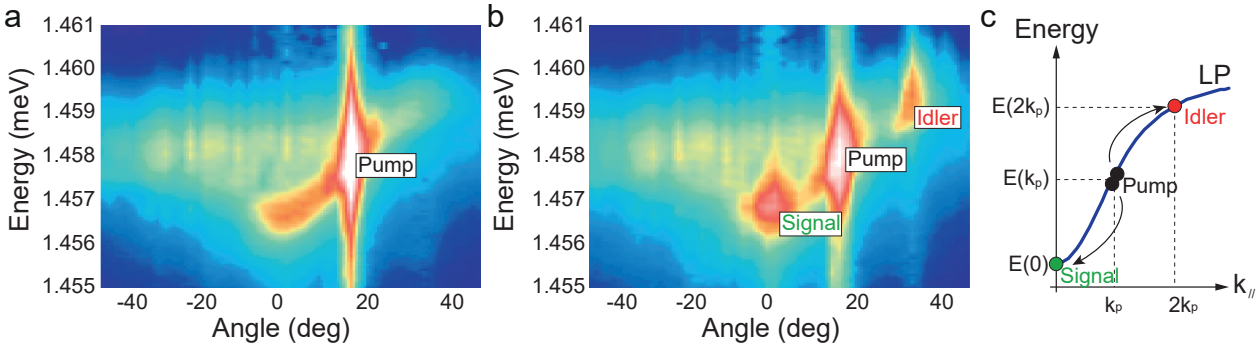

Figure 2.6 (a) Lower polariton dispersion illustrating the resonant pump (saturated in intensity) and the scattering of polaritons to a continuum of final states. (b) When a second weak signal beam is injected at normal incidence, it stimulates the pairwise scattering of polaritons to the signal mode and to a new idler mode to conserve energy and momentum. (c) Schematic of the pairwise scattering process. (a) and (b) adapted by permission from John Wiley and Sons: Physica Status Solidi b, "Parametric amplification and polariton liquids in semiconductor microcavities", J. J. Baumberg et al., Copyright © 2005 [43].

Next, a weak probe beam was directed at the sample and adjusted to be resonant with the LP mode at $k = 0$. Again, the pump angle of incidence was scanned and, at a specific angle, two surprising effects were observed: a drastic enhancement (gain) of the probe beam reflected by the cavity and the emergence of a new spectral component emitted at high momenta.

These results, shown in Fig. 2.6b, can be explained by a pairwise scattering process, schematized in Fig. 2.6c, in which two polaritons with momentum k_p undergo stimulated scattering into the state at $k = 0$, seeded by the probe beam, and into a high momentum state at $2k_p$, satisfying both energy and momentum conservation [43]

$$2E(k_p) = E(0) + E(2k_p). \tag{2.83}$$

The two points on the LP dispersion where polaritons accumulate are commonly referred to as signal ($k = 0$) and idler ($2k_p$), in an analogy with the optical parametric oscillator (OPO) in classical nonlinear optics. The pump angle of incidence where Eq. (2.83) is satisfied is referred to as the "magic angle" and corresponds to a triple phase-matching condition, which could only be achieved along the LP mode due to its peculiar shape. Note also that the strong

population of the pump, signal and idler states can also lead to stimulated scattering towards any combination of these states satisfying Eq. (2.83) [44]. The effective $\chi^{(3)}$ nonlinearity resulting from this polariton-polariton scattering process can be several orders of magnitude larger than those found in passive nonlinear materials, surpassing also the effective $\chi^{(3)}$ of OPOs based on cascaded $\chi^{(2)}$ nonlinearities [45]. As a consequence, microcavity polaritons have attracted considerable attention for enabling low-power nonlinear optical applications [45].

Parametric scattering has been demonstrated in inorganic microcavities up to a temperature of 220K, essentially limited by the binding energy of CdTe excitons [46]. So far, the smaller nonlinearities and lower power damage thresholds of organic semiconductors have prevented the observation of parametric interactions in this material set.

2.4.3 Condensation and lasing

Stimulated scattering of polaritons is possible due to the bosonic nature of the constituent quasiparticles. The peculiar shape of the LP mode favors the relaxation towards the bottom of the polariton dispersion, which by itself can trigger stimulated scattering into this state. Consider the case where a microcavity is pumped non-resonantly at a high energy. A reservoir of hot excitons is created, which subsequently relaxes into polaritons, followed by scattering into different final states. Below a certain intensity threshold, the light emitted from the cavity is incoherent and follows thermal statistics, as all coherence inherited from the pump is lost in the reservoir. Above threshold, however, stimulated scattering into the LP ground state at $k = 0$ can take place [47]. This spontaneous symmetry breaking leads to the creation of a coherent signal field with long-range order [48]. Due to the short polariton lifetimes (typically < 1 ps), this new state behaves as a non-equilibrium Bose-Einstein condensate (rigorously, a 2D system goes through a Berezinskii-Kosterlitz-Thouless transition [25]).

The first conclusive demonstration of polariton Bose-Einstein condensation (BEC) was performed by Kasprzak et al. [48] in a CdTe quantum well microcavity at 5K. Figure 2.7a shows the real space emission from the excitation spot when the pump intensity is swept across the condensation threshold. The corresponding momentum space patterns illustrating the population distribution along the LP mode are shown in Fig 2.7b. Below threshold, polaritons occupy a range of k states and the real space pattern has a smooth profile. When the intensity is increased above threshold, the momentum distribution shrinks towards the ground state and a sharp peak in real space is seen, corresponding to polaritons with $k_{\|} = 0$.

This threshold is termed the polariton lasing threshold as it does not rely on population inversion and because the sample is still in the strong coupling regime [49]. When the pump

intensity is increased further, the conventional lasing threshold can be found, which for this system was 50 times higher than the polariton one. Thus, polariton lasing could enable the fabrication of coherent light sources operating at much lower powers.

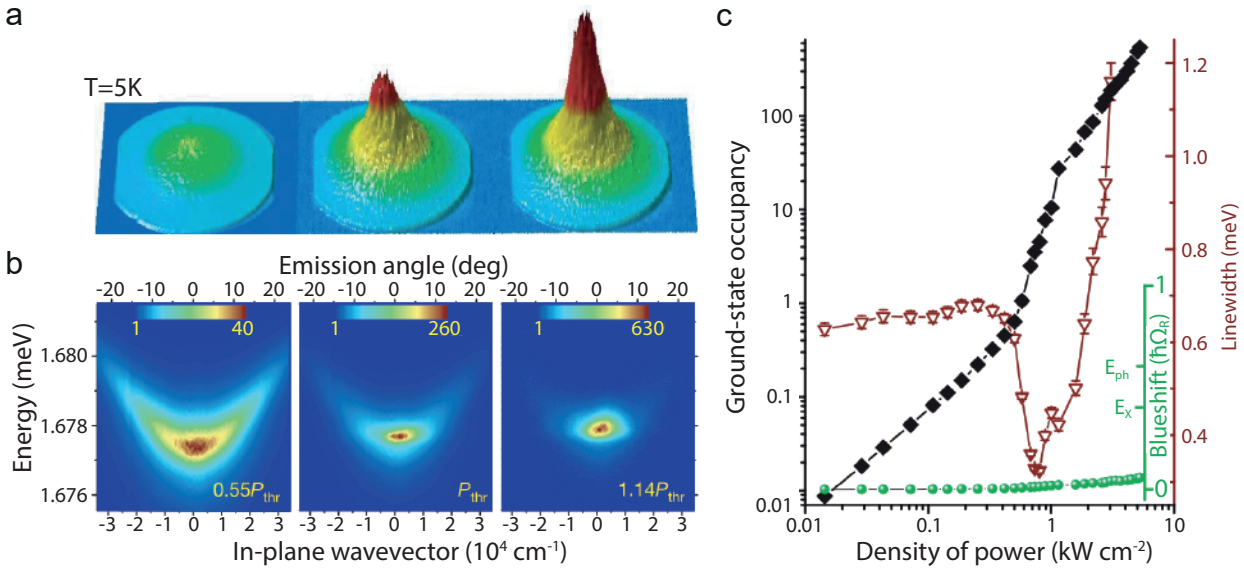

Figure 2.7 (a) Real and (b) momentum space images of a polariton fluid across the condensation threshold. In real space, bright emission can be seen coming from polaritons with zero in plane momentum. In momentum space, polaritons collapse to the bottom of the LP dispersion, which is blueshifted by the polariton-polariton and polariton-exciton interactions. (c) Ground-state occupancy which increases exponentially above unity due to stimulated scattering (black), LP linewidth (brown) and LP blueshift (green). Adapted by permission from Springer Nature: Nature, "Bose-Einstein condensation of exciton polaritons", J. Kasprzak et al., Copyright © 2006 [48].

Figure 2.7c shows additional features of the polariton condensate. The black curve shows the ground state occupancy, which displays an exponential increase above unity, a signature of bosonic stimulated scattering. The brown curve shows that the polariton linewidth decreases above threshold, a consequence of the increased coherence, but increases again at high excitation due to decoherence caused by polariton interactions. The green curve traces the blueshift of the polariton mode, another consequence of polariton-polariton and polariton-exciton interactions, which for this system was found to be below 10% of the Rabi splitting. The blueshift of the polariton modes can also be seen as an intensity-dependent vertical shift of the dispersions in Fig 2.7b.

Polariton condensation has since been observed in different geometries, material sets and also at room temperature and under electrical excitation [12–14, 42, 50–57]. In addition, polariton

condensates have allowed for the demonstration of a number of interesting nonlinear effects, such as the propagation of solitons and the formation of quantized vortices [58, 59].

2.4.4 Optical limiting and bistability

The blueshift plays an important role in the different nonlinear processes. In parametric scattering under resonant excitation, the signal and idler condensates are created on states along the blue-shifted dispersion. Under quasi-resonant excitation, drastically different regimes will be encountered if the pump energy is on the low or high energy side of the unperturbed dispersion.

First, consider the case when the cavity is driven by a coherent continuous wave pump with a slight red detuning from the LP mode. As the pump intensity is increased, the blueshift pushes the dispersion away from the pump energy and more out of resonance. The growth of the polariton density, and consequently of the blueshift, is therefore sub-linear. This behavior is known as optical limiting and is illustrated in Fig. 2.8a.

When the pump has a slight blue detuning with respect to the LP mode, the blueshift can bring them into resonance. This positive feedback mechanism is shown in Fig. 2.8b. As the pump intensity is increased along the lower portion of the curve, only a small blueshift is observed. Upon reaching the A high intensity threshold, the feedback becomes strong enough and the system jumps to point B along the upper curve to lock the blueshifted dispersion to the pump energy. As the intensity is increased further above B, the optical limiting behavior is recovered. When the intensity is decreased from B, the blueshift is maintained as long as the polariton population is high enough. Upon reaching the C low intensity threshold, the system jumps back to the lower portion of the curve towards point D. Because the high and low intensity thresholds are distinct, a hysteresis loop is observed and the system is said to be bistable. Polariton bistability is the result of a $\chi^{(3)}$ nonlinearity. At normal incidence or when only one mode is involved, it is associated to the polariton Kerr effect [11, 62], a reference to the optical analogue in which changes in the pump intensity lead to a change in refractive index. Figure 2.8c shows a different type of polariton bistability observed in the polariton OPO regime in an InGaAs/GaAs microcavity at cryogenic temperatures [61]. In this case, the pump shifts the dispersion such that triply-resonant oscillation becomes possible and the hysteresis loop is observed in the signal condensate.

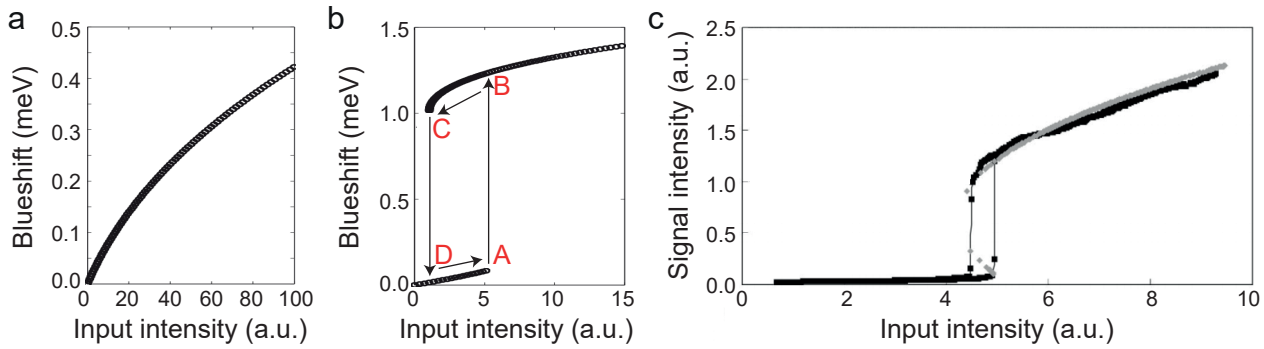

Figure 2.8 Theoretical LP blueshift when the pump is red (a) and (b) blue detuned from the LP mode in the low excitation regime. In (a) the blueshift brings the mode more out of resonance with the pump and the observed blueshift increases sublinearly with power. This is the optical limiter regime. In (b), the blueshift can bring the LP mode into resonance with the pump and a sudden increase in the blueshift is observed (from point A to point B). Hysteresis is observed when decreasing the power and a second jump in the blueshift is seen (C to D) when the pump intensity can no longer maintain the high polariton density. This is the bistable behavior. (c) Experimental demonstration of the polariton bistable regime. When the pump intensity is increased, the LP mode blueshifts and allows for stimulated scattering to occur. The bistability was observed in the intensity of the signal condensate. (a) and (b) adapted by permission from John Wiley and Sons: Physica Status Solidi b, "Quantum fluid effects and parametric instabilities in microcavities", C. Ciuti et al., Copyright © 2005 [60] and (c) adapted by permission from American Physical Society: Physical Review B, "Optical bistability in semiconductor microcavities in the nondegenerate parametric oscillation regime: Analogy with the optical parametric oscillator", A. Baas et al., Copyright © 2004 [61].

2.4.5 Superfluidity

The Gross-Pitaevskii equation can be used to describe the steady state behavior of a polariton condensate. A linear stability analysis can then be performed when the condensate is subjected to weak perturbations. The resulting dispersions are called Bogoliubov modes and describe the spectrum of the collective excitations supported by the condensate [60, 63]. As we will see in Chapter 5, this analysis shows that there exists a regime where the Bogoliubov modes become so distorted that $\omega_{LP}(k) > \omega_{pump}$ for every $k \neq k_{pump}$. In this regime, there are no final states available for resonant or elastic scattering to take place. The condensate can flow unperturbed and behaves as a superfluid. For the Landau superfluidity criterion to be satisfied, it is necessary for elastic scattering to take place in the low excitation regime (no or small blueshift) and therefore $\omega_{pump} > \omega_{LP}(0)$.

Figure 2.9a shows real space images of a polariton condensate flowing against a defect as the

polariton density is increased above the superfluidity threshold. Below threshold, interference fringes are formed in front of the obstacle as a result of counter-propagating waves and the region behind the obstacle is dark. At threshold, superfluidity is achieved in the center of the Gaussian excitation spot only where the intensity is highest. A reduction in the number of fringes can be seen, as well as an increase in polariton density behind the defect. At high intensity, superfluidity is achieved over the entire illumination area and the interference fringes disappear. The condensate can be seen to flow around the obstacle without scattering. The transition to the superfluid behavior can also be seen in the momentum space images shown in Fig. 2.9b. In the low excitation regime, resonant Rayleigh scattering leads to the appearance of a ring in momentum space. Above threshold, the ring shrinks and eventually collapses towards the pump position in momentum space.

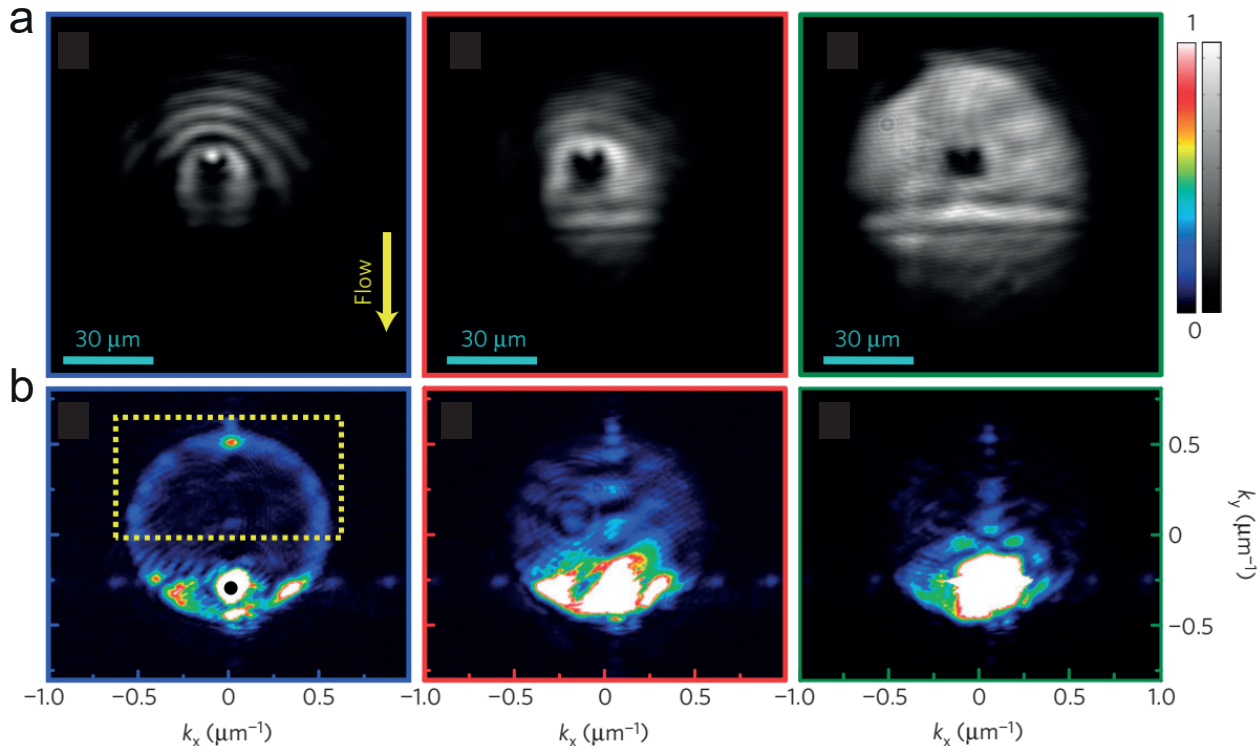

Figure 2.9 (a) Real and (b) momentum space images of a polariton fluid moving against an obstacle across the superfluidity threshold. In real space, the linear regime is marked by interference fringes in front of the obstacle and a dark region behind it. In the superfluid regime, the density becomes uniform around the obstacle and the fluid flows unperturbed. In momentum space, the linear regime is marked by a resonant Rayleigh scattering ring. In the superfluid case, the ring collapses towards the pump excitation spot as scattering becomes suppressed. Adapted by permission from Springer Nature: Nature Physics, "Superfluidity of polaritons in semiconductor microcavities", A. Amo et al., Copyright © 2009 [64].

The interaction-induced sound velocity in the polariton fluid is given by [60]

$$c_s = \sqrt{\hbar g_{LP} |\Psi|^2 / m_{LP}} \tag{2.84}$$

and for the superfluid regime to be achieved it must be larger than the condensate flow velocity imparted by the pump [60]

$$v_p = \hbar k_p / m_{LP}. \tag{2.85}$$

Therefore, this regime is more easily achieved for low group velocities and in systems where the polariton-polariton nonlinearity is high, such as in inorganic quantum well microcavities, or in systems where the polariton density can be very high without a transition into weak-coupling, such as in organic microcavities. In Chapter 5 we will discuss a recent demonstration of superfluid behavior in an organic microcavity at room temperature [21].

2.4.6 Harmonic generation

As a final example of polariton nonlinearities, which are typically of a $\chi^{(3)}$ type, we will consider the case of second harmonic generation in a microcavity embedding an organic dye possessing a large $\chi^{(2)}$ nonlinearity [65]. Second-order nonlinear processes involving polariton modes have remained largely unexplored and will be considered in more detail in Chapter 3.

Consider a metallic microcavity designed such that the second cavity mode is strongly coupled to an exciton absorption, as shown in Fig. 2.10a. The cavity is pumped at low energies in the near infrared and the pump energy is scanned across the first polariton mode, which is a doublet due to birefringence. These modes are mostly photonic due to the significant detuning to the exciton transition. The intensity of the SHG generated from the cavity is shown in Fig. 2.10b and is found to peak when the energy of the second harmonic matches that of the upper and lower polariton modes. The observed behavior is different for a bare material, as shown in in Fig. 2.10c, where the SHG intensity peaks when the energy of the harmonic matches the exciton transition (resonant SHG). When the transmission of the mirrors and the field enhancement experienced by the pump and SHG fields were taken into account, it was concluded that the presence of polariton states enhanced the $\chi^{(2)}$ response of the material. Finally, the LP SHG was found to be stronger than the UP one, what was consistent with the higher photonic content of the lower polaritons at the experimental cavity detuning.

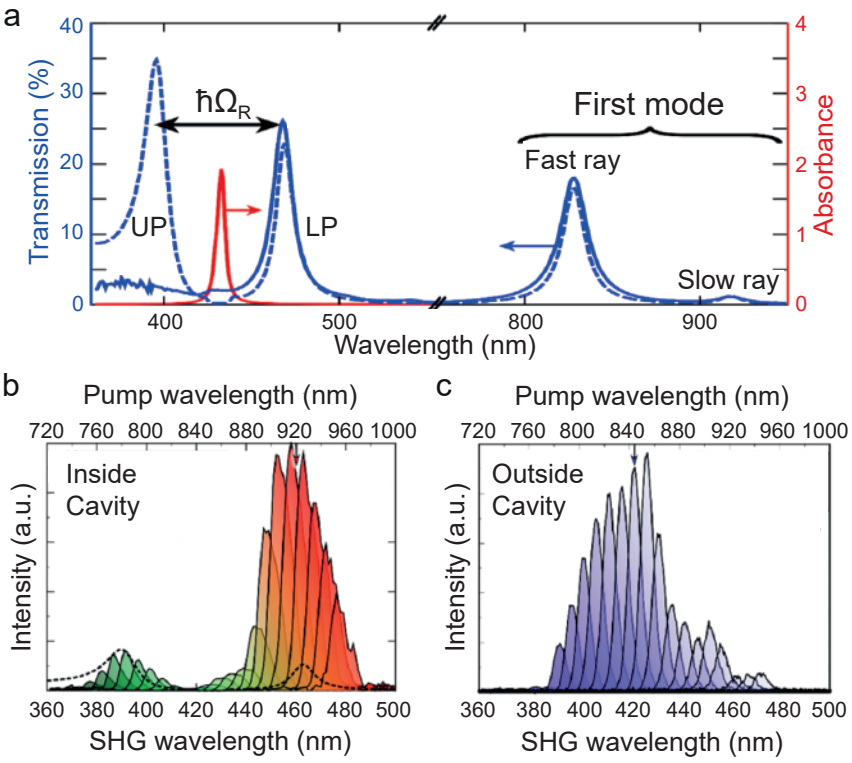

Figure 2.10 (a) Transmission of the polariton modes (blue) and absorbance of the organic dye (red). The pump is scanned in the near infrared over the first mode (a doublet due to birefringence). (b) Intensity of the SHG as a function of pump excitation wavelength for the case of a microcavity and (c) for a bare organic layer. In (b) the black lines indicate the transmission of the polariton modes. Adapted with permission from American Chemical Society: Nano Letters, "High-efficiency second-harmonic generation from hybrid light-matter states", T. Chervy et al., vol. 16, no. 12, pp. 7352–7356. Copyright © 2016 [66].

CHAPTER 3 GENERATION OF RABI-FREQUENCY RADIATION USING EXCITON-POLARITONS

3.1 Introduction

As introduced in Chapter 2, cavity exciton-polaritons are hybrid light-matter quasiparticles that result from the mixing between an exciton transition and a Fabry-Perot cavity photon. The minimum energetic difference between the lower and upper polariton modes, called the Rabi splitting, can range from a few meV in inorganic semiconductors to ~ 1 eV in organic ones [27, 48, 54, 67, 68]. Therefore, radiative transitions from the upper to the lower polariton branch, as shown in Fig. 3.1, can provide a simple route towards tunable infrared (IR) and terahertz (THz) generation.

Such transitions can be understood as resulting from a strongly coupled $\chi^{(2)}$ nonlinear interaction in which two photons, dressed by the resonant interaction with excitons, interact emitting a third photon. As a consequence of the usual $\chi^{(2)}$ symmetry requirement, such polariton-polariton transitions are forbidden in centrosymmetric systems. To overcome this issue several solutions have been proposed, including the use of asymmetric quantum wells [69, 70], the mixing of polariton and exciton states with different parity [71, 72] and the use of transitions other than UP to LP [73, 74].

In this chapter, we study the use of non-centrosymmetric semiconductors, possessing an intrinsic second-order susceptibility $\chi^{(2)}$, to allow for the generation of Rabi-frequency radiation. For the case where the UP and LP branches are driven by two incident pump waves, the irradiance of the resulting radiation is identical to classical difference-frequency generation. Using a semiclassical model, we show that the DFG irradiance is enhanced by nearly four orders of magnitude compared to bare $\chi^{(2)}$ nonlinearity. Although here we consider DFG, a similar enhancement is expected for the case of parametric fluorescence, which does not require a LP pump wave. Finally, we highlight the use of a triply-resonant scheme to obtain

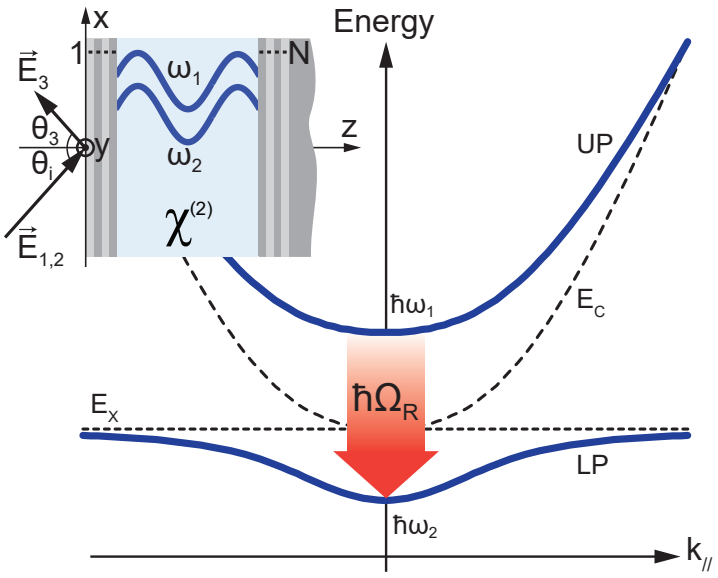

Figure 3.1 Dispersion relation of exciton-polaritons as a function of in-plane wavevector. The interaction between an exciton transition (E_X) and a Fabry-Perot cavity mode (E_C), both represented by dashed lines, leads to the appearance of lower and upper polariton branches (solid blue). A radiative transition at the Rabi energy ($\hbar\Omega_R$) occurs between two incident pumps at frequencies ω_1 and ω_2 through difference-frequency generation in a second-order nonlinear semiconductor ($\chi^{(2)} \neq 0$). Inset: microcavity showing the two pump beams ($\vec{E}_{1,2}$), incident at angle θ_i, and the Rabi radiation ($\vec{E}_3$), reflected at angle θ_3. The solid blue lines in the $\chi^{(2)}$ layer illustrate the high modal overlap of polariton fields. Layers are numbered from 1 (air) to N (substrate) for the transfer matrix formalism.

polariton optical parametric oscillation.

Semiconductor microcavities are advantageous for nonlinear optical mixing due to their ability to spatially and temporally confine the interacting fields. In contrast to conventional nonlinear optical crystals, which require birefringence or quasi-phase-matching, the efficiency of the nonlinear process does not depend on phase-matching for small interaction lengths, but instead on maximizing the field overlap [75]. To overcome mode orthogonality, while simultaneously satisfying the symmetry requirements of the $\chi^{(2)}$ tensor, a number of strategies have been proposed, such as mode coupling between crossed-beam photonic crystal cavities with independently tunable resonances [76–78] and the use of single cavities supporting both TE and TM modes [79, 80]. Exciton-polaritons provide a simple solution to this problem because they arise from coupling to a single cavity mode and thus naturally display good modal overlap. Many of the fascinating effects observed in strongly-coupled semiconductor microcavities exploit this property, but these have been principally limited to the resonant

$\chi^{(3)}$ nonlinearity inherited from the exciton. Examples include stimulated polariton scattering [8, 9], parametric oscillation [10, 81, 82], optical bistability [11], condensation and superfluidity [21, 48, 64].

3.2 Nonlinear transfer matrix method

To calculate the propagation of the incident pump fields and the difference-frequency contribution due to nonlinear layers, we use the nonlinear transfer matrix method introduced by Bethune [83]. This method is applicable to structures with an arbitrary number of parallel nonlinear layers [84–86], but is restricted to the undepleted pump approximation, where the three fields are essentially independent. First, we propagate the incident pump fields using the standard transfer matrix method. Within each nonlinear layer, these behave as source terms in the inhomogeneous wave equation. Then, we solve for the particular solution and determine the corresponding source field vectors. Finally, we use the boundary conditions and propagate the free fields using the transfer matrix method to obtain the total field in each layer.

3.2.1 Propagation of the pump fields

We begin by calculating the field distribution of the two incident pumps as shown in Fig. 3.1 by using the standard transfer matrix method [87–89]. To simplify the discussion, we consider the pumps to be TE ($\hat{y}$) polarized. In our notation, the electric field in each layer i is given by sum of two counter-propagating plane waves

$$\mathcal{E}_i(z,x,t) = \mathrm{Re}\left\{E_i^+ \exp[i(k_{iz}z + k_x x - \omega t)] + E_i^- \exp[i(-k_{iz}z + k_x x - \omega t)]\right\}, \tag{3.1}$$

where the k_{iz} and k_x components of the $\vec{k_i}$ wavevector satisfy the relationship $k_{iz}^2 + k_x^2 = n_i^2(\omega)\,\omega^2/c^2$, with n_i the refractive index of layer i. The forward and backward complex amplitudes of the electric field are represented in vector form as $\mathbf{E}_i = \begin{bmatrix} E_i^+ & E_i^- \end{bmatrix}^T$.

For a given incident field $\mathbf{E}_1$, the field in layer i is calculated by $\mathbf{E}_i = T_i\mathbf{E}_1$, where T_i is the partial transfer matrix

$$T_i = M_{i(i-1)}\phi_{i-1}\cdots M_{21}. \tag{3.2}$$

The interface matrix M_{ij}, that relates fields in adjacent layers i and j at the interface, and the propagation matrix ϕ_i, that relates fields on opposite sides of layer i with thickness d_i,

are given by

$$M_{ij} = \frac{1}{2k_{iz}} \begin{bmatrix} k_{iz} + k_{jz} & k_{iz} - k_{jz} \\ k_{iz} - k_{jz} & k_{iz} + k_{jz} \end{bmatrix} \tag{3.3}$$

and

$$\phi_i = \begin{bmatrix} \exp(ik_{iz}d_i) & 0 \\ 0 & \exp(-ik_{iz}d_i) \end{bmatrix}. \tag{3.4}$$

3.2.2 Inclusion of nonlinear polarizations

To obtain the difference-frequency contribution within a nonlinear layer, we must solve the inhomogeneous wave equation for the electric field

$$\nabla^2 \mathcal{E} - \mu\epsilon \frac{\partial^2 \mathcal{E}}{\partial t^2} = \mu \frac{\partial^2 \mathcal{P}^{NL}}{\partial t^2}, \tag{3.5}$$

where the source term

$$\mathcal{P}^{NL}(z, x, t) = \epsilon_0 \chi^{(2)} \mathcal{E}^2(z, x, t) \tag{3.6}$$

is the second-order nonlinear polarization, μ is the magnetic permeability and ϵ the permittivity. By using a polarization term of the same form as Eq. (3.1), Eq. (3.5) can be written in the frequency domain as

$$\left[-(k^{NL})^2 + \omega_{NL}^2 n^2(\omega_{NL})\mu_0\epsilon_0\right] \mathbf{E} = -\omega_{NL}^2 \mu_0 \mathbf{P}^{NL}, \tag{3.7}$$

with wavevector k^{NL}, $\mu(\omega_{NL}) = \mu_0$ and $\epsilon(\omega_{NL}) = n^2(\omega_{NL})\epsilon_0$. The nonlinear polarization thus generates a bound source field at the same frequency given by

$$\mathbf{E}_s = \frac{\mathbf{P}^{NL}}{\frac{(k^{NL})^2}{\omega_{NL}^2 \mu_0} - n^2(\omega_{NL})\epsilon_0}. \tag{3.8}$$

If we consider the presence of two pump fields $\mathbf{E}_1(\omega_1)$ and $\mathbf{E}_2(\omega_2)$, with $\omega_1 > \omega_2$, the $\mathcal{E}^2(z, x, t)$ term in Eq. (3.6) can be written as

$$\begin{aligned} \mathcal{E}^2(z, x, t) = \mathrm{Re}\Big\{ & E_1^+ \exp\left[i\left(k_z^1 z + k_x^1 x - \omega_1 t\right)\right] + E_1^- \exp\left[i\left(-k_z^1 z + k_x^1 x - \omega_1 t\right)\right] \\ & + E_2^+ \exp\left[i\left(k_z^2 z + k_x^2 x - \omega_2 t\right)\right] + E_2^- \exp\left[i\left(-k_z^2 z + k_x^2 x - \omega_2 t\right)\right]\Big\}^2. \end{aligned} \tag{3.9}$$

Expanding $\mathcal{E}^2(z, x, t)$ leads to terms related to frequency doubling ($\omega_{NL} = 2\omega_1$ or $2\omega_2$) and rectification ($\omega_{NL} = 0$), sum-frequency ($\omega_{NL} = \omega_1 + \omega_2$) and difference-frequency generation

($\omega_{NL} = \omega_1 - \omega_2$). The terms contributing to the latter ($\equiv \omega_3$) are given by

$$\begin{aligned}\mathcal{P}^3(z,x,t) = \epsilon_0\chi^{(2)}\,\mathrm{Re}\Big\{\Big(&E_1^+E_2^{+*}\exp\left[i\left(k_z^1 - k_z^2\right)z\right]\\ &+E_1^+E_2^{-*}\exp\left[i\left(k_z^1 + k_z^2\right)z\right]\\ &+E_1^-E_2^{+*}\exp\left[-i\left(k_z^1 + k_z^2\right)z\right]\\ &+E_1^-E_2^{-*}\exp\left[-i\left(k_z^1 - k_z^2\right)z\right]\Big)\\ &\times\exp\left(i\left[\left(k_x^1 - k_x^2\right)x - \omega_3 t\right]\right)\Big\}.\end{aligned} \tag{3.10}$$

Co-propagating waves $(\pm,\pm)$ generate terms with perpendicular wavevector $k_z^{3-} = k_z^1 - k_z^2$, whereas counter-propagating waves $(\pm,\mp)$ generate terms with $k_z^{3+} = k_z^1 + k_z^2$. Their contributions can be handled separately when pump depletion is ignored, so we divide the polarization term into two components

$$\mathbf{P}^{3-} = \epsilon_0\chi^{(2)}\begin{bmatrix}E_1^+E_2^{+*}\\ E_1^-E_2^{-*}\end{bmatrix} \tag{3.11a}$$

$$\mathbf{P}^{3+} = \epsilon_0\chi^{(2)}\begin{bmatrix}E_1^+E_2^{-*}\\ E_1^-E_2^{+*}\end{bmatrix}, \tag{3.11b}$$

with their source fields given by Eq. (3.8) and the perpendicular component of k^{NL} taking the values of k_z^{3-} or k_z^{3+}, respectively.

In addition to the bound fields, there are also free fields with frequency ω_3 that are solutions to the homogeneous wave equation. The free field in a nonlinear layer j is obtained from the bound field amplitudes $\mathbf{E}_{js}$ and the boundary conditions at the interfaces. By imposing continuity of the total tangential electric and magnetic fields across interfaces i–j and j–k, an effective free field source vector can be defined as

$$\mathbf{S}_j = \left(\phi_j^{-1}M_{js}\phi_{js} - M_{js}\right)\mathbf{E}_{js}. \tag{3.12}$$

The source matrices with the subscript s, M_{js} and ϕ_{js}, are identical to the ones given by Eqs. (3.3) and (3.4), with k_{iz} and k_{jz} taking the values of k_{jz}^3 and $k_{jz}^{3\pm}$, respectively. These matrices use only source layer indices and involve optical constants at all three optical frequencies (pumps and DFG). They relate the free fields that propagate with wavevector $k_{jz}^3 = n_j(\omega_3)\omega_3/c$ to the bound fields with wavevectors $k_{jz}^{3\pm} = [n_j(\omega_1)\omega_1 \pm n_j(\omega_2)\omega_2]/c$.

The total nonlinear field is then given by the sum of independent source field vectors $\mathbf{S}_j$ propagated using the transfer matrix method reviewed in Sec 3.2.1. In particular, for the case where only layer j is nonlinear, we obtain

$$\begin{aligned}\begin{bmatrix} E_{3T} \\ 0 \end{bmatrix} &= M_{N(N-1)} \cdots M_{21} \begin{bmatrix} 0 \\ E_{3R} \end{bmatrix} + M_{N(N-1)} \cdots M_{(j+1)j} \mathbf{S}_j \\ &= T_N \begin{bmatrix} 0 \\ E_{3R} \end{bmatrix} + \begin{bmatrix} R_j^+ \\ R_j^- \end{bmatrix},\end{aligned} \tag{3.13}$$

with

$$\mathbf{R}_j = T_N {T_j}^{-1} \mathbf{S}_j. \tag{3.14}$$

Therefore, the reflected and transmitted components of the $\mathbf{E}_3$ field can be calculated by

$$E_{3R} = -\frac{R_j^-}{T_{22}} \tag{3.15a}$$

$$E_{3T} = R_j^+ - \frac{T_{12}}{T_{22}} R_j^-. \tag{3.15b}$$

The angle dependence of the reflected difference-frequency field can be expressed as

$$|k_3| \sin\theta_3^{\pm} = |k_1| \sin\theta_1 \pm |k_2| \sin\theta_2, \tag{3.16}$$

where the $\pm$ sign must match the wavevector component $k_z^{3\pm}$ when both pumps are incident on the same side of the normal [90]. Because the first layer is taken to be air with $n(\omega) = 1$, if we consider both pumps to be incident with the same angle $\theta_1 = \theta_2 = \theta_i$, we obtain for the cases of k_z^{3-} and k_z^{3+}

$$\sin\theta_3^- = \frac{\omega_1 \sin\theta_i - \omega_2 \sin\theta_i}{\omega_1 - \omega_2} = \sin\theta_i \tag{3.17a}$$

$$\sin\theta_3^+ = \left(\frac{\omega_1 + \omega_2}{\omega_1 - \omega_2}\right) \sin\theta_i. \tag{3.17b}$$

Equation (3.17a) shows that the DFG component due to co-propagating waves exits the structure at the same angle as the incident pumps, resembling the law of reflection. Conversely, according to Eq. (3.17b), the component due to counter-propagating waves is sensitive to deviations of the pump waves from normal incidence. In particular, for low DFG frequencies, the $(\omega_1 + \omega_2)/(\omega_1 - \omega_2)$ term is much larger than unity and this component easily becomes evanescent.

3.3 DFG in an organic polymer cavity

In this section, we investigate the use of organic microcavities for Rabi frequency generation. Due to the large binding energy of Frenkel excitons, organic microcavities can readily reach the strong coupling regime at room temperature and have shown Rabi splittings of up to 1 eV [27, 67]. Demonstrations of optical nonlinearities have been more limited than in their inorganic counterparts, but a variety of resonant [21, 91, 92] and non-resonant nonlinearities [12, 50, 51] have nevertheless been observed in these systems.

Although most organic materials possess a negligible second-order susceptibility, a number of poled nonlinear optical (NLO) chromophores have been shown to exhibit high electro-optic coefficients that exceed those of conventional nonlinear crystals such as $LiNbO_3$ by over an order of magnitude [30, 93]. In addition, the metallic electrodes needed for polling can also be used as mirrors, providing high mode confinement and a means for electrical injection.

We will consider a thin NLO polymer film enclosed by a pair of metallic silver mirrors of thicknesses 10 nm (front) and 100 nm (back). The model polymer is taken to possess a dielectric constant described by a single Lorentz oscillator

$$\epsilon(\omega) = \epsilon_b + \frac{f{\omega_0}^2}{{\omega_0}^2 - \omega^2 - i\gamma\omega}. \tag{3.18}$$

Similar to Eq. (2.39), here ϵ_b is the background dielectric constant, f is the oscillator strength, ω_0 is the frequency of the optical transition and γ its full width at half maximum. The parameters are chosen to be $\epsilon_b = 4.62$, $f = 0.91$, $\hbar\omega_0 = 1.55$ eV and $\hbar\gamma = 0.12$ eV. Experimental values are used for the refractive index of silver [94]. For simplicity, we ignore the dispersive nature of the second-order nonlinear susceptibility and take $\chi^{(2)} = 300$ pm/V. In principle, the Lorentz model could readily be extended to account for the dispersive resonant behavior as in Eq. (2.44) [30].

Figure 3.2 shows the linear reflectance, calculated at normal incidence, as a function of polymer film thickness. The reflectance for film thicknesses below 200 nm shows only the fundamental cavity mode (M1), which is split into UP and LP branches. For these branches, the Rabi energy falls below the LP branch, where there are no further modes available for difference-frequency generation.

By increasing the thickness of the film, low-order modes shift to lower energies and provide a pathway for the DFG radiation to escape. For example, at 300 nm, a triple-resonance condition occurs where the Rabi splitting of the M2 cavity mode matches the M1 energy ($E_{UP} - E_{LP} = \hbar\Omega_R = E_{M1} = 0.68$ eV). A second resonance occurs between M3 and LP

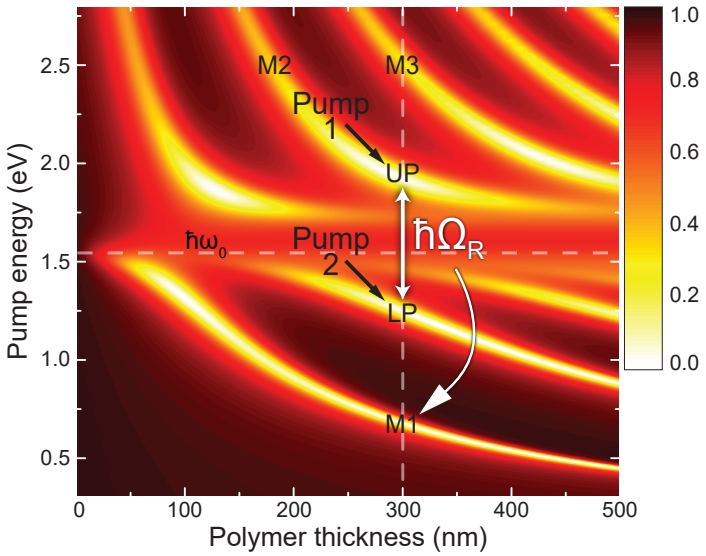

Figure 3.2 Reflectance as a function of pump energy and thickness of the polymer film. Front and back Ag mirrors have thicknesses of 10 nm and 100 nm, respectively. Dielectric parameters: $\epsilon_b = 4.62$, $f = 0.91$, $\hbar\omega_0 = 1.55$ eV, $\hbar\gamma = 0.12$ eV and $\chi^{(2)} = 300$ pm/V. Dashed horizontal line indicates the exciton energy. At the thickness of 300 nm, indicated by a vertical dashed line, the M1 cavity mode is resonant with the difference-frequency generation of pumps 1 and 2 such that $E_{UP} - E_{LP} = \hbar\Omega_R = E_{M1}$.

because $E_{M3} - E_{LP} = E_{LP} = 1.25$ eV, but with reduced modal overlap.

The enhancement in DFG irradiance from the microcavity, as compared to a bare nonlinear slab, is shown in Fig. 3.3 as a function of the pump energies. The two peaks correspond to the triple-resonance conditions mentioned above, where the left peak corresponds to an enhancement of $2.8 \cdot 10^2$ at the Rabi energy ($\lambda_3 = 1.82$ μm) and the right peak to an enhancement of $3.3 \cdot 10^2$ at the LP energy ($\lambda_{LP} = 996$ nm). The apparent contradiction of a higher DFG enhancement in the case of reduced modal overlap arises from normalizing each point by the corresponding DFG irradiances of the bare polymer slab.

The inset shows the normalized electric field profiles of the relevant modes, which highlight the good modal overlap of the two pump fields in the strong-coupling regime. The small thickness of the front metallic mirror lowers the mutual orthogonality of different modes and accounts for the lack of symmetry of the fields with respect to the center of the film. This loss of orthogonality allows the overlap integral between M3 and LP to be non-zero and the enhanced DFG extraction due to the triple-resonance condition leads to the appearance of the second peak at $\hbar\omega_3 = 1.25$ eV in Fig. 3.3.

Additionally, oblique incidence of the pump beams can be used to tune the DFG energy. As

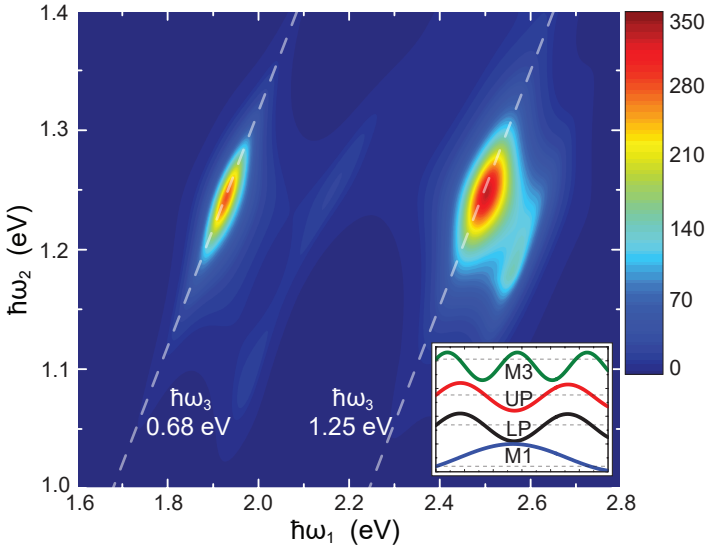

Figure 3.3 DFG irradiance enhancement of the poled NLO polymer model structure with respect to a bare film of equal thickness. Due to the thickness of the second mirror, only reflected fields are considered. The tilted dashed lines correspond to pairs of pump energies that generate the same DFG energy and that match the M1 (left, $\hbar\omega_3 = \hbar\omega_{M1} = 0.68$ eV) and LP (right, $\hbar\omega_3 = \hbar\omega_{LP} = 1.25$ eV) energies in the triple-resonance condition. Inset: normalized electric field profiles of the relevant modes, illustrating the excellent modal overlap of the LP and UP branches.

indicated by Eq. (3.17b), the k_z^{3+} component of the DFG signal rapidly becomes evanescent and therefore we shall consider only the k_z^{3-} component. Figure 3.4 shows the dependence of DFG energy and irradiance on the angle of incidence when $\theta_1 = \theta_2 = \theta_i$. In the lower panel, as the interacting modes move to higher energies, the triple-resonance condition at the Rabi ($E_{UP} - E_{LP}$) energy is maintained for incidence angles up to 79^o. The maximum irradiance is obtained at 57^o for $\hbar\omega_{NL} = 0.72$ eV ($\lambda_{NL} = 1.72$ μm). This enhancement is reduced by 3 dB at $\hbar\omega_3 = 0.74$ eV ($\lambda_3 = 1.68$ μm) for 79^o. The upper panel shows that the peak at $\hbar\omega_3 = 1.25$ eV falls out of the triple resonance condition faster with a 3 dB roll-off at 40^o.

3.4 DFG in a (111) GaAs cavity

The vast majority of resonant nonlinearities observed in inorganic semiconductor microcavities are due to a $\chi^{(3)}$ nonlinearity inherited from the exciton [95]. In the typical $\chi^{(3)}$ four-wave mixing process, two pump (p) polaritons interact to produce signal (s) and idler (i) components such that their wavevectors satisfy $2\mathbf{k}_p = \mathbf{k}_s + \mathbf{k}_i$. Second-order susceptibilities tend to be much larger than their $\chi^{(3)}$ counterparts, but conventionally used (001)-microcavities only

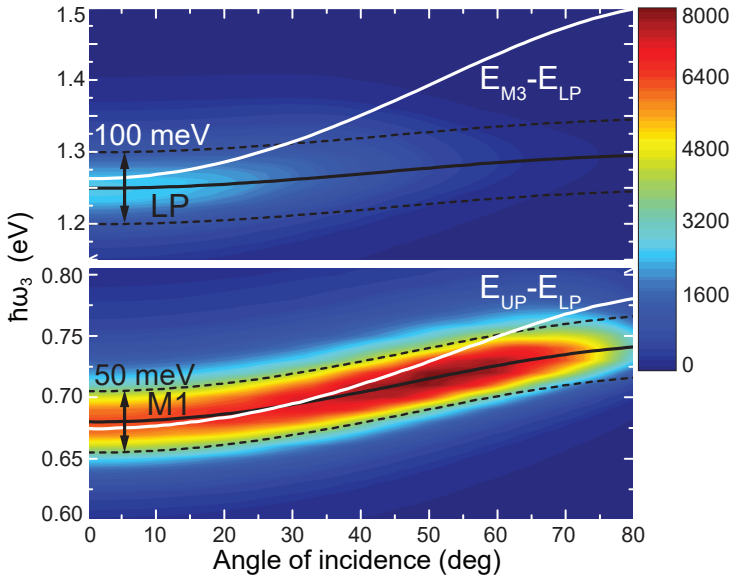

Figure 3.4 Angle dependence of DFG energy and irradiance (kW/m^2) for TE polarized pumps incident on the structure with NLO polymer and Ag mirrors when $\theta_1 = \theta_2 = \theta_i$. Only waves with $k_z^{3-} = k_z^1 - k_z^2$ are considered. Lower and upper panels show the DFG at the the Rabi and LP energies, respectively. Solid black lines illustrate the energies of the M1 (bottom) and LP (top) modes where DFG radiation can be extracted in triple-resonance. Dashed black lines illustrate a typical linewidth of 100 meV for the LP branch and 50 meV for the M1 mode. Solid white lines indicate the angle dependence of the DFG energy. For the upper panel, as the white line moves out of resonance with the black LP line, the DFG peak is suppressed. For the lower one, a slight increase is observed around 57^o and corresponds to an enhancement of the triple-resonance condition, after which the irradiance rolls off.

allow for nonlinear optical mixing between three orthogonally polarized field components.

A number of commonly used inorganic semiconductors are known to be non-centrosymmetric and to possess high second-order susceptibility tensor elements. Examples include III-V semiconductors, such as gallium arsenide (GaAs) and gallium phosphide (GaP), and II-VI semiconductors, such as cadmium sulfide (CdS) and cadmium selenide (CdSe) [30, 96]. To allow for the nonlinear optical mixing of co-polarized waves to occur, we will consider (111) GaAs as the microcavity material [97, 98], in contrast to the typical (001)-oriented material.

We consider a $\lambda/2$ (111) bulk GaAs microcavity sandwiched between 20 (25) pairs of AlAs/ $Al_{0.2}Ga_{0.8}As$ distributed Bragg reflectors on top (bottom). The structure is followed by a bulk GaAs substrate with the same dielectric constant as the cavity material, modeled by Eq. (3.18) with experimental values $\epsilon_b = 12.53$, $f = 1.325 \cdot 10^{-3}$, $\hbar\omega_0 = 1.515$ eV and $\hbar\Gamma =$ 0.1 meV [99]. Experimental values are also used for the refractive index of $Al_xGa_{1-x}As$ [100].

The nonlinear susceptibility was kept the same as for the NLO polymer ($\chi^{(2)} = 300$ pm/V) to allow for a direct comparison of the irradiances. The absolute value chosen has no effect on the enhancement factor. In practice, the largest contribution to the background $\chi^{(2)}$ in GaAs is due to interband transitions and for simplicity we ignore the resonant contribution to $\chi^{(2)}$.

The enhancement in DFG irradiance as compared to a bare GaAs slab of equal thickness is shown in Fig. 3.5. Due to the much smaller oscillator strength in GaAs, as compared to the NLO polymer, the Rabi splitting of $\hbar\omega_3 = 5.52$ meV falls in the THz range ($\nu_3 = 1.33$ THz) with an enhancement of $8.8 \cdot 10^3$.

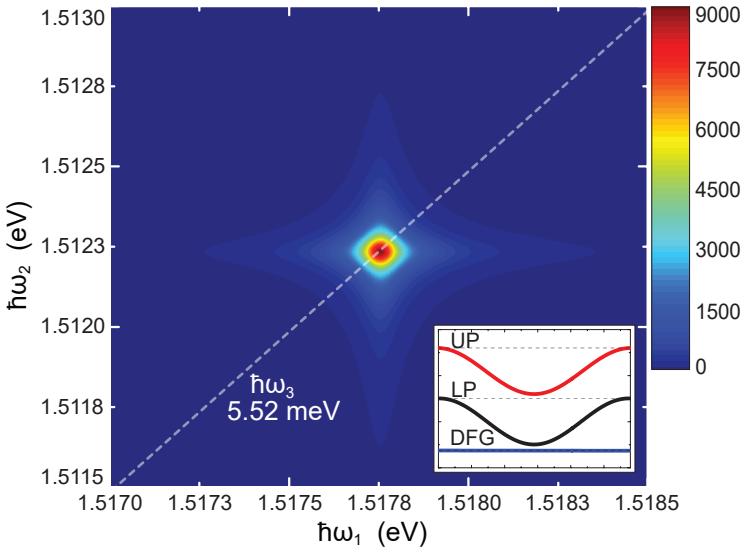

Figure 3.5 DFG enhancement of a $\lambda/2$ (111) GaAs cavity structure with respect to a bare slab. GaAs parameters: $\epsilon_B = 12.53$, $f = 1.325 \cdot 10^{-3}$, $\hbar\omega_0 = 1.515$ eV and $\hbar\Gamma = 0.1$ meV [99]. The same value of $\chi^{(2)} = 300$ pm/V was used as for the NLO polymer. Due to the presence of the substrate, only reflected fields are considered. The tilted dashed line corresponds to pairs of pump energies that generate the same DFG energy. Inset: normalized electric field profiles inside the GaAs layer illustrating the excellent modal overlap of the LP and UP branches.

Figure 3.6 shows the angle dependence of the DFG energy and irradiance when $\theta_1 = \theta_2 = \theta_i$. The dashed black line in the upper panel traces the DFG energy, where a logarithmic scale for the irradiance was used due to its rapid decrease with angle of incidence. The lower panel shows a segment of the same data on a linear scale. Tunability down to 3 dB can be obtained up to $\hbar\omega_3 = 7.21$ meV ($\nu_3 = 1.74$ THz) at 17^o.

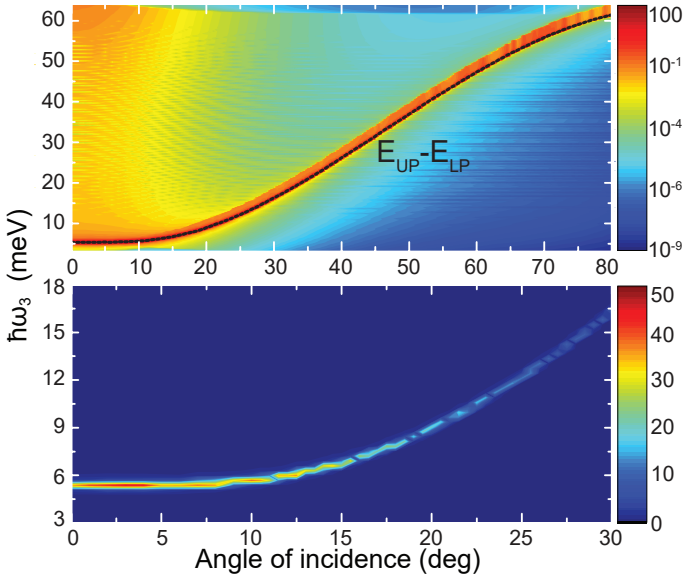

Figure 3.6 Angle dependence of DFG energy and irradiance (W/m^2) for TE polarized pumps incident on the $\lambda/2$ (111) GaAs structure with DBR mirrors when $\theta_1 = \theta_2 = \theta_i$. Only waves with $k_z^{3-} = k_z^1 - k_z^2$ are considered. The upper panel shows the angle dependence of DFG irradiance in logarithmic scale, with the dashed black line tracing the DFG energy. The lower panel shows a smaller angular range of the same data in linear scale where a fast decrease of DFG irradiance can be observed as the angle of incidence increases.

3.5 Discussion

In Sections 3.3 and 3.4 we showed that the use of polaritonic modes for Rabi frequency generation can lead to irradiance enhancements of almost four orders or magnitude with respect to bare nonlinear slabs. Quantitative estimates can be obtained by considering equal pump irradiances $I_1 = I_2 = 10$ GW/m^2. Figure 3.7 shows the maximum DFG irradiances for the two structures and the reference slabs. For the NLO film with Ag mirrors, the calculated peak DFG irradiances are $I_{DFG} = 7.69$ kW/m^2 at $\hbar\omega_3 = 0.68$ eV and $I_{DFG} = 4.05$ kW/m^2 at $\hbar\omega_3 = 1.25$ eV. As expected, due to the higher modal overlap, the DFG irradiance at the Rabi energy exceeds the one at the LP energy. For the $\lambda/2$ (111) GaAs microcavity with DBRs, we find $I_{DFG} = 45$ W/m^2 at $\hbar\omega_3 = 5.52$ meV.

These results can be compared to the ones obtainable with conventional nonlinear crystals. Assuming perfect phase-matching and neglecting pump depletion or losses, the conversion

efficiency CE can be expressed as

$$CE = \frac{I_3}{I_1 I_2} = \frac{2\left[\omega_3 \chi^{(2)} L\right]^2}{n(\omega_1) n(\omega_2) n(\omega_3) \epsilon_0 c^3}, \tag{3.19}$$

where $I_{1,2,3}$ are the irradiances and L is the crystal length [30]. Comparing the organic microcavity to a beta barium borate crystal (BBO, $\chi^{(2)} = 4.4$ pm/V) [30] for near-infrared generation, the required crystal length to achieve the same DFG irradiance is $L = 45$ μm, a factor of 150 larger than the microcavity thickness or $150^2 = 2.25 \cdot 10^4$ lower in conversion efficiency. Similarly, the GaAs microcavity can be compared to a zinc telluride crystal (ZnTe, $\chi^{(2)} = 137$ pm/V) for terahertz generation [101]. In this case, the required crystal length is $L = 36$ μm, a factor of 310 larger than the microcavity thickness or $9.6 \cdot 10^4$ lower in conversion efficiency. In this context, the main advantages of the thinner microcavity layers are the absence of phase matching requirements and the potential for electrical injection.

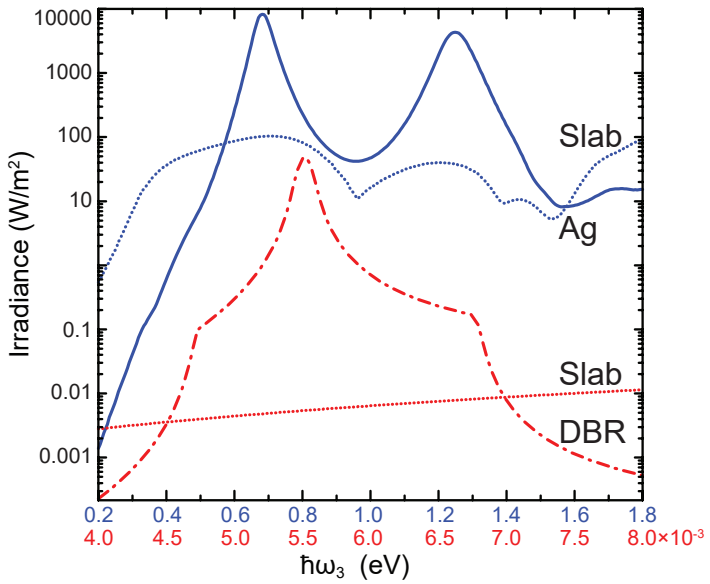

Figure 3.7 Comparison of the calculated DFG irradiances for the two structures studied. Solid blue (dash-dot red) line represents the NLO polymer (GaAs) cavity with Ag (DBR) mirrors and dotted lines directly below represent the corresponding bare slabs. Top blue (bottom red) energy scale relates to the NLO polymer (GaAs) cavity. The curves have been extracted from the maps shown in Fig. 3.3 and Fig. 3.5 by picking out the maximum values among all pairs of pump energies that generate the same DFG energy. Pump irradiances are $I_1 = I_2 = 10$ GW/m^2.

The CE enhancements are a result of the larger $\chi^{(2)}$ used in the calculations (68 times that of BBO and 2.2 that of ZnTe) and, most importantly, of the cavity electric field enhancements,

where a substantial difference was found for both material sets. Metal losses in the polymer cavity prevent a significant enhancement of the UP and LP electric fields with $|E_{peak}/E_{in}| = 1.2$, where E_{peak} and E_{in} are the peak and incident fields, respectively. In contrast, for the GaAs microcavity an enhancement of 15 is obtained. Despite this field enhancement, the irradiance shown in Fig. 3.7 is 170 times lower at the Rabi energy for the inorganic microcavity than for the organic one. This is a consequence of the ω_{NL}^2 factor in the source field given by Eq. (3.8), making DFG at smaller energies increasingly difficult.

Finally, we can use Fig. 3.7 to evaluate the tunability of the structures at normal incidence. For the first structure, the FWHM of the $\hbar\omega_3 = 0.68$ eV DFG peak is 0.045 eV, indicating that the same structure can be used for DFG generation from 1.76 μm to 1.88 μm by adjustment of the pumps only. For the GaAs structure, the FWHM of the $\hbar\omega_3 = 5.52$ meV DFG peak is 0.12 meV, indicating a tunability from $\nu_3 = 1.32$ THz to $\nu_3 = 1.35$ THz.

We should note that although in our calculation two pumps were used, similar enhancements are anticipated for (spontaneous) parametric fluorescence ($I_2 = 0$). In addition, the triply-resonant scheme introduced for the organic microcavity where the signal is resonant has further consequences. First, coupled-mode theory analysis of triply-resonant systems has shown the existence of critical input powers to maximize nonlinear conversion efficiency [76, 102]. These are found to be inversely proportional to the product of the Q-factors. Lower Q-factors are thus advantageous for high power applications, although thermal damage and saturation will limit the operating powers in organic and inorganic microcavities, respectively. Second, the scheme is also well-suited for realizing a more conventional $\chi^{(2)}$ polariton OPO. In this case, the oscillation threshold can be shown to depend inversely on the product of Q-factors.

Since in general, any $\chi^{(2)}$ medium will also have a non-zero $\chi^{(3)}$, these structures will display a change in refractive index proportional to the square of the applied electric field, an effect known as self/cross-phase modulation. The power dependance of the refractive index can lead to rich dynamics such as multistability and limit-cycle solutions [103, 104].

3.6 Conclusion

We studied the potential of microcavities possessing a non-vanishing second-order susceptibility for generating Rabi-frequency radiation. Using a semiclassical model based on nonlinear transfer matrices in the undepleted pump regime, we calculated the Rabi splitting and the DFG irradiance enhancement for an organic microcavity, composed of a poled nonlinear optical polymer, and for an inorganic one, composed of GaAs. In the first case, we obtained a

Rabi splitting of $\hbar\omega_3 = 0.68$ eV ($\lambda_3 = 1.82$ μm) and an enhancement of two orders of magnitude, as compared to a bare polymer film. In the second case, we found a Rabi splitting of $\hbar\omega_3 = 5.52$ meV ($\nu_3 = 1.33$ THz) and an enhancement of almost four orders of magnitude, as compared to a bare GaAs slab. These results show the potential of the use of polaritonic modes for IR and THz generation. Both model structures display a high degree of frequency tunability by changing the wavelength and angle of incidence of the incoming pump beams. Similar enhancements are anticipated for parametric fluorescence and the triply-resonant scheme introduced for the optical microcavity can be exploited to realize monolithic $\chi^{(2)}$ OPOs.

CHAPTER 4 TUNABLE THIRD-HARMONIC GENERATION FROM POLARITONS IN THE ULTRASTRONG COUPLING REGIME

4.1 Introduction

As discussed in Section 2.4, most of the nonlinear phenomena observed using polaritons have been restricted to inorganic microcavities at low-temperatures [6, 7, 43]. There, the intrinsic nonlinearity responsible for pairwise scattering, similar to an optical $\chi^{(3)}$, is strong due to the delocalized nature of Wannier-Mott excitons. The large binding energy of organic Frenkel excitons can in principle allow for such phenomena to be observed at room-temperature, but the exciton-exciton nonlinearities inherent to Frenkel excitons tend to be much weaker than in inorganics. To date, only a handful of nonlinear processes have been observed using organic polaritons [12, 21, 50, 51, 91, 92].

In the limit where the exciton-photon coupling is increased to a significant fraction of the uncoupled exciton energy ($\hbar\Omega_R \sim E_X$), the system enters the so-called ultrastrong coupling regime. As seen in Section 2.3.2, the presence of non-negligible anti-resonant light-matter coupling terms leads to modifications of both excited and ground state properties, a subject which is currently under intense investigation [32, 33, 105]. Demonstrations of USC in organic microcavities [27, 37, 68] have triggered many interesting studies about its effects on observable material properties [40, 41, 106], with many open questions remaining.

In this chapter, we demonstrate organic microcavities operating in the USC regime with a Rabi splitting corresponding to a record 62% of the uncoupled exciton energy. We impart a strong third-order nonlinearity to the resulting polaritons by using a nonlinear polymethine dye as the cavity material and show that the large magnitude of the third-order susceptibility $\chi^{(3)}$ contributes to enhancing polariton interactions.

The enhanced polariton-polariton nonlinearity is used to demonstrate tunable third-harmonic generation spanning the entire visible spectrum upon resonant excitation of the LP mode.

When compared to bare films, the fabricated microcavities show conversion efficiency enhancements of over two orders of magnitude and even larger internal enhancements. Two advantages of polariton states in the USC regime are that they are characterized by narrow, homogeneously broadened lineshapes and a nearly angle-independent dispersion relation [27]. This allows us to obtain high quality factors over a broad spectral range and achieve efficient frequency conversion using focused excitation from a high numerical aperture microscope objective. This structure may also form a versatile platform for the study of other nonlinear phenomena in the USC regime.

4.2 Fabrication and characterization

The microcavities are composed of a film of a bis(selenopyrylium)-terminated heptamethine dye (see Fig. 4.1). Dyes of this type exhibit extremely large magnitudes of the molecular third-order polarizability in solution [107]. The dye used in this study is one of many developed in which bulky substituents on both the chalcogenopyrylium end groups and on the polymethine chain, along with a large counterion, are used to disrupt intermolecular interactions such that the solution linear and nonlinear properties are largely preserved in high chromophore-density films [108]. To characterize the linear optical properties of the polymethine dye, neat films were prepared by spin-coating from 5-20 mg/ml dichloromethane solutions. The refractive index obtained using ellipsometry is shown in Fig. 4.1. The imaginary component shows a strong exciton absorption maximum at 1067 nm ($E_X = 1.162$ eV) and a vibronic shoulder. Note in particular the low losses in the near-infrared part of the spectrum.

Planar microcavities were fabricated by embedding a neat (pure) polymethine layer between silver mirrors. To improve the wetting and optical properties of the back mirror, cleaned quartz substrates were first functionalized with a monolayer of (3-mercaptopropyl)-trimethoxysilane [109]. Then, a 75 nm-thick silver mirror was grown by thermal evaporation at a base pressure of $\sim 10^{-7}$ mBar. After spin-coating the polymethine film, the structure was capped with a 35 nm top mirror. All of the measurements were performed under ambient conditions.

4.3 Angle-resolved reflectivity

Figure 4.2 (a) shows the measured angle-resolved TM-polarized reflectivity from a 350 nm thick microcavity, which corresponds to nearly zero detuning between the exciton and photon energies at normal incidence. The dashed lines correspond to a least-squares fit to the full Hopfield Hamiltonian shown in Eq. (2.63), yielding a Rabi splitting of $\hbar\Omega_R = 0.707$ eV. A

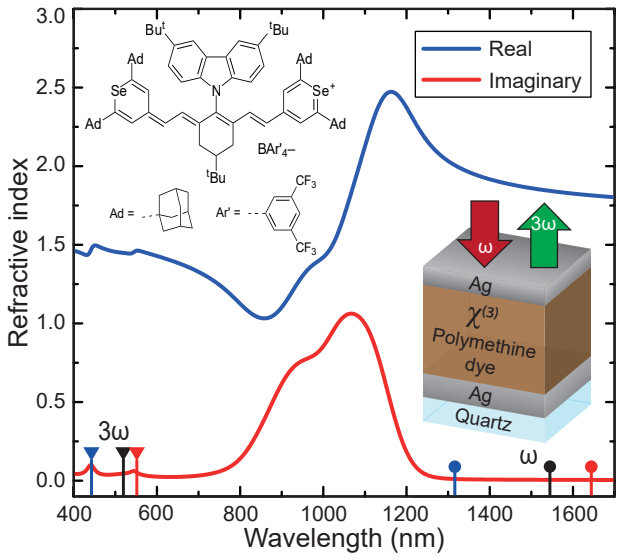

Figure 4.1 Real (blue) and imaginary (red) refractive index of neat polymethine. The imaginary part has a peak value of 1.06 at 1067 nm. Round (triangular) markers indicate the pump (THG) wavelengths where power dependence measurements were performed. The inset shows (top) the chemical structure of the polymethine dye and counterion and (bottom) a schematic of the THG experiment, where a microscope objective is used to focus the pump beam onto the microcavity and to collect the third-harmonic signal from the excitation side.

slightly larger value of $\hbar\Omega_R = 0.719$ eV is obtained for the TE-polarized reflectivity spectrum (not shown).

The remaining fit parameters are summarized in Table 4.1. Note that the different effective refractive indices obtained for TE and TM polarizations are not a consequence of anisotropy in the organic film, but of the polarization-dependent penetration depth of the electric field into the metallic mirrors [27].

Table 4.1 Full Hopfield Hamiltonian fit parameters obtained for the reflectivity data of a 350 nm cavity.

Polarization	$\hbar\Omega_R$ (eV)	n	E_C (eV)
TE	0.719 ± 0.004	1.57 ± 0.04	1.09 ± 0.01
TM	0.707 ± 0.002	1.83 ± 0.04	1.10 ± 0.01

The values obtained for the Rabi splitting correspond to 60-62% of the uncoupled exciton energy, slightly exceeding the largest normalized coupling ratio ($\hbar\Omega_R/E_X$) reported to date of 60% in organic microcavities [37]. The large ratio observed is a consequence of the high

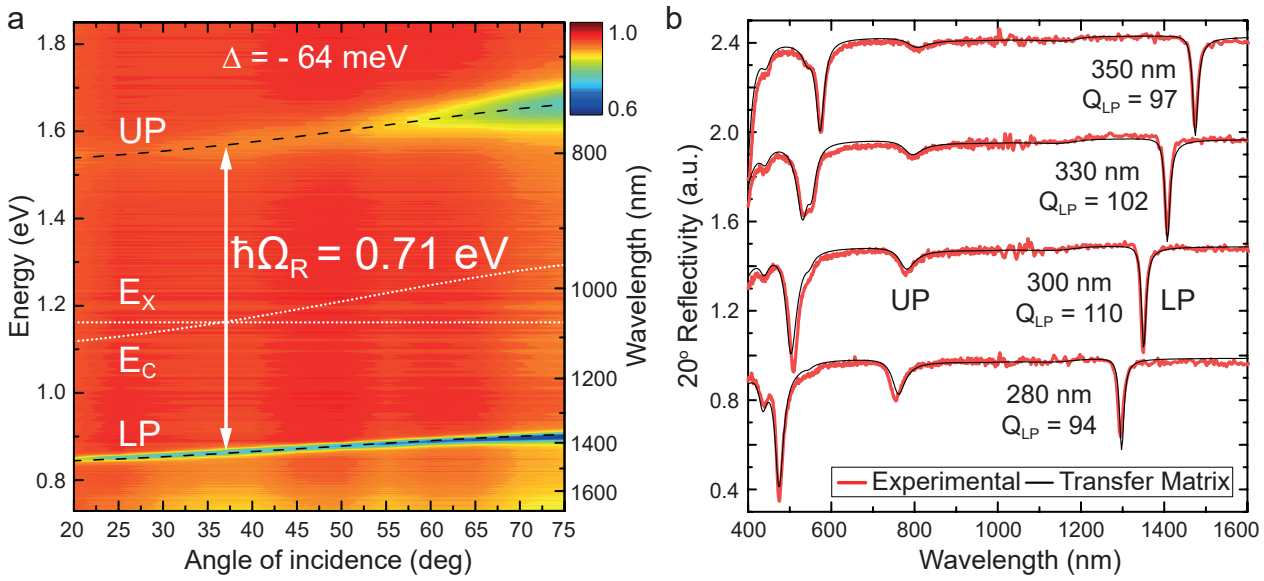

Figure 4.2 (a) Angle-dependent TM-polarized reflectivity spectrum of a 350 nm-thick microcavity. The dashed lines show the least-squares fit to the full Hopfield Hamiltonian, yielding a Rabi splitting of $\hbar\Omega_R = 0.707$ eV and a cavity energy at normal incidence of $E_C = 1.098$ eV. The detuning is $\Delta = E_C - E_X = -64$ meV. (b) Measured (red) and calculated (black) TM-polarized 20^o reflectivity spectra for regions of different thickness present on the same sample, as well as the experimental LP quality factors. The dip below 600 nm is the UP that originates from coupling to the second-order cavity mode.

oscillator strength (f) of the dye and the large number density of molecules (N) resulting from the use of a neat film, both evidenced by the strong absorption band shown in Fig. 4.1. From a simple Lorentz oscillator fit to the real part of the refractive index in the transparency region, we obtain $Nf = 5.59 \times 10^{20}$ cm^{-3} for this material. In addition, the use of metallic mirrors instead of dielectric ones leads to a reduced photonic mode volume. These two factors contribute to the increased $\hbar\Omega_R$. Meanwhile, the near-infrared transition energy leads to a smaller E_X than in previous reports. Note that for larger cavity thicknesses, the coupling ratio can exceed 90% in this structure.

We find that the experimental LP quality factors can exceed 100, which is considerably higher than typical values (below 30) obtained for all-metal microcavities [68, 110, 111]. This is a consequence of the material's low linear losses and the high reflectivity of silver in the near-infrared part of the spectrum. This is helpful for increasing the efficiency of nonlinear processes or, in some cases, lowering their thresholds [75, 95]. Despite the inhomogeneously broadened absorption of the dye, the LP reflectivity spectra showed Lorentzian lineshapes characteristic of homogeneous broadening, a consequence of the large Rabi splitting compared

to the inhomogeneous linewidth [112].

The LP resonance position can be readily tuned via changes in angle of incidence or sample thickness. Our use of high concentration solutions and of a high vapor pressure solvent naturally leads to smooth thickness gradients over the sample surface. This allows for multiple cavity thicknesses to be probed using a single sample. These can be easily identified experimentally due to changes in the surface color caused by the changing position of the UP branch. Figure 4.2b shows a collection of measured (red) and calculated (black) TM-polarized 20^o reflectivity spectra taken at different locations. The corresponding sample thicknesses are indicated below the traces.

4.4 Third-harmonic generation

Figure 4.3a shows a calculated reflectivity map, where the spectral positions of the polariton modes are obtained for increasing values of cavity thickness.

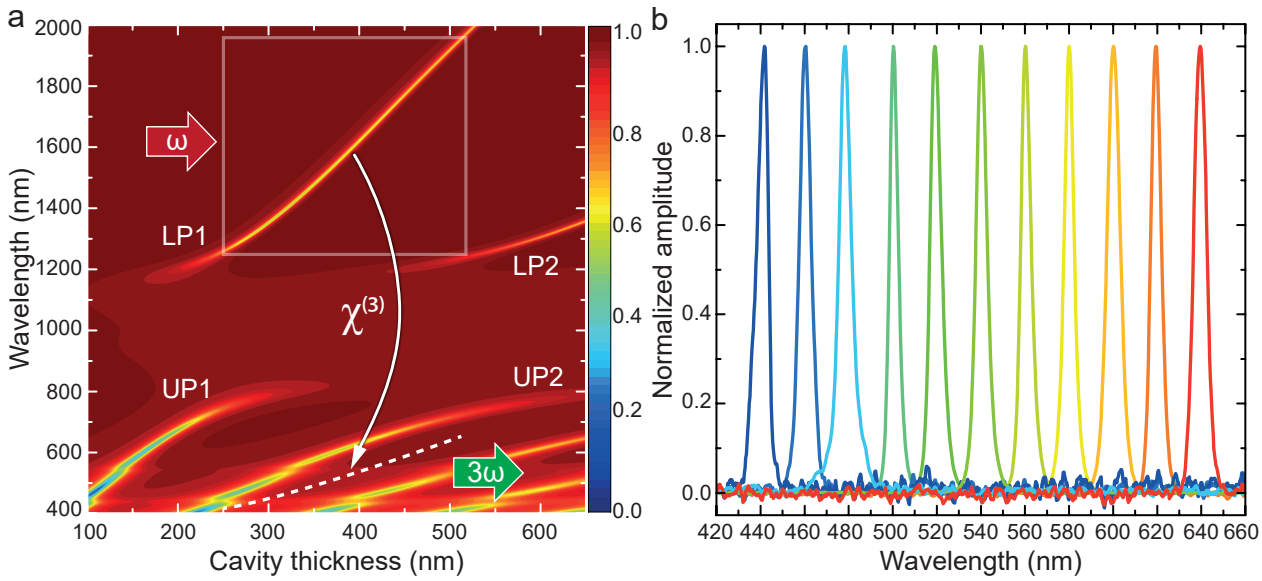

Figure 4.3 (a) Calculated microcavity reflectivity spectra at normal incidence for increasing values of polymethine thickness. The four polaritonic modes indicated by LP1/UP1 and LP2/UP2 arise due to the strong coupling of the exciton transition to the first- and second-order cavity modes, respectively. The top box indicates the range of LP spectral positions covered by the broad infrared pump (1250-1950 nm). The corresponding third-harmonic wavelengths are indicated by a dashed line. (b) Experimental normalized THG spectra obtained on areas of different cavity thickness found on the same microcavity sample.

The first four polaritonic modes indicated by LP1/UP1 and LP2/UP2 correspond to strong

coupling to the first- and second-order cavity modes, respectively. The broad pump is spectrally filtered by the thickness-dependent LP resonance position, as shown in the top box in Fig. 4.3a. The resonant component is coupled into the microcavity and interacts with the high $\chi^{(3)}$ material to generate the third-harmonic signal. The THG wavelengths corresponding to the first LP branch are shown as a dashed line in the bottom of Fig. 4.3a.

Third-harmonic generation was first studied by exciting the sample with a broad IR pump spanning 1250-1950 nm. The experimental setup is detailed in Appendix A.2. Figure 4.3b shows a series of normalized THG spectra obtained on areas of different cavity thickness found on the same microcavity sample and illustrates the tunability of the THG process at normal incidence. Note that the third-harmonic is not resonant with higher order modes and only light that can leak out due to the finite transmission of the mirrors is observed. Nevertheless, the generated harmonic signals were easily visible with the naked eye through the microscope optics.

To investigate the THG power dependence as a function of wavelength, the broad IR pump was spectrally filtered using 12 nm bandpass filters, which is slightly narrower than the mean LP linewidth of 14 nm obtained from Fig. 4.2b. The measurement calibration is detailed in Appendix B. The pump and corresponding THG wavelengths are indicated in Fig. 4.1 by round and triangular markers, respectively. Figure 4.4 shows the results obtained for the fabricated microcavities (curves 1-3). We observe a doubling of the conversion efficiency when changing from 1320 nm to 1650 nm excitation. This corresponds to an increased THG efficiency for polaritonic modes that are more photonic in nature, as highlighted in Fig. 4.5. When pumping at 1320 nm, which corresponds to modes with a strong exciton component, we observed a fast irreversible decay of the THG signal due to sample damage — a clear signature of the mode matter content. Note, in contrast, that the linear absorption of the bare film is negligible at this wavelength. For longer wavelengths, no decrease in THG powers was observed for up to an hour of measurement.

The values at the end of each curve correspond to the peak power conversion efficiencies, defined as $P_{3\omega}/P_{\omega}$. In all cases, the THG wavelength was not resonant with the higher order upper polariton modes and was not efficiently extracted from the microcavity. Nonetheless, the experimental conversion efficiencies for the microcavities were comparable to those of other systems that required patterning or considerably thicker films [113–115].

For comparison, THG from bare polymethine films of different thicknesses are shown in Fig. 4.4 (curves 4-5). The 368 nm-thick film (curve 5) is of comparable thickness to the microcavities and allows for an accurate estimate of the conversion enhancements. Table 4.2 shows the fit coefficients C obtained by fitting each data set with a cubic power dependence of

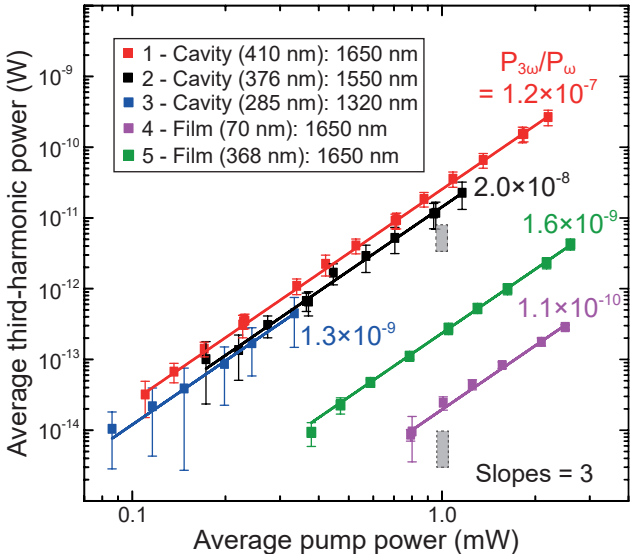

Figure 4.4 Measured third-harmonic powers (squares) as a function of pump power. Red, black and blue data sets correspond to microcavities pumped at 1650 nm, 1550 nm and 1320 nm, respectively. Bare polymethine films of 70 nm and 368 nm were investigated at 1650 nm and the results are shown in purple and green, respectively. The solid lines indicate a cubic power fit to each data set. The values at the end of each curve correspond to their peak conversion efficiencies, defined as $P_{3\omega}/P_{\omega}$. The top (bottom) gray boxes indicate the range of calculated THG powers on the excitation side for the microcavity (bare films) shown in Fig. 4.5.

the form $P_{3\omega} = C \times {P_{\omega}}^3$. The last column shows the conversion enhancements with respect to the 368 nm-thick film. At the wavelength of highest conversion efficiency (1650 nm), the fabricated microcavities show raw (external) THG enhancement factors of 108 ± 1.7 compared to the bare film. As shown in Fig. 4.5, the internal efficiency at this wavelength is approximately 50 times higher than this value due to the low fraction of THG that is out-coupled from the cavity.

4.5 Simulations

To correlate our results with the LP exciton and photon fractions at normal incidence, Fig. 4.5 shows the polariton modal content calculated using the full Hopfield Hamiltonian from experimental (circles) and simulated (squares) angle-resolved reflectivity spectra. Note that in the USC regime, the contribution from the squared electromagnetic vector potential leads to a blueshift of the bare cavity photon energy and that the modal content of both components is no longer equal at zero detuning, which corresponds to 1432 nm in Fig. 4.5 [32]. We find

Table 4.2 Experimental cubic fit coefficients for data sets 1-5 shown in Fig. 4.4 and the THG conversion enhancement with respect to the 368 nm-thick bare film.

Data Set	C	THG Enhancement
1	$(254.2 \pm 2.1) \times 10^{-4}$	108.0 ± 1.7
2	$(142.9 \pm 2.7) \times 10^{-4}$	60.7 ± 1.4
3	$(119.7 \pm 2.7) \times 10^{-4}$	50.6 ± 1.3
4	$(195.8 \pm 7.4) \times 10^{-7}$	–
5	$(235.4 \pm 3.2) \times 10^{-6}$	–

that the LP branch varies from 73% to 52% exciton content over the range of thicknesses used in Fig. 4.4 (indicated by colored arrows).

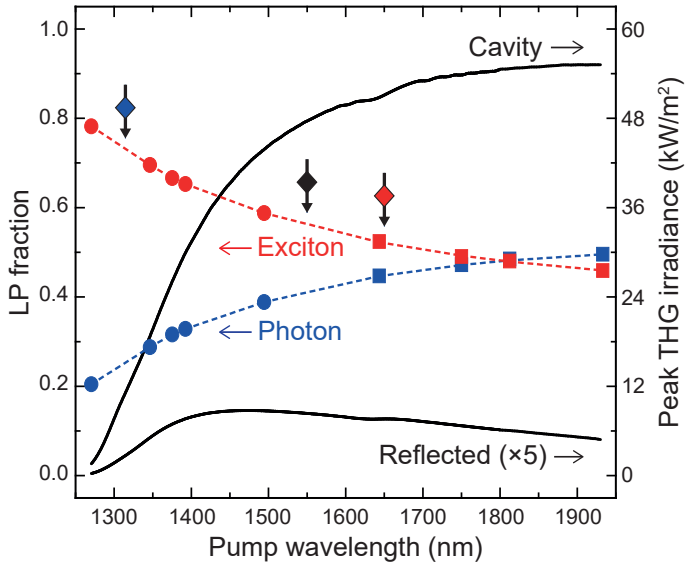

Figure 4.5 Calculated exciton (red) and photon (blue) fractions for the first LP branch from experimental (circles) and simulated (squares) reflectivity data. The solid black curves show the calculated THG irradiances inside the cavity (top) and outside on the excitation side (bottom). The colored arrows in indicate the experimental conditions for the measurements in Fig. 4.4.

To determine the origin of the enhancement, THG was investigated using the same nonlinear transfer matrix approach introduced in Chapter 3. In this way, the combined effects of multiple reflections and absorption at both the fundamental and third-harmonic wavelengths are automatically taken into account, as well as the resonant pump enhancement and non-resonant THG extraction factors. Maintaining the same notation, we consider only one pump with frequency ω_1 such that the third-harmonic frequency is given by $\omega_4 \equiv 3\omega_1$. Then, the

nonlinear polarization vectors given in Eq. (3.11) are replaced by

$$\mathbf{P}^{4-} = \frac{3}{4}\epsilon_0\chi^{(3)}\begin{bmatrix} E_1^+E_1^+E_1^- \\ E_1^+E_1^-E_1^- \end{bmatrix} \tag{4.1a}$$

$$\mathbf{P}^{4+} = \frac{1}{4}\epsilon_0\chi^{(3)}\begin{bmatrix} E_1^+E_1^+E_1^+ \\ E_1^-E_1^-E_1^- \end{bmatrix}, \tag{4.1b}$$

and the perpendicular component of k^{NL} takes the values of $k_z^{4-} = k_z^1$ or $k_z^{4+} = 3k_z^1$. The average power radiated towards the excitation side of the microcavity is given by

$$P_{4R} = \frac{1}{2}\epsilon_0 c\,|E_{R4}|^2\,\frac{1}{8}\left(\frac{\pi}{\log 2}\right)^{\frac{3}{2}} \cdot f \cdot \tau_t \cdot \tau_r^2, \tag{4.2}$$

assuming that the THG has both a temporal and spatial Gaussian profile. Here E_{R4} is the calculated electric field in reflection, $f = 40$ MHz is the laser repetition rate, $\tau_t = 48$ ps is the pump pulse length and $\tau_r = 1.5$ μm is the THG spot waist. Figure 4.6a shows a map of the calculated THG powers for the fabricated microcavities as a function of cavity thickness and pump wavelength for an average input power of 1 mW. As expected, the THG map resembles the reflectivity map shown in the boxed region of Fig. 4.3a because THG is only generated when the pump is resonant with the LP branch. The colored arrows indicate the experimental conditions of cavity/film thickness and pump wavelength for the measurements in Fig. 4.4. The top gray box in Fig. 4.4 shows the range of calculated THG powers emitted towards the excitation side for the microcavities. The quantitative agreement with the experimental values is remarkable, considering that the only parameter not known with certainty is the third-order susceptibility $\chi^{(3)}(3\omega;\omega,\omega,\omega)$, which was kept dispersionless and equal to the value $\chi^{(3)}(\omega;-\omega,\omega,\omega) = -5.1\times10^{-11}$ esu (-7.12×10^{-19} m^2/V^2) measured using the z-scan technique [108].

A similar calculation for the bare films pumped at 1650 nm is shown in Fig. 4.6b and was found to be less accurate for the 368 nm-thick film, with the experimental value closer to the transmitted THG power (not shown) instead of the one measured on the excitation side. The bottom gray box in Fig. 4.4 shows the range of calculated THG powers for the bare films. We believe that the discrepancy stems from the large angular spread of wavevectors in the focused pump beam, which is not taken into account in our calculations. For microcavities, wavevectors away from the resonance condition are naturally filtered out by the LP dispersion. The agreement for the thinner film and microcavities confirms that the value of $\chi^{(3)}$ used in

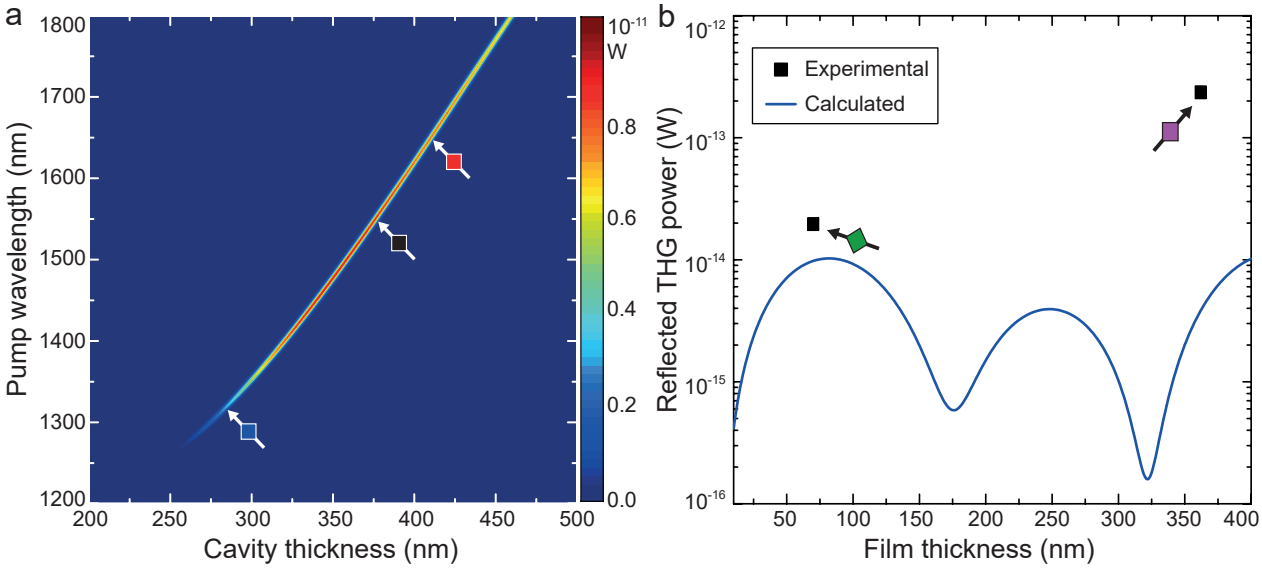

Figure 4.6 (a) Calculated THG power radiated towards the excitation side for a microcavity pumped at 1650 nm for an average input power of 1 mW. THG is obtained when the pump is resonant with the LP mode, maintaining the same shape as in the boxed region in Fig. 4.3. (b) Same calculation for a thin film on quartz. The colored arrows in a,b indicate the experimental conditions for the measurements in Fig. 4.4.

the calculations is a reasonable estimate for the real one. Therefore, even when neglecting possible resonant enhancements of $\chi^{(3)}$ due to the weak absorption bands in the visible part of the spectrum, the observed enhancements in THG from polaritons are consistent with the cavity enhancement of the pump electric field and the bulk third-order nonlinearity, as opposed to a drastic modification of the material's nonlinear properties [66]. At the same time, in the equivalent polaritonic picture, the THG enhancement stems from the three resonantly pumped polaritons with increased nonlinear interactions. Still, compared to bare films, microcavities offer the advantage that they require smaller thicknesses to generate the same harmonic power. This is a consequence of the pump electric field enhancement, the reduced absorption of the generated signal and the absence of a phase-matching requirement, with the conversion efficiency depending instead on mode overlap, which can be tuned by microcavity design or by the use of polaritonic modes [19, 76].

Fig. 4.5 also shows the calculated peak THG irradiances inside the cavity as compared to the THG emitted on the excitation side. Both curves significantly decrease towards shorter wavelengths because of the absorption band peaked at 1067 nm. The internal THG first increases towards longer wavelengths as losses in the mirrors are reduced for thicker cavities. The decreasing transmission of the front silver mirror towards longer wavelengths eventually

leads to a decrease in both the internal and external components, the latter already visible in Fig. 4.5. For this range of wavelengths, the internal THG enhancements are up to 56 times higher than the ones observed from the excitation side. Further calculations show that small modifications of the structure to improve out-coupling, such as reducing the top mirror thickness or achieving a doubly-resonant condition of the THG wavelength with an UP branch can further increase the THG efficiency by more than an order of magnitude.

4.6 Conclusion

In this chapter, we have reported organic microcavities containing a nonlinear dye operating in the USC regime and possessing a normalized coupling ratio of 62%, slightly exceeding the highest value ever reported [37]. The combination of the material's low losses and the use of high reflectivity silver mirrors led to LP quality factors much higher than conventional all-metal microcavities. The polariton nonlinearity was exploited to demonstrate efficient and tunable third-harmonic generation when the cavity was excited resonantly with the LP branch. Although the THG was not resonantly extracted from the microcavities, conversion enhancement factors of up to two orders of magnitude were obtained in comparison to bare films. Transfer matrix calculations indicate that the observed enhancement can be explained by the pump field enhancement alone, suggesting that the material's third-order susceptibility is not strongly modified even in the case of ultrastrong light-matter coupling. This demonstration of nonlinear polariton microcavities operating in the USC regime can allow for the observation of room-temperature nonlinear effects so far restricted to low-temperature inorganic systems, in addition to to new phenomena unique to the USC regime.

CHAPTER 5 NUMERICAL STUDY OF SUPERFLUIDITY IN A POLARITON CONDENSATE

5.1 Introduction

In atomic systems, the transition from a classical gas into a macroscopic quantum state is typically achieved by keeping the number of particles fixed and lowering the temperature below a critical value T_C. Condensation into the ground state then occurs in the regime where the interparticle distance is comparable to the thermal de Broglie wavelength [116] given by

$$\lambda_T = \sqrt{\frac{2\pi\hbar^2}{Mk_BT}}. \tag{5.1}$$

We see that the temperature T and the particle mass M play a similar role in determining the condensation threshold. Exciton-polaritons are excellent candidates to enable Bose-Einstein condensation above cryogenic temperatures because their effective masses can be up to 10 orders of magnitude lower than those of atoms. For instance, this would bring the condensation threshold temperature for a gas of ^{87}Ru atoms, which is of the order of 200 nK [117], easily to room temperature.

Polariton condensation is usually observed at a constant and less stringent temperature condition as the density of particles is increased beyond a critical value. Despite the lighter effective masses, polariton condensation was initially only observed at cryogenic temperatures due to the low exciton binding energies of inorganic quantum well excitons [48]. Today, however, as shown in Section 2.4.3, polariton BEC and lasing have been already demonstrated at room temperature in a variety of systems, not only in organic microcavities [12, 42, 50, 51, 118] but also in inorganic perovskite and nitride ones [13, 53–55, 119, 120] where $E_B > k_BT$.

Recently, our collaborators in the group of Dr. Daniele Sanvitto at the CNR Nanotec Institute reported the first conclusive demonstration of superfluid behavior in a polariton condensate at room temperature [21]. The regime where superfluid behavior was observed is very different from the one common for atomic condensates. Due to the short polariton lifetime of the cavity, the system is not in thermal equilibrium, but rather in a dynamic one where polaritons are constantly being injected by the pump beam and escaping the cavity. In addition, since the pump pulse duration is comparable to the polariton lifetime, complicated temporal dynamics take place and are not accessible in time-averaged measurements.

In this chapter, we will introduce the main experimental results from our collaborators and present our time-resolved simulations of the Gross-Pitaevskii equation, introduced in Section 2.4.1. Using their experimental parameters, our simulations were able to reproduce the observed superfluid behavior and shed light on the dynamics of the system.

5.2 Sample and experimental setup

The cavity consists of a 130 nm thick film of the organic molecule 2,7-Bis[9,9-di(4-methyl-phenyl)-fluoren-2-yl]-9,9-di(4-methyl-phenyl)fluorene, which was sandwiched between a pair of reflectance DBR mirrors. The sample is mounted on a rotation stage and positioned between two microscope objectives. The LP branch is resonantly excited with TE-polarized ultrashort 33 fs laser pulses. Since such short pulses are broadband, resonance excitation can be maintained for different angles of incidence and in the presence of a LP blueshift. This allows polaritons with specific group velocities v_g to be resonantly excited via tuning of the pump energy E_p and angle of incidence θ according to

$$v_g = \frac{\hbar k_p}{m_{LP}} = \frac{\hbar \omega_p}{m_{LP}c} \sin(\theta) = \frac{E_p}{m_{LP}c} \sin(\theta). \tag{5.2}$$

Both the light reflected and transmitted by the cavity are collected by the objectives and used for momentum- and real-space imaging, respectively. All measurements were performed under ambient conditions.

5.3 Experimental results

A polariton wavepacket traveling with a group velocity of 19 μm/ps is created by the resonant pump and propagates along the plane of the sample. This is shown in Fig. 5.1a in the low excitation regime. When the upward flow of polaritons encounters an obstacle, such as an imperfection in the organic film, a shadow region of low polariton density is seen behind

the object. In addition, as a consequence of interference between incident and reflected waves, density modulations can be seen in front of the obstacle. The spacing between these fringes is inversely proportional to the speed at which polaritons propagate. Figure 5.1b shows the corresponding momentum space image in the linear regime. In addition to the saturated pump, injected at $k_p = 3.59\ \hat{y}\ \mu\text{m}^{-1}$, a resonant Rayleigh scattering ring is seen, corresponding to elastic scattering of polaritons by the obstacle.

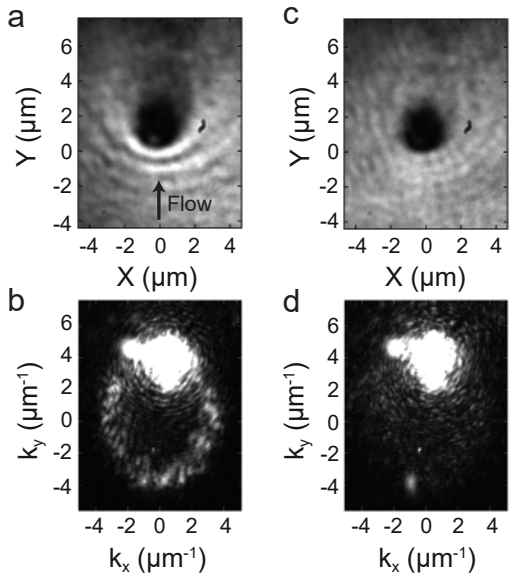

Figure 5.1 (a) Experimental real-space polariton distributions in the linear and (c) nonlinear regimes illustrating the transition from dissipative to superfluid flow. The Gaussian pump, with FWHM=13 μm is centered 2 μm below the defect position. The peak polariton densities are $0.5 \cdot 10^6$ pol/μm^2 in (a) and 10^7 pol/μm^2 in (c). (b) Experimental saturated momentum-space maps corresponding to the linear and (d) nonlinear regimes.

When the peak pump intensity was increased above a certain threshold, our collaborators observed that the interference fringes ahead of the obstacle disappeared and the fluid uniformly filled the space around the defect. This is shown in Fig. 5.1c. Experimentally, the fringes don't disappear completely because of time integration during image acquisition, which also records intervals where the polariton density is below the critical value. In momentum space, superfluid behavior manifests itself as a collapse of the Rayleigh ring towards the pump excitation spot, in agreement with the experimental results shown in Fig. 5.1d.

5.4 Simulations

By solving the time-dependent GP equation, we can calculate the polariton evolution using parameters corresponding to the experimental conditions. We begin by modifying Eq. (2.82) to include a potential barrier $V(r)$ to represent the position of the obstacle and obtain

$$i\hbar\frac{\partial\Psi(r,t)}{\delta t} = \left(\hbar\omega_0 - \frac{\hbar^2\nabla^2}{2m_{LP}} + V(r) - \frac{i\gamma_{LP}}{2} + g_{LP}|\Psi(r,t)|^2\right)\Psi(r,t) + \hbar P(r,t). \tag{5.3}$$

For simplicity, the defect is taken to be an infinite barrier with vanishing boundary conditions. The pump term $P(r,t)$ is taken to be a plane wave modulated by a temporal Gaussian envelope

$$P(r,t) = F_p e^{i(kr-\omega_p t)} e^{-\frac{(t-t_0)^2}{2\sigma_t^2}}, \tag{5.4}$$

where σ_t can be related to the intensity FWHM using $\sigma_t = FWHM/(2\sqrt{ln2})$. The amplitude of the driving term can be related to the incident pump intensity using input-output theory [45] as

$$F_p = |C_{k_p}|\sqrt{\frac{\gamma_{LP} I_0}{2\hbar\omega_p}}, \tag{5.5}$$

where $|C_{k_p}| = 0.88$ is the Hopfield coefficient for the photon fraction of the LP mode at the pump wavevector k_p. The remaining simulation parameters are $\hbar\omega_0 = 2.896$ eV, $m_{LP} = 1.976 \cdot 10^{-35}$ kg, $\gamma_{LP} = 10^{13}$ s^{-1}, $g_{LP} = 5 \cdot 10^{-3}$ μeV $\cdot$ μm^2, $k_p = 3.59\ \hat{y}$ μm^{-1} and $\hbar\omega_p = 2.9242$ eV.

First, we will examine the case when the pump pulse is not broadened by the optical elements, then the effect of a positive chirp will be considered. To compare our simulations with the experimental time-integrated images, the calculated polariton density maps ($|\Psi(r,t)|^2$) were integrated over a time interval of 800 fs. Instantaneous momentum-space maps were obtained via a Fourier transform and then time-averaged.

5.4.1 Ultrashort pump

Time-averaged

Our simulation results in real-space for the linear and superfluid regimes are shown in Fig. 5.2a and c, respectively. We could extract peak polariton density values of $1.6 \cdot 10^5$ pol/μm^2 and $2.4 \cdot 10^7$ pol/μm^2 for the linear and the superfluid regimes, which are in agreement with the estimated experimental values of $0.5 \cdot 10^6$ pol/μm^2 and 10^7 pol/μm^2, respectively. The momentum-space profiles below and above the superfluidity threshold are shown in Fig. 5.2b

and d, respectively. The overall agreement with the experimental results shown in Fig. 5.1 is excellent.

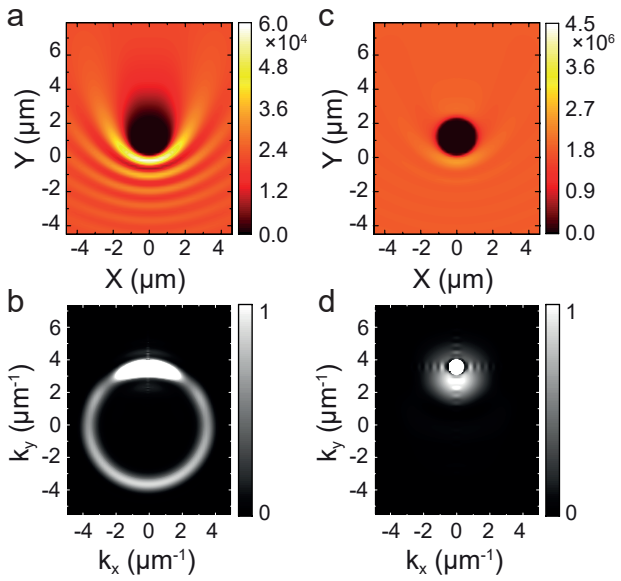

Figure 5.2 (a) Calculated real-space polariton distributions in the linear and (b) nonlinear regimes. The peak polariton densities are $1.6 \cdot 10^5$ pol/μm^2 in (a) and $2.4 \cdot 10^7$ pol/μm^2 in (b). (c) Calculated saturated momentum-space maps corresponding to the linear and (d) nonlinear regimes. The simulation parameters are listed in the text.

To make a connection to the pump fluence, we can use $E_{in} = I_0 \sigma_t \sqrt{\pi}$, which gives 26.6 mJ/cm^2 for the incident fluence in the superfluid regime. This is comparable with the experimental value of 4 mJ/cm^2, given the approximations made in connection with input-output theory and the approximate value of the polariton interaction constant. Indeed, the latter is the only experimental parameter not known with certainty. The value chosen for the simulations is close to a previous estimate of $g_{LP} = 10^{-3}$ μeV $\cdot$ μm^2 in this structure [121] and also to that obtained using the resonant blueshift at high powers. At higher powers, however, the measured blueshift of the polariton may be strongly affected by the thermal load of the pump, causing a competing redshift of the polariton energy due to an expansion of the cavity length.

Finally, Fig. 5.3 shows the measured and calculated reduction in elastic scattering obtained from the Rayleigh scattering patterns as a function of the pump fluence. Our simulations were able to reproduce the decreasing trend and the relative suppression observed in the experimental results.

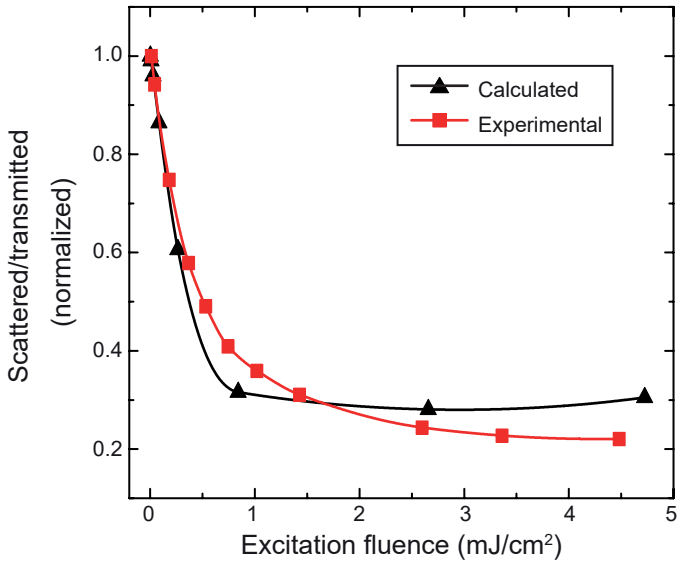

Figure 5.3 Calculated and experimental ratio of the scattered light to transmitted light obtained from the Rayleigh scattering patterns. Note that the precise shape of these curves is sensitive to the choice of k-space mask used to block the transmitted light. In our simulations, a mask of radius 4.8 μm^{-1} centered on k_p was used.

Time-evolution

An advantage of the numerical simulations is that we can observe in detail the dynamics of the polariton wavepacket as it transitions in and out of the superfluid regime. Figure 5.4 shows the time-evolution of the polariton densities measured directly behind the defect and in the background region. For reference, the normalized pump pulse is shown in black.

In the linear regime (Fig. 5.4a), we can observe the reduced polariton density behind the defect and a slow decay of the polariton densities on a timescale given by the polariton lifetime. As the pump density is increased (Fig. 5.4b), we first cross into a regime where the driving rate exceeds dissipation and the field coherently follows that of the pump. Beyond this threshold, we cross into the superfluid regime due to the renormalized dispersion. Here, the density behind the defect follows the background density closely.

Figure 5.5 shows instantaneous snapshots of the calculated polariton densities in the linear and superfluid regimes. When crossing back into dissipative flow at longer times, vortex pairs are created behind the defect and carried away by the viscous flow (Fig. 5.5b at $t = 500$ fs).

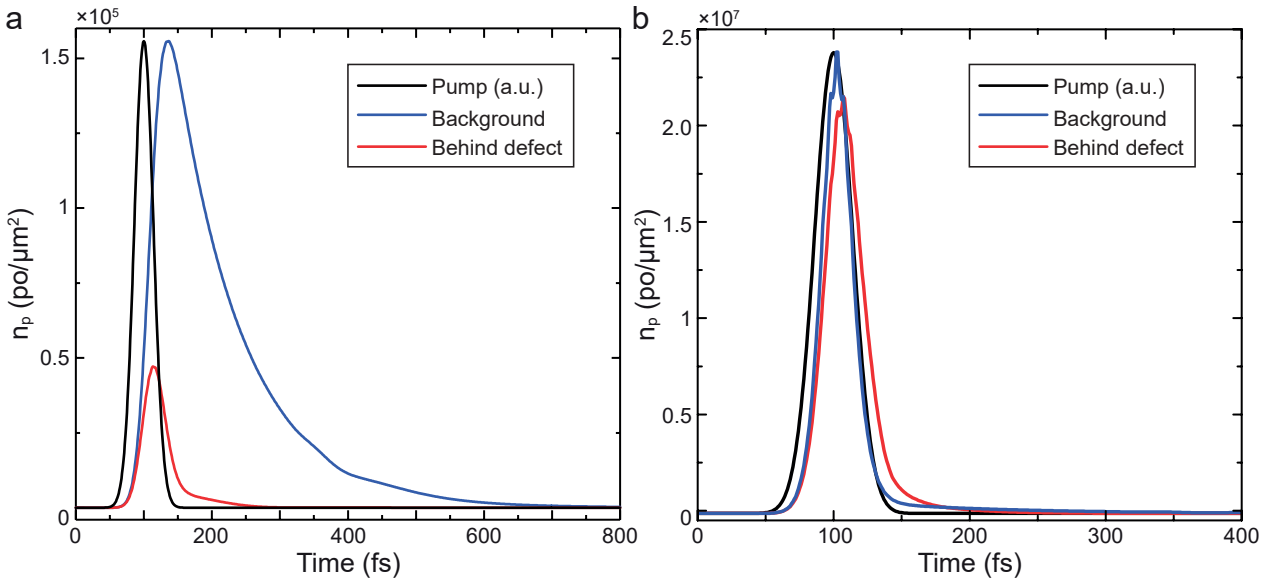

Figure 5.4 Time-domain polariton density traces taken directly behind the defect (red) and in the background (blue) in the (a) linear and (b) superfluid regimes. The pump pulse is traced in black and normalized to the peak background density.

5.4.2 Temporal broadening of the pump pulse

The positive chirp acquired during propagation through optical elements leads to a temporal broadening of the pump pulse and a lowering of its peak amplitude. To investigate the effects of chirp in the simulation results, the equations of the driving term are modified as [122]

$$P(r,k,t) = F_p e^{i(kr-\omega_p t)} e^{-\frac{(t-t_0)^2}{2(\sigma_t^2+i\mathrm{GVD}d)}} \tag{5.6}$$

and

$$F_p = C_{k_p}\sqrt{\frac{\gamma_{LP} I_0}{2\hbar\omega_p}\cdot\frac{\sigma_t^2}{\sigma_t^2+i\mathrm{GVD}d}}, \tag{5.7}$$

where GVD = 90.4 fs^2/mm is the group velocity dispersion coefficient of fused silica at the pump wavelength of 424 nm and d = 30 mm is the total thickness of optical elements in the path of the pulse. The results for the superfluid case are shown in Fig. 5.6 for the same simulation parameters as in Fig. 5.2. The same superfluid behaviour is seen in the time-integrated real and momentum space images (Fig. 5.6a,b), but the time domain traces show a number of relaxation oscillations due to the longer pulse duration (Fig. 5.6c,d). The modulation from these initial oscillations is also larger than in the unchirped case. Finally,

the pump intensity threshold for the observation of superfluid behavior remained unchanged.

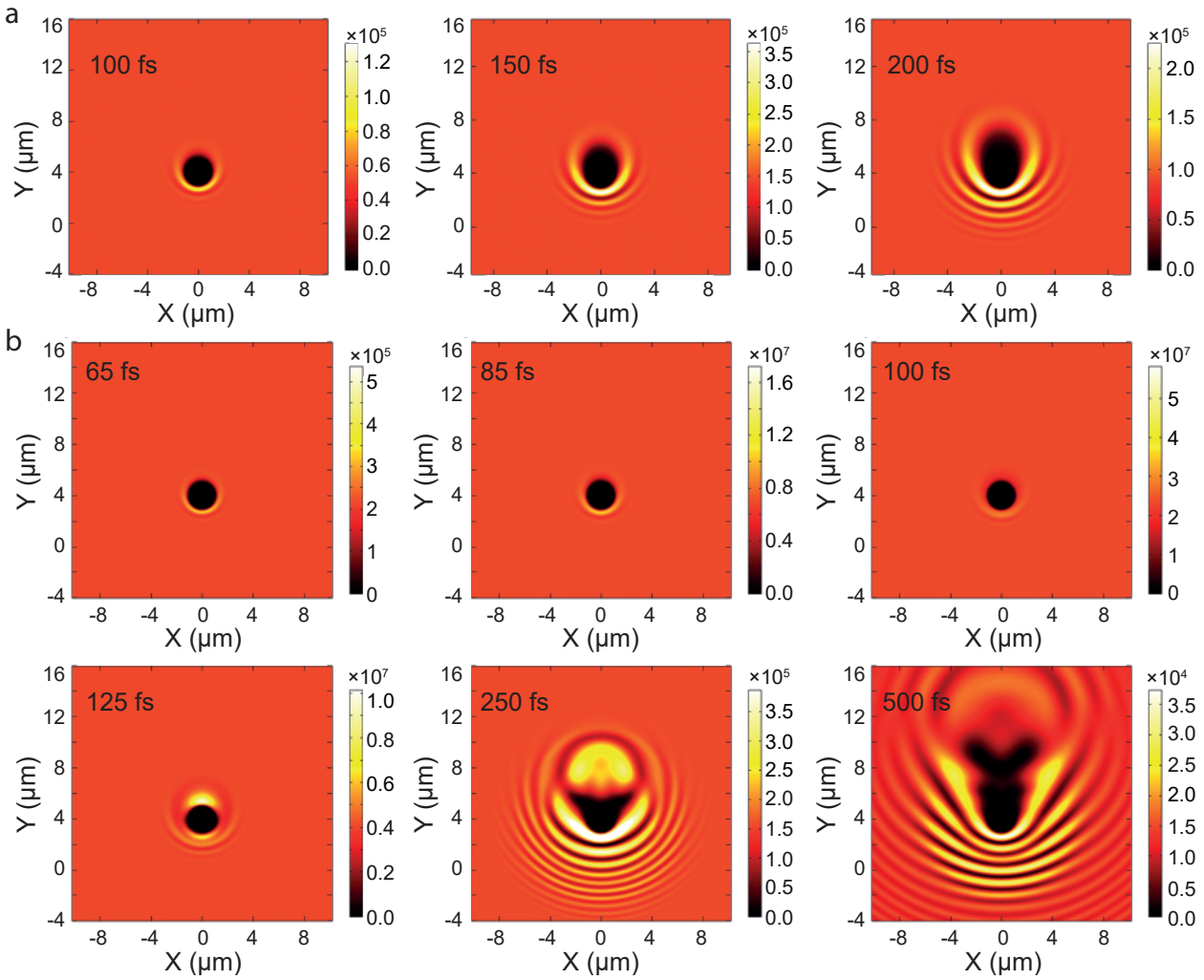

Figure 5.5 (a) Individual time snapshots of the polariton density during polariton flow in the linear and (b) superfluid regimes. Note the ejection of vortex pairs around 500 fs when the density has been reduced. The color scales are in pol/μm^2 and their maximum values are adjusted to maintain the background color throughout the images.

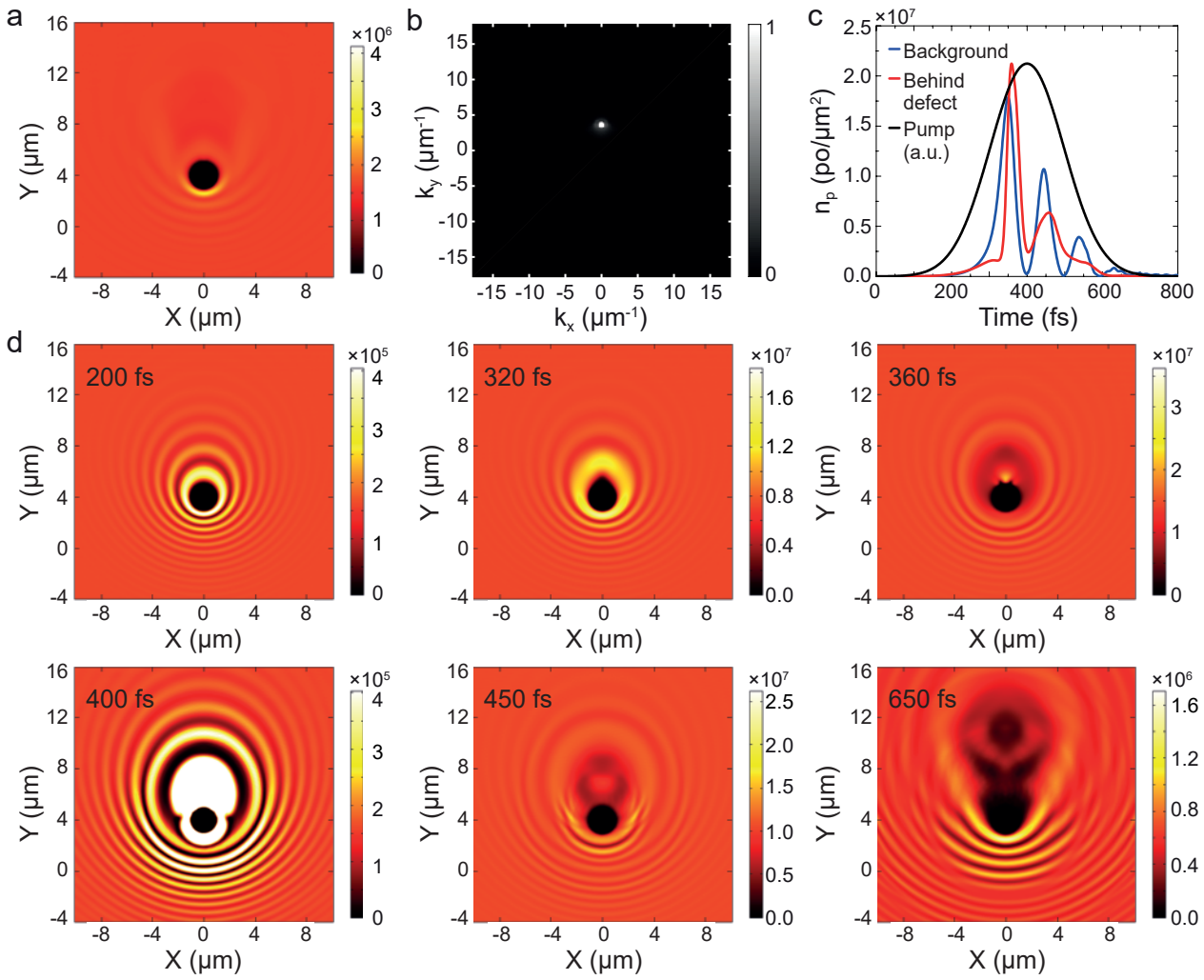

Figure 5.6 (a) Real space polariton density profile in the superfluid regime when the pump is chirped by going through 3 cm of fused silica. Peak background density is $1.8 \cdot 10^7$ pol/μm^2. (b) Saturated intensity momentum space emission profile showing the absence of the Rayleigh scattering ring pattern. (c) Time-domain polariton density traces behind the defect (red) and in the background (blue). The pump pulse is traced in black and normalized to the peak density. (d) Individual time snapshots of the polariton density during polariton flow. The color scales are in pol/μm^2 and their maximum values are adjusted to maintain the background color throughout the images.

5.4.3 Steady state

Steady-state Bogoliubov excitation spectra

The excitation spectra of the stationary solutions can be calculated by linearizing the GP equation around a stationary homogeneous state ψ_{SS} following Ref. [63]. We consider the case of resonant excitation at the renormalized dispersion and that the LP wavefunction has a plane-wave form similar to the pump field given by

$$\psi(r,t) = \psi_{SS} e^{i(k_p r - \omega_p t)}. \tag{5.8}$$

Then, the spectrum of the excitations is given by the solutions of the eigenvalue problem

$$\mathcal{L}_k \mathcal{U}_k = \hbar\omega_k \mathcal{U}_k, \tag{5.9}$$

with the small fluctuations vector given by

$$\mathcal{U}_k = [\delta\psi(r,t), \delta\psi^*(r,t)]^T \tag{5.10}$$

and the operator $\mathcal{L}_k$ being defined as

$$\mathcal{L}_k = \begin{pmatrix} \hbar\omega_{LP}(k) + 2g_{LP}n_p - i\hbar\gamma_{LP}/2 & g_{LP}n_p \\ -g_{LP}n_p & 2\hbar\omega_p - \hbar\omega_{LP}(2k_p - k) - 2g_{LP}n_p - i\hbar\gamma_{LP}/2 \end{pmatrix}. \tag{5.11}$$

Figure 5.7 shows the Bogoliubov excitation energies obtained for polariton density values below (black), at (red) and above (green, blue) the superfluidity threshold. The energies are traced with respect to the center pump energy. Note that for each value of k, the dispersion contains two branches $\omega^{\pm}_{LP}(k)$. Since they are related by symmetry as $\omega^{-}_{LP}(k) = 2\omega_p - \omega^{+}_{LP}(2k_p - k)$, only the positive branch is shown.

At low densities, as in Fig. 5.7 (black), the dispersion remains parabolic and the presence of isoenergetic states available for scattering generates the resonant Rayleigh scattering ring pattern observed in momentum space in Fig. 5.2b. For increasing densities, the polariton-polariton interactions tilt the dispersion and introduce a discontinuity in the slope around k_p. For the threshold density shown in Fig. 5.7 (red), the dispersion becomes horizontal at low momentum values in the vicinity of k_p and point to the collapse of the scattering ring to a single point, as shown in Fig. 5.2d. Above the superfluidity threshold, as in Fig. 5.7 (green, blue), the dispersions show a minimum at k_p and the linear slope defines the sound

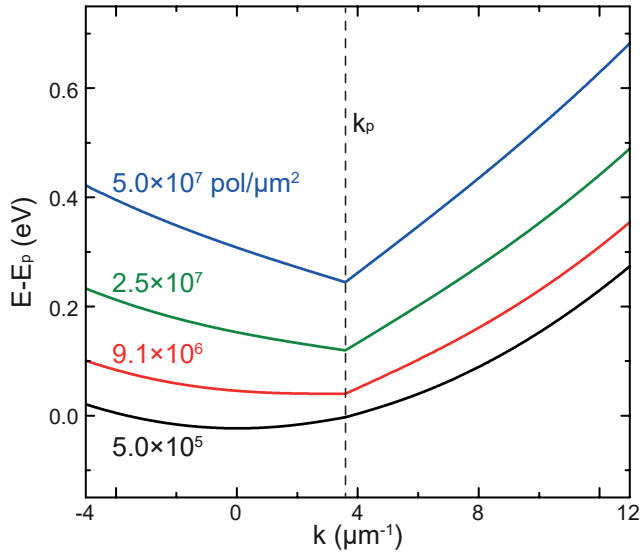

Figure 5.7 Positive Bogoliubov branch as a function of polariton density. At high polariton densities, the linearized dispersion becomes apparent. Note the absence of elastic scattering beyond $9.1 \cdot 10^6$ pol μm^{-2}.

velocity. Although the Bogoliubov analysis is performed for the steady-state, the threshold density for the superfluid transition is in agreement with the experimental densities and the time-dependent calculations.

Simulations

We can verify that the superfluid behavior would also be observed in steady-state under the same experimental conditions. The pump pulse was set to be a long rectangular pulse with duration of 2 ps, having the same peak amplitude as in the short pulse case shown in Fig. 5.2c. As shown in Fig. 5.8, superfluidity persists through the damped oscillations and the linear regime is recovered shortly after the end of the pump pulse. Note that the density modulations disappear from the time-integrated real-space map.

5.5 Conclusion

Using parameters corresponding to the experimental conditions, our GP calculations were able to reproduce the superfluid behaviour observed by our collaborators. We found that despite the small polariton-polariton interaction constant of organic polaritons, the superfluid regime is indeed achieved at a group velocity of 19 μm ps^{-1} when the polariton density reaches approximately 10^7 pol μm^{-2}, in agreement with the experimental estimates. Finally,

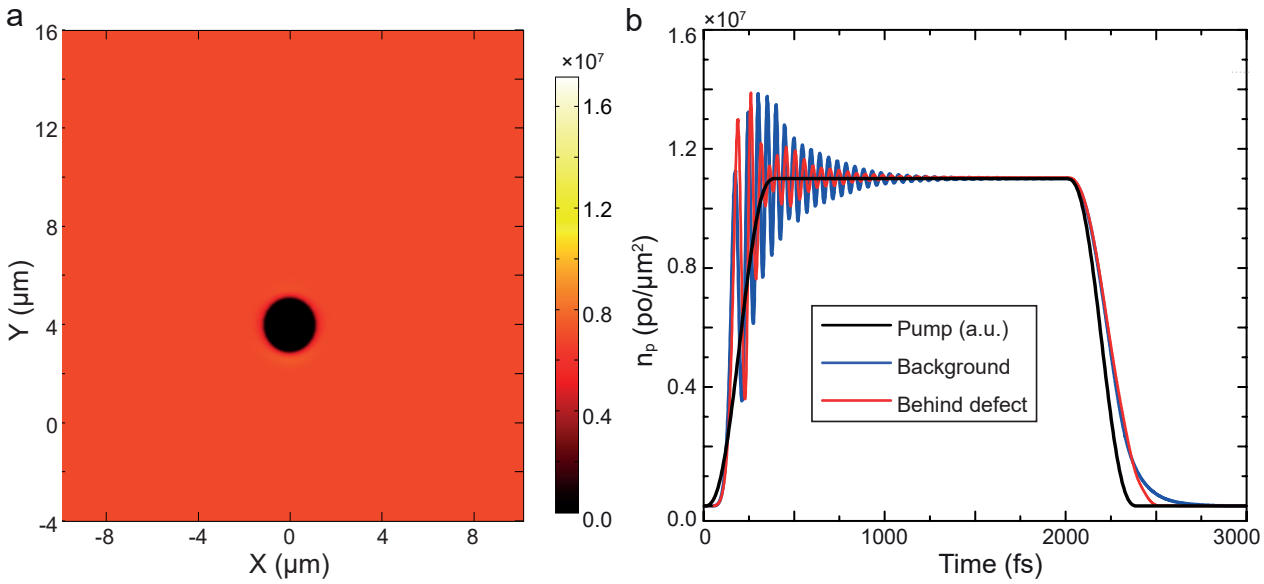

Figure 5.8 (a) Real space polariton density profile in the superfluid regime when the pump is a rectangular pulse of duration 2 ps. The steady-state background density is $1.1 \cdot 10^7$ pol/μm^2. (b) Time-domain polariton density traces behind the defect (red) and in the background (blue). The pump pulse is traced in black and normalized to the steady-state density.

we were able to resolve the presence of relaxation oscillations and the launching of vortex pairs, shedding light on the range of hydrodynamic effects that occur in the quantum fluid. Entering a steady-state regime free of transients would allow for the study of additional effects, such as the formation of free vortices. This, however, has been prevented by the limited photostability of organic semiconductors.

CHAPTER 6 INTERACTING POLARITON FLUIDS IN A MONOLAYER OF TUNGSTEN DISULFIDE

6.1 Introduction

As reviewed in Section 2.4, the light effective masses and strong interparticle interactions of exciton-polaritons have enabled demonstrations of nonlinear effects of tremendous technological interest. Until now, however, the cryogenic temperatures required for commonly used inorganic quantum well microcavities and the weak nonlinearities observed in room-temperature excitonic systems have hampered the use of polaritons for practical applications [7].

A promising new class of materials to overcome these limitations is that of atomically thin transition metal dichalcogenides. The increased carrier confinement and reduced dielectric screening in TMDs lead to the creation of excitons with a large binding energy, which dictate the optoelectronic properties of the material even at room temperature and have been predicted to lead to strong nonlinearities due to enhanced Coulomb interactions [29, 123]. In addition to room temperature excitonic behaviour, TMDs enable an unprecedented electrostatic tunability of their optical properties, the harnessing of higher-lying Rydberg exciton states and access to the valley degree of freedom [124–126].

The direct bandgap and high oscillator strength of monolayer TMDs have allowed strong light-matter coupling to be demonstrated in a variety of systems, including planar microcavities [126–130], plasmonic cavities [130–132], fibre cavities [124] and photonic crystals [133]. At room-temperature, however, these structures have been limited to the linear regime due to short polariton lifetimes resulting from the high losses of the underlying cavity and the broad exciton linewidths.

In this chapter, we overcome these limitations by strongly coupling the A exciton of monolayer WS_2 to a low-loss propagating Bloch surface wave at the air-dielectric interface of a Bragg mirror. The strong coupling shifts the lower polariton mode away from the exciton absorption and into the transparency region of the spectrum. The resulting low losses enable polaritons to propagate over the entire extent of the monolayer. Together, the longer polariton lifetime, stronger electric field enhancement and narrow polariton linewidths allow for the first observation of polariton-polariton nonlinearities in TMD monolayers. To highlight the role of such nonlinearities, we demonstrate a nonlinear polariton source in a configuration analogous to that previously used to show bistability under continuous wave excitation [7]. All measurements reported here were performed under ambient conditions.

6.2 Fabrication and characterization

A schematic of the sample is shown in Fig. 6.1a. A glass coverslip was coated with a dielectric mirror, designed to support a Bloch surface mode near the A exciton band of WS_2 (2.014 eV/615.6 nm) [134]. The Bragg mirror consisted of five pairs of tantalum pentoxide (Ta_2O_5)/silicon dioxide (SiO_2) layers (98.5 nm/134.6 nm thick), deposited by radiofrequency magnetron sputtering at a pressure of 10^{-7} mbar. An additional thinner pair (17.1 nm/22.3 nm) was used to shift the position of the Bloch mode at the WS_2 A exciton wavelength towards the center of the photonic bandgap. A large monolayer of WS_2 was first tape-exfoliated onto a polydimethylsiloxane stamp and subsequently transferred onto the top dielectric surface. Tungsten disulfide was chosen as the active material over other TMDs due to its strong and sharp excitonic absorption, which better matches the narrow linewidths of Bloch surface modes. The solid line in Fig. 6.1a shows the calculated electric field profile corresponding to the bare Bloch mode at the A exciton wavelength. The field peaks inside the last dielectric pair and decays exponentially away from the surface. The mode is TE polarized and propagates along the surface with wavevector $\vec{k}_{BSW}$.

Fig. 6.1b shows a micrograph of the large exfoliated WS_2 flake in reflectance (top) and in photoluminescence (PL, bottom) under 514 nm excitation by a large Gaussian spot. Only the monolayer regions exhibit bright PL due to their direct bandgap [135]. A typical monolayer PL spectrum is shown in Fig. 6.1c and contains a single strong peak centered at 1.988 eV/623.6 nm with a FWHM of 42 meV. These values vary slightly along the sample, presumably due to fluctuations in strain, substrate adhesion, defects and surface charge density [136, 137].

To demonstrate strong coupling between the monolayer A exciton and the BSW, white-light reflectivity was measured with an immersion objective in a back focal plane imaging configuration. The experimental setup is detailed in Appendix A.3. In Fig. 6.2a we show the

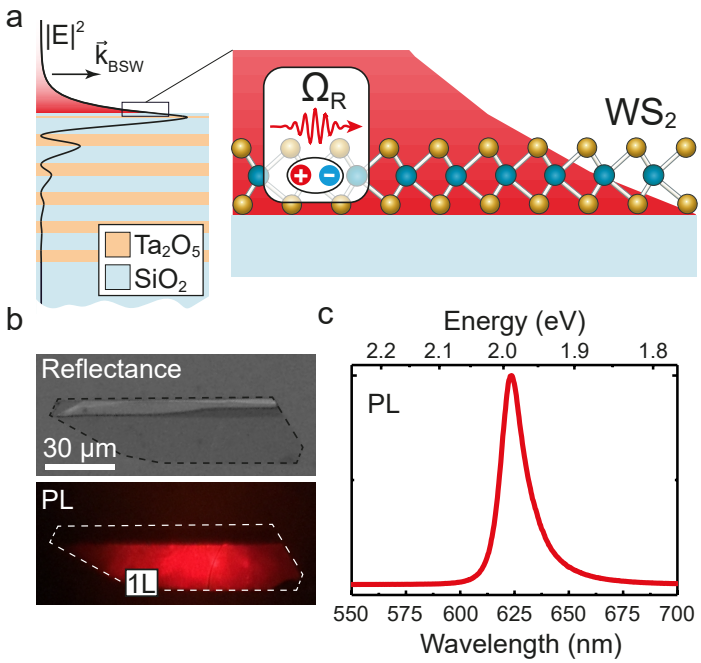

Figure 6.1 (a) Schematic of the dielectric stack supporting Bloch surface wave polaritons in monolayer WS_2. The solid black lines trace the electric field profile of the bare mode at the wavelength of the A exciton band. The mode is TE polarized and propagates along the surface with wavevector $\vec{k}_{BSW}$. The inset illustrates the coupling of the enhanced electric field at the surface of the stack to the in-plane excitons in the monolayer. (b) Micrographs of the monolayer in reflectance and PL. The dashed lines indicate the flake boundaries. Only monolayer regions show bright PL under illumination by a large Gaussian spot. (c) The typical monolayer PL spectrum under 514 nm excitation contained a single strong peak centered at 1.988 eV/623.6 nm.

experimental dispersion of the upper and lower polariton modes measured in the center of the monolayer. The position and visibility of the modes are in good agreement with transfer matrix calculations shown in Fig. 6.2b, where the thickness and refractive index of monolayer WS_2 were obtained from the literature [134].

Both polariton branches are also visible in PL, as shown in Fig. 6.2c on a logarithmic color scale. Their anti-crossing, a signature of the strong-coupling regime, is evident in both reflectance and PL around the same wavelength of 623 nm, coinciding with the peak PL wavelength shown in Fig 6.1c. Interestingly, a progression of modes surrounding the LP branch is visible in Fig. 6.2a,c. Bloch surface waves are extremely sensitive to changes in the thickness and refractive index of the topmost layer. In the case of our monolayer, these can be caused by surface inhomogeneities in the large area probed by the propagating mode. A

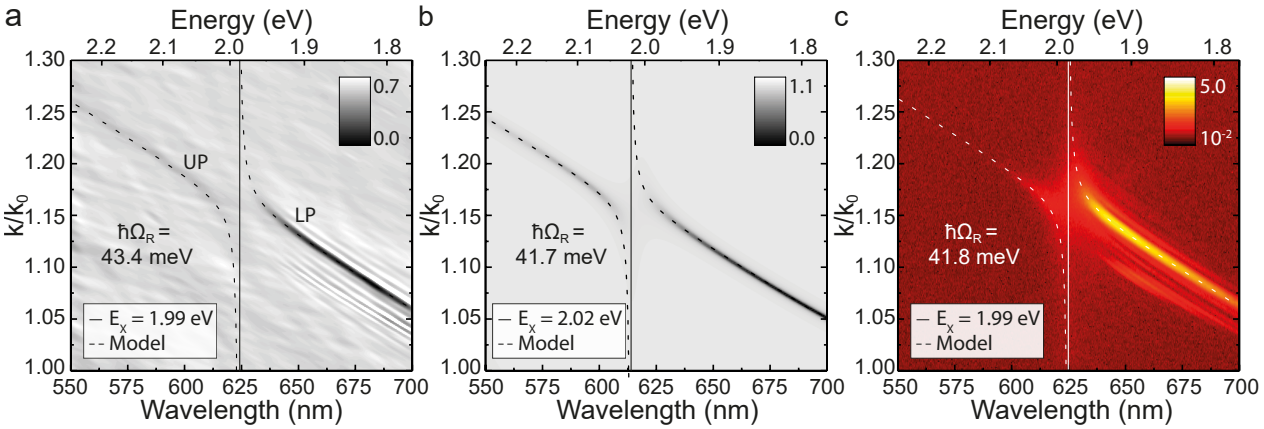

Figure 6.2 (a) Experimental dispersion of Bloch surface wave polaritons (BSWPs) in monolayer WS_2 in reflectance and (b) the corresponding transfer matrix calculation. (c) Experimental dispersion in PL under 514 nm excitation on a logarithmic color scale. Coupled harmonic oscillator fits and fitting parameters are shown in all three panels. The UP and LP modes are traced in dashed lines and the fitted exciton energies are indicated by solid lines.

similar but weaker effect could also be seen for the bare mode (not shown). For each panel in Fig. 6.2, the simple 2×2 coupled harmonic oscillator model shown in Eq. (2.54) was used to fit the data. The energy dispersion of the bare Bloch surface mode in the center of the photonic bandgap was approximated by

$$E_C(k) = \hbar v_g |k| + E_0, \tag{6.1}$$

where v_g is the group velocity and E_0 is a fitting parameter. The dispersion fits and exciton energies are traced in dashed and solid lines, respectively. The extracted Rabi splittings of 43.4±0.8 meV and 41.8±0.6 meV are in close agreement with the transfer matrix value of 41.7± 0.3 meV.

6.3 Polariton propagation

Next, we investigated how far BSWPs are able to propagate within the WS_2 monolayer. The pump wavevector and wavelength were selected to be in resonance with the LP mode. The corresponding real space spot size dimensions were typically 3 μm × 5 μm (FWHM). The first panel in Fig. 6.3a shows the real space propagation trace for an exciton fraction of 10% and wavelength of 645 nm. Propagation can be observed for over 60 μm and ends upon reaching the flake boundary, indicated by a dashed white line. As a comparison, the

propagation of the uncoupled (bare) Bloch surface wave is shown in panel 2. The propagation constants extracted from single exponential decay fits were 20.6±0.1 μm and 21.1±0.1 μm for the LP and bare modes, respectively. These values are considerably larger than the ones found in high-quality planar microcavities embedding TMD monolayers, which are typically of the order of 1 μm [128]. The propagation length can be further increased by limiting the angular content of the excitation beam. By reducing divergence in this way, the propagation length of the bare mode could be increased to 42.2±0.2 μm (not shown). The third panel in Fig. 6.3a shows an enlarged micrograph of the monolayer in reflectance where the monolayer boundaries can be seen.

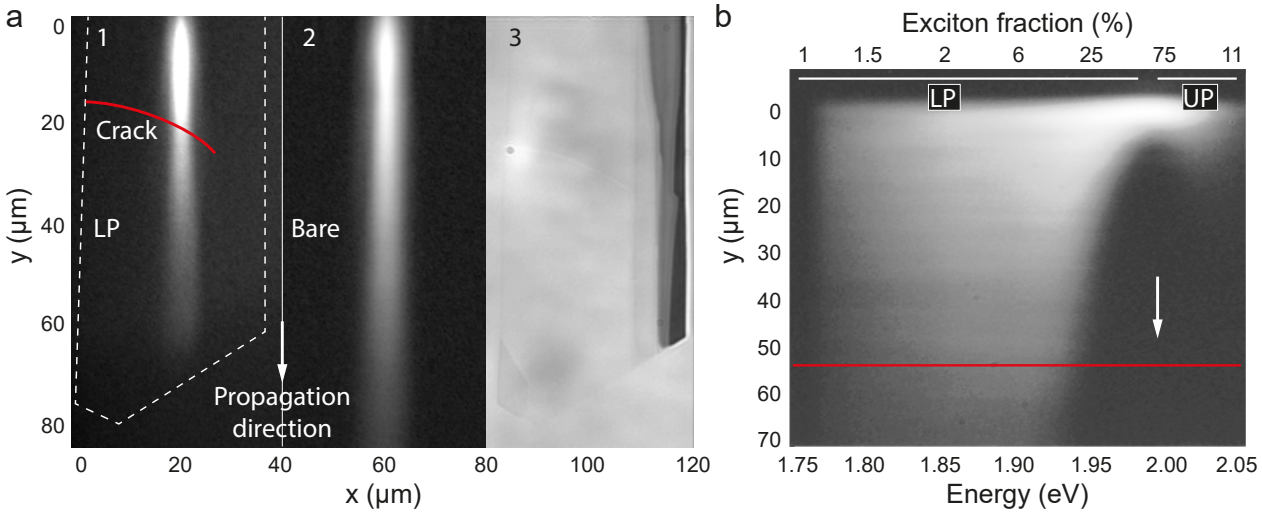

Figure 6.3 (a) Resonant propagation at a wavelength of 645 nm for the LP (exciton fraction of 10%) and bare modes, shown in panels 1 and 2, respectively. Corresponding propagation constants are 20.6±0.1 μm and 21.1±0.1 μm. The flake boundary is shown by a white dashed line. A small crack, indicated by a solid red line in panel 1, has very little impact on the propagation, possibly due to the high photonic content of the mode. Panel 3 shows a micrograph of the monolayer in reflectance where the crack and boundaries can be seen. (b) Non resonant (PL) propagation under 514 nm excitation on a logarithmic intensity scale. The presence of the small crack, which leads to a small change in slope, is indicated by the solid red line. Propagation constants for the LP branch ranged from 14.7±0.1 μm to 33.4±0.4 μm for exciton fractions between 16% to 2%. Polaritons from the upper branch are also visible but propagate significantly less. In both measurements the propagation direction is downwards, as indicated by the white arrows.

Propagation was also investigated using non-resonant above-gap excitation. In this case, the pump first creates excitons, which subsequently relax into propagating polariton states. Fig. 6.3b shows the PL spectrum under 514 nm excitation as it propagates within the flake. As

previously observed in planar microcavities, relaxation kinetics lead to a LP emission intensity that diminishes for states with lower exciton content [126]. The propagation constants for polaritons with exciton fractions ranging from 2% to 16% were found to be between 33.4±0.4 μm and 14.7±0.1 μm, consistent with the resonant case. Weak emission from the UP mode is also visible using the logarithmic intensity scale of Fig. 6.3b . The much shorter propagation distances for the UP are consistent with the increased linear losses above the exciton energy. The experimental LP propagation constant for an exciton fraction of 16% agrees well with the value of 15.3 μm, estimated from the group velocity and a 6.4 meV linewidth (103 fs lifetime).

6.4 Nonlinear interactions

Next, we study the effect of polariton-polariton interactions. At high densities, polaritons interact through their matter component due to phase space filling, which leads to a lowering of the oscillator strength, and due to inter-particle Coulombic interactions, which under most conditions are repulsive and lead to a blueshift of the polariton modes. Fig. 6.4a shows the resonant blueshift of the LP mode at the highest incident pump fluence (60 mJ cm^{-2}) as a function of the resonance position in the linear regime and the exciton fraction extracted from the coupled harmonic oscillator model shown in Fig. 6.2a. In Fig. 6.4b we show the complete power sweep where the highest time-averaged blueshift of 12.9±0.5 meV was observed. The top two curves for low and high fluences show that the blueshift is reversible and is larger than the LP linewidth of 7∼8 meV.

The blueshift saturates with power, as evidenced by a flattening out of the dashed line in Fig. 6.4b at higher fluences. The saturation behaviour is also shown in Fig. 6.5 for different starting energy positions of the LP mode and is more pronounced at higher exciton fractions. This is consistent with the exciton-exciton annihilation mechanism which has been shown to play an important role in TMD monolayers at high exciton densities [138, 139].

6.5 Simulations

Quantifying the strength of the polariton nonlinearity due to exciton-exciton interactions and PSF from the observed LP blueshift requires an accurate knowledge of the polariton density. In addition, when several modes in momentum space are excited, their individual contributions must be accounted for [34]. Using input-output theory and parameters corresponding to our experimental conditions, we calculated the LP field in momentum space such that $|\psi(k,t)|^2$ is the instantaneous number of polaritons in the mode k. Its time-evolution

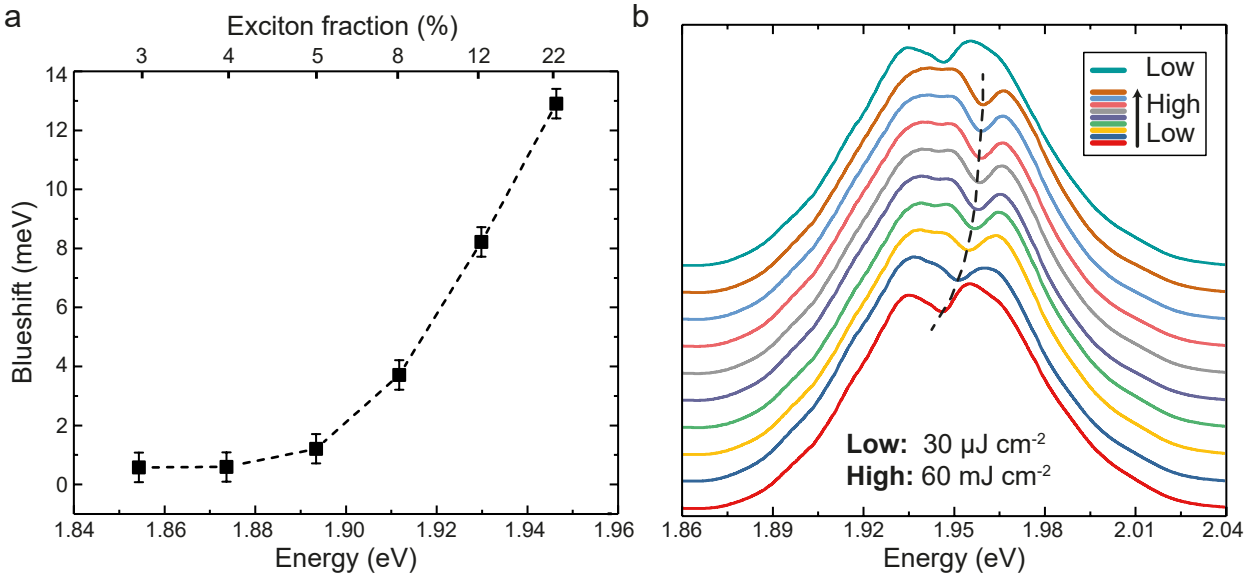

Figure 6.4 (a) High fluence (60 mJ cm^{-2}) time-averaged resonant blueshift of the LP mode as a function of the initial BSWP energy and corresponding exciton fraction, extracted from the coupled harmonic oscillator model shown in Fig. 6.2a. (b) Power sweep in steps of 7.6 mJ cm^{-2} for the highest blueshift/exciton fraction in Fig. 6.4a, showing that the shift is reversible and larger than the LP linewidth of 7∼8 meV.

is governed by a dissipative Gross-Pitaevskii equation of the form shown in Eq. (2.82) but in momentum space, where the BSW dispersion is described by Eq. (6.1). To reproduce our experimental conditions, the pump field is taken to be a Gaussian in momentum space modulated by a positively chirped temporal Gaussian envelope

$$F_p(k,t) = \sqrt{\frac{|C_k|^2\gamma_{LP}I_0}{\hbar\omega_p}} \cdot G(k) \cdot \sqrt{\frac{\sigma_t^2}{\sigma_t^2 + i\mathrm{GVD}d}} \cdot e^{-\frac{(t-t_0)^2}{2(\sigma_t^2+i\mathrm{GVD}d)}}, \tag{6.2}$$

with

$$G(k) = \frac{1}{\sqrt{A}} \cdot \frac{\sqrt{2\pi}}{\sigma_k} \cdot e^{\frac{-[k_x^2+(k_y-k_{y0})^2]}{4\sigma_k^2}}. \tag{6.3}$$

The corresponding real space LP field is then given by the inverse Fourier transform of $\psi(k,t)$, defined as

$$\psi(r,t) = \frac{1}{\sqrt{A}} \sum_k \psi(k,t) e^{irk}. \tag{6.4}$$

The simulation parameters are as follows. GVD = 61.86 fs^2/mm is the group velocity dispersion coefficient of BK7 glass at the pump wavelength of 645 nm ($\hbar\omega_p$ = 1.922 eV),

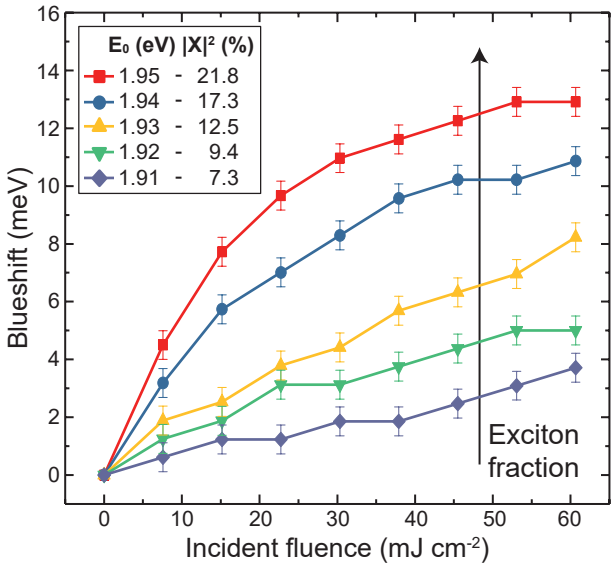

Figure 6.5 Saturation of the LP blueshift as a function of exciton fraction and incident pump fluence. The error bars correspond to an uncertainty of 0.5 meV in extracting the energy values from momentum-space maps.

$d = 40$ mm is the total thickness of optical elements in the path of the laser pulse, $\sigma_t = 30$ fs, $|C_k|$ is the Hopfield coefficient for the LP photon fraction at the pump wavevector, $\gamma_{LP} = 1.03 \cdot 10^{13}$ s^{-1}, $\sigma_k = 0.3\ \mu m^{-1}$ and $k_{y0} = 11.1\ \mu$m^{-1} is the center pump wavevector. The LP field is calculated in momenta intervals of $dk_x = 2\pi/L_x$ and $dk_y = 2\pi/L_y$ assuming periodic boundary conditions over the monolayer dimensions of $L_x = 20\ \mu$m and $L_y = 90\ \mu$m, with $A = L_x L_y$ being the quantization area. For the LP dispersion, $v_g = 1.49 \cdot 10^8$ m s^{-1} and $E_0 = 0.84$ eV. From the incident energy $E_{in} = \frac{P_{in}}{f} = \frac{9.25\ \mu\text{W}}{10\ \text{kHz}} = 0.93$ nJ, where P_{in} is the average power incident on the sample and f the repetition rate of the laser, the peak incident power is found to be $I_0 = \frac{E_{in}}{\sigma_t \sqrt{\pi}} = 17.4$ kW.

Figure 6.6a shows the calculated time evolution of the number of polaritons in momentum space $|\psi(k,t)|^2$ for modes with $k_x = 0$. The pump pulse is centered at $t = 300$ fs and the total number of polaritons peaks at $t = 364$ fs. The momentum space grid showing the polariton population in all modes considered in the calculation at the instant of peak total number of polaritons is shown in Fig. 6.6b, with the pump centered at k_{y0}.

Given that our measurements were performed using pulsed excitation, we illustrate in Figure 6.7 the underlying temporal dynamics of the spatial density of BSWPs under our experimental conditions. The temporal profile of the pump is traced in a solid white line. During the pump pulse, the density of polaritons is highest close to the excitation spot, centered at

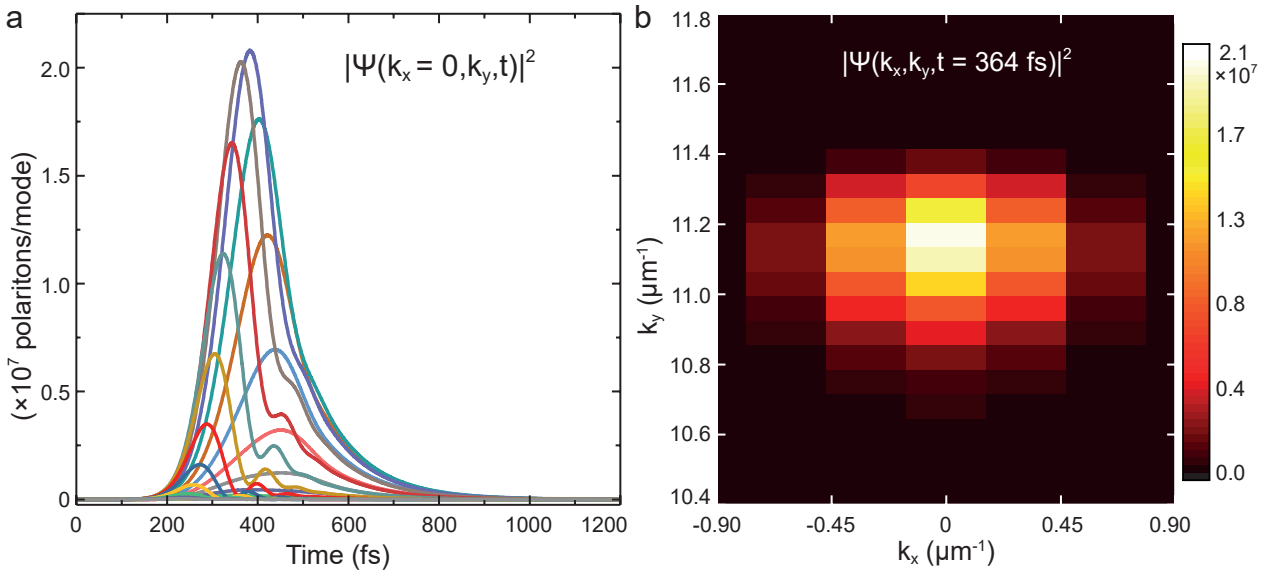

Figure 6.6 (a) Time evolution of the number of polaritons in momentum space for modes with $k_x = 0$. (b) Momentum space map showing the polariton population at the instant of peak total number of polaritons.

$\mathbf{r} = 0$. As the pump vanishes, the polariton wavepacket can be clearly seen as it propagates downwards with a group velocity of $1.49{\cdot}10^8$ m s^{-1}.

6.6 Estimation of the interaction energies

We consider an effective polariton-polariton interaction Hamiltonian of the form shown in Eq. (2.76). Although this Hamiltonian describes a local interaction in space, it critically accounts for the varying exciton fractions as a function of momenta, which cannot be accounted for in the GP equation. In this framework, the experimental values of the k dependent LP blueshift $\Delta E_{LP}(k)$ are directly related to the polariton population in momentum space through Eq. (2.78). The quantity $V^{PP}_{k,k',q}$ is the effective polariton-polariton interaction energy, which is independent of the choice of quantization area $A = L_x L_y$, and contains contributions arising from exciton-exciton Coulomb repulsion (V_{XX}) and saturation due to phase space filling (V_{SAT}). Considering each mechanism individually, we can obtain the exciton-exciton interaction energy as

$$V_{XX}(k) = \frac{\Delta E_{LP}(k)}{2|X_k|^2 \sum_{k'} |X_{k'}|^2 |\psi(k')|^2} \tag{6.5}$$

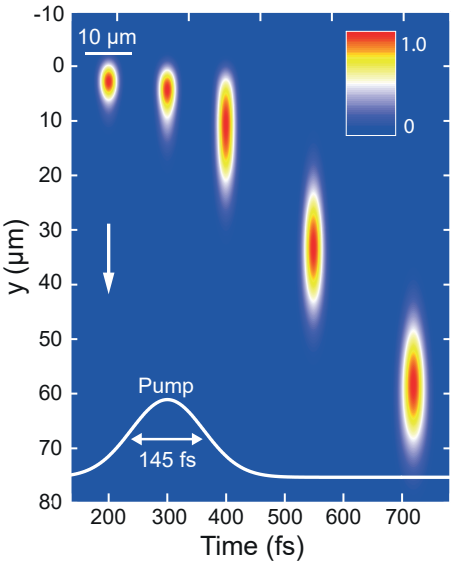

Figure 6.7 Calculated time snapshots of the spatial density of BSWPs following the arrival of the pump pulse, traced in a solid white line. The chirped pump pulse has an estimated FWHM of 145 fs. The polariton wavepacket is initially concentrated close to the excitation spot. As the pump vanishes, it can be seen propagating downwards at a group velocity of $1.49{\cdot}10^8$ m s^{-1}. The propagation traces were displaced laterally so that the center of the excitation spot coincides with the time at which the snapshot was taken. The top scale bar is related to the spatial dimensions of the propagation traces in the horizontal direction.

and the saturation interaction energy as

$$V_{SAT}(k) = \frac{\Delta E_{LP}(k)}{\begin{array}{r} 2|C_k||X_k|\sum_{k'}|X_{k'}|^2|\psi(k')|^2 \\ +\,6|X_k|^2\sum_{k'}|C_{k'}||X_{k'}||\psi(k')|^2 \end{array}}. \tag{6.6}$$

The experimental values obtained using Eqs. (6.5) and (6.6) and the calculated polariton population in momentum space shown in Fig. 6.6b are shown in Fig. 6.8. The interaction constants were calculated at an incident pump power below the saturation of the blueshift (7.6 mJ cm^{-2}) and at the instant when the total number of polaritons averaged by their exciton fractions was highest ($t = 346$ fs). The average interaction energies are $V_{XX} = (2.8 \pm 1.0) \cdot 10^{-4}$ μeV and $V_{SAT} = (2.6 \pm 1.1) \cdot 10^{-5}$ μeV. In both cases, instead of constant values, different interaction energies were found for different wavevectors (and corresponding exciton and photon fractions). Therefore the model does not allow us to determine which interaction mechanism plays a dominant role in the observed blueshift. Although the variation in V_{XX} is smaller, the observed blueshift is likely due to a combination of both Coulomb interactions and saturation.

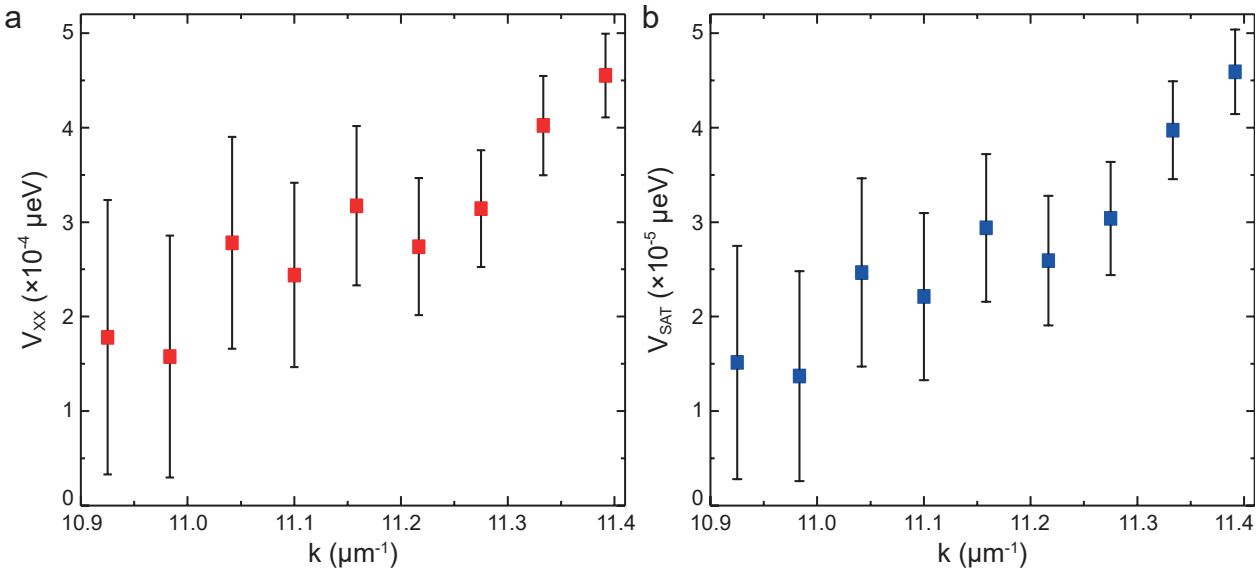

Figure 6.8 (a) Experimental interaction energies due to exciton-exciton Coulomb repulsion and (b) to saturation due to phase space filling.

6.7 Estimation of the interaction constants

In typical experiments where the lower polariton mode is excited resonantly by a narrow pump (in energy and momentum), the local experimental blueshift is related to the local polariton density by the polariton-polariton interaction constant as

$$\Delta E_{LP}(r) = g_{LP}|\psi(r)|^2. \tag{6.7}$$

For single-mode excitation and low propagation distances, the polariton distribution in real-space is constant and the interaction constant is simply given by

$$g_{LP} = \frac{\Delta E_{LP}}{|\psi|^2}. \tag{6.8}$$

Here, the polariton distribution in real-space will be modified by the energy and momentum width of the pump and the long propagation constants. The center wavelength and momentum of the pump will then be considered for estimating g_{LP}. The real space distribution is accounted for by a normalized integral of the polariton density at the instant of highest polariton population. Because the blueshift is detected from the spectrum of the emitted light, the density is weighed by the emitted intensity ($|\psi|^2$). The interaction constant is then

obtained from

$$g_{LP} = \frac{\Delta E_{LP} \cdot \int\int |\psi(r, t_{max})|^2 dr}{\int\int |\psi(r, t_{max})|^4 dr}. \tag{6.9}$$

Although our experiments cannot determine the relative contribution of each interaction mechanism over the range of momenta probed, we can separately estimate the interaction constants required to explain the observed blueshift if either mechanism was uniquely present. From the calculated real space polariton density shown in Fig. 6.7 we can estimate a polariton-polariton interaction constant of $g_{LP} = 6 \cdot 10^{-4}$ μeV μm^2. For this estimate, we considered the case of a blueshift of $\Delta E_{LP} = 1.25$ meV, exciton fraction of 10%, at an incident pump power below the saturation of the blueshift (7.6 mJ cm^{-2}) and at the instant $t_{max} = 364$ fs of highest total polariton density. The peak density was $4.1 \cdot 10^6$ polaritons/μm^2. Through Eqs. (2.80) and (2.81), this corresponds to exciton-exciton or PSF interaction constants of $g_{XX} = 6 \cdot 10^{-2}$ μeV μm^2 and $g_{SAT} = 5 \cdot 10^{-3}$ μeV μm^2, respectively. These estimates also suggest that both Coulomb interactions and PSF may contribute to the blueshift within the range of momenta probed in our system.

We can compare these interaction constants to their respective theoretical values. The exciton-exciton interaction constant in TMDs can be estimated using $g_{XX} \simeq 2.07 E_{1s} \lambda_X^2 = 1.9$ μeV μm^2, where $E_{1s} = 0.32$ eV is the 1s exciton binding energy and $\lambda_X = 1.7$ nm is the 1s exciton radius [29]. The numerical prefactor in the expression for PSF depends on the form of the exciton wavefunctions. For 1s excitons, it is often estimated [34] as $g_{SAT} \simeq 7.18 \hbar \Omega_R \lambda_X^2 = 0.87$ μeV μm^2. Both theoretical values far exceed those obtained from the blueshift. Part of the discrepancy may be due to the fact that we overestimate the polariton density by ignoring exciton-exciton annihilation and relaxation into dark dipole and spin-forbidden exciton states. Note also that we use the maximum instantaneous polariton density in our estimate although we measure a time-averaged blueshift. We have examined these various possible sources of error and they are not expected to modify the value by more than an order of magnitude. In addition, our measured exciton-exciton interaction constant is similar to a recent measurement in encapsulated $MoSe_2$ at 4K [140]. This instead suggests a need for further work on exciton-exciton interactions in TMDs to explain the discrepancy between experiments and the current theory.

6.8 Nonlinear polariton source

Finally, we demonstrate how the optical control of the LP mode can be used as a nonlinear source of polaritons, by pumping in a configuration similar to that which leads to bistability under continuous wave pumping [7]. For this, we excite the LP mode with an exciton fraction

of 36% at 633 nm with a spectrally-filtered 3 nm-wide pump. At low incident powers, very little light is coupled into the propagating polariton mode, as shown on inset 1 in Fig. 6.9. As the pump power is increased, the LP mode blueshifts and the propagating part of the BSWP dispersion moves closer to resonance with the pump (insets 2 and 3). At high power, the pump laser is fully resonant with the polariton mode and launches a propagating surface wave, which through coupling to the underlying bare mode is able to propagate far beyond the flake dimensions. The normalized intensities of the propagating and scattered components, which depend on the selected integration areas, are shown in the blue and red curves, respectively. The nonlinearity leads to a superlinear fluence dependence for the propagating component at pump fluences above 1 mJ cm^{-2}. For a single pump beam, the nonlinear polariton source behaves as an all-optical discriminator (or diode) in forward operation. For two or more beams, it behaves as an all-optical transistor or switch.

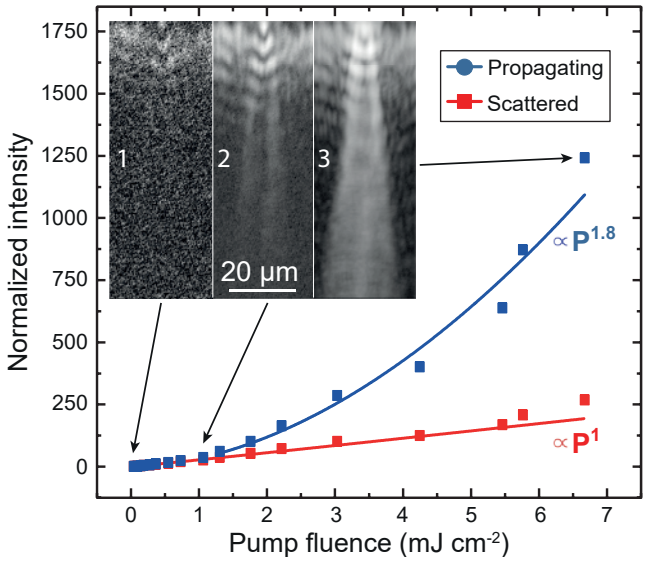

Figure 6.9 A nonlinear polariton source at an exciton fraction of 36%, where the incident power can block or launch a beam of propagating BSWPs. The blue and red curves show the normalized intensity of the propagating and scattered beams, respectively, where the first is found to have a superlinear dependence on pump fluence, indicating its nonlinear origin.

6.9 Conclusion

Our demonstration of strong light-matter coupling between excitons in two-dimensional materials and BSWs forms a new platform for enabling practical nonlinear polariton devices operating at room temperature. All-optical polariton transistors, switches and logic circuits

could be used for ultrafast optical information processing at speeds well beyond the capabilities of existing electronic devices [15, 141–143]. Because of their propagating nature, BSWPs can play the dual role of active elements and low-loss optical interconnects. The structure is simple to fabricate, not requiring the deposition of a top dielectric mirror, and it can be tailored for other two-dimensional materials or for van der Waals heterostructures with engineered optical properties. In particular, TMDs encapsulated by hexagonal boron nitride show improved surface flatness, screening from charged impurities and ambient stability. This leads to a suppression of loss mechanisms such as exciton-exciton annihilation and would allow higher polariton densities to be achieved in the nonlinear regime [139]. Finally, polariton propagation losses in our experiment stem mainly from leakage into the immersion optics, which for low-power operation could be reduced by an increase in the number of dielectric pairs or even completely avoided by the use of surface gratings for external in- and out-coupling [144].

CHAPTER 7 CONCLUSION

7.1 Advancement of knowledge

The main goal of this thesis was to investigate the enhancement of polariton nonlinearities to enable their use in practical nonlinear applications. We began by numerically exploring a new way in which polariton nonlinearities can be used for optical frequency mixing. We proposed the use of a non-centrosymmetric active layer, possessing a large second-order susceptibility $\chi^{(2)}$, to enable efficient radiative transitions between polariton modes. This process, which we called Rabi frequency generation, is forbidden in typical polariton systems in which only third-order nonlinearities are present. Because polaritons arise from strong coupling to the same cavity mode, we showed that they display excellent mode overlap and effectively eliminate the usual phase-matching constraint.

Next, we fabricated high quality microcavities containing a nonlinear organic dye with a large optical third-order susceptibility $\chi^{(3)}$. The main question we wanted to address was if polaritons would inherit the strong nonlinearity of the dye. Surprisingly, our fabricated microcavities showed a record value of the normalized coupling strength, indicating that they were operating in the ultrastrong coupling regime. This also allowed us to address the impact of the USC regime on observable material properties.

Upon resonant excitation of the lower polariton mode, we demonstrated efficient and tunable third-harmonic generation spanning the entire visible spectrum. Indeed, by correlating the THG conversion efficiencies and the polariton photon fraction, we confirmed that the strong nonlinearity of the dye was carried over to the polaritons via their photon component. Using a nonlinear transfer matrix method, we were able to explain the experimental results using a known value for the optical $\chi^{(3)}$, indicating that the nonlinear properties of the dye were not noticeably affected in the USC regime.

In Chapter 5, we performed numerical simulations to reproduce the recent observation by our collaborators of room temperature polariton superfluidity in an organic microcavity. In this system, the cavity material is not strongly nonlinear and the weak polariton interactions stem mainly from saturation effects. Using experimental parameters describing the cavity, we simulated the flow of a polariton fluid against an obstacle at different polariton densities. We observed a transition from dissipative to superfluid (scattering free) behaviour at pump intensities consistent with the experimental value. We were able to reproduce the experimental observations and shed light on the complicated temporal dynamics of the system, which

included transient damped oscillations and the ejection of vortex pairs.

Finally, we turned our attention to transition metal dichalcogenides. Such materials are expected to enable strong exciton-exciton interactions because of the reduced dielectric screening at the monolayer level. Previous attempts to observe polariton nonlinearities in microcavities embedding TMD monolayers were unsuccessful due to the high losses of either the mirrors or the active material itself. We proposed to combine a surface wave propagating on a low-loss dielectric mirror and a monolayer of tungsten disulfide, which possesses a strong and narrow exciton absorption.

As a consequence of the low losses, we were able to generate Bloch surface wave polaritons with very long propagation distances. This is especially interesting in the context of cascadable optical elements in polaritonic circuits. More importantly, together with the narrow linewidths, the enhancement of the electric field and its confinement to the monolayer enabled us to observe clear and reversible blueshifts of the lower polariton mode with increasing pump fluences. This constituted the first demonstration of polariton nonlinearities in this class of materials and enabled us to measure the strength of their interactions. As a proof-of-principle, we used the nonlinearity to implement a nonlinear polariton source, similar to an all-optical diode or discriminator.

7.2 Limits and constraints

In order to enable practical nonlinear applications, a number of material properties are required: room-temperature excitonic behaviour, high photostability, strong exciton nonlinearities and low losses. We have yet to find a material set in which all these requirements are simultaneously fulfilled. Cavities embedding inorganic quantum wells only operate at cryogenic temperatures, but satisfy all the remaining criteria. Organic semiconductors support stable excitons at room-temperature, but their weak nonlinearities require high pump fluences. As a result, they must be operated in the pulsed regime in order to reduce thermal damage. This effect was present in our third-harmonic measurements and in the superfluidity experiments done by our collaborators. Although we did not observe thermal damage in our demonstration of polariton nonlinearities in monolayer TMDs, it also required prohibitively high pump fluences for practical technological applications.

7.3 Future research

Future polariton experiments will like make use of a combination of different materials and approaches in order to enable practical nonlinear devices that can operate at room-temperature

and at excitation powers comparable to inorganic quantum well microcavities. Here we highlight some of the most promising ones.

Cavity design: In our experiments, light was confined either inside a planar microcavity or to the surface of a dielectric mirror. The second approach is more interesting for enhancing nonlinear effects because of the stronger electric field confinement. Compared to planar microcavities, Bloch surface modes have the advantages of reduced losses, due to the absence of metallic layers, and of easier fabrication, since there is no need to deposit a top mirror. A clear disadvantage is that the dispersion of Bloch surface wave polaritons has a monotonic slope, while nonlinear polariton effects such as condensation and lasing rely on the buildup of a significant population at the bottom of a parabolic dispersion. An interesting strategy to obtain a minimum in the dispersion of BSWPs is to pattern one-dimensional gratings to either the top dielectric layer or to the semiconductor material itself. In addition, gratings can also be used for in- and out-coupling of light into BSWP modes directly for the air side [144].

Organic materials: New nonlinear dyes with stronger nonlinearities, higher photostability and lower losses are constantly being developed. When embedded in high quality DBR microcavities, such materials might enable the elusive demonstration of room-temperature parametric scattering and amplification in organic microcavities. In the context of electrical excitation, purified carbon nanotubes have a strong and narrow exciton absorption which might enable polariton lasing in the NIR or telecom wavelengths [145, 146].

Layered semiconductors: There are a number of promising materials with sufficiently large exciton binding energies for room-temperature operation and which are considerably more photostable than organic semiconductors. We explored the group of transition metal dichalcogenides, which despite showing weaker nonlinearities than expected were surprisingly stable and must be explored further. Monolayer TMDs are especially interesting for the study of room-temperature BE condensates because they are both more photostable and much less disordered than organic semiconductors. In addition, a number of layered semiconductors has been shown to exhibit large second- and third-order nonlinearities, which could be imparted onto BSWPs via their photonic component [147–149]. Such materials should be investigated for their viability for polaritonics and might enable complex nonlinear effects to be observed.

Other materials: Interesting candidates for nonlinear polaritonics include inorganic perovskites [119, 120], which have strong nonlinearities but high losses, and wide-bandgap inorganic semiconductors, such as zinc oxide (ZnO) and gallium nitride (GaN), in which polariton lasing has already been demonstrated [55, 57, 150].

Excitons: Ground-state excitons do not possess a dipole moment and their interactions are

predominantly due to Coulomb exchange, which depends strongly on the dielectric environment and the size of the exciton radius. Two promising alternatives to enhance polariton nonlinearities are to use either ground-state excitons which have been given a dipolar character or higher order excitonic Rydberg states, which have both a large radius and dipole moment.

In the first case, the typical experimental configuration consists of a pair of asymmetric double quantum wells which are placed inside a microcavity [151]. One of the quantum wells supports a direct exciton, through which strong light-matter coupling is achieved. In addition, the proximity of the two quantum wells allows the creation of indirect excitons, where the electron and hole are in separate wells. This indirect exciton has a static dipole moment along the growth direction, enabling dipole-dipole interactions to take place. Under an applied bias, the two types of excitons mix and the resulting polaritons, called dipolaritons, acquire a dipolar character and have been shown to enhance polariton nonlinearities by an order of magnitude [152]. Dipolaritons can in principle also be obtained with monolayer TMDs separated by a small spacer via the mixing of direct and interlayer excitons [153]. This interesting approach, however, has not been explored yet in the context of polaritonics.

The second approach consists of using excitons with a higher principal quantum number. Such excitons interact strongly via dipole-dipole repulsion and have been predicted to lead to the enhancement of exciton nonlinearities by several orders of magnitude [154]. However, the small oscillator strength typical of Rydberg excitons has limited their use in polaritonics. Recent exceptions are inorganic perovskites, where condensation of Rydberg exciton-polaritons has been claimed [155] and TMD monolayers where strong coupling has been demonstrated with the 2s exciton [156]. However, both demonstrations were performed at temperatures below 150K.

REFERENCES

[1] B. Hacker, S. Welte, G. Rempe, and S. Ritter, "A photon–photon quantum gate based on a single atom in an optical resonator," *Nature*, vol. 536, no. 7615, p. 193, 2016.

[2] L.-M. Duan and H. J. Kimble, "Scalable photonic quantum computation through cavity-assisted interactions," *Phys. Rev. Lett.*, vol. 92, p. 127902, Mar 2004.

[3] R. J. Thompson, G. Rempe, and H. J. Kimble, "Observation of normal-mode splitting for an atom in an optical cavity," *Phys. Rev. Lett.*, vol. 68, pp. 1132–1135, Feb 1992.

[4] T. Yoshie, A. Scherer, J. Hendrickson, G. Khitrova, H. Gibbs, G. Rupper, C. Ell, O. Shchekin, and D. Deppe, "Vacuum rabi splitting with a single quantum dot in a photonic crystal nanocavity," *Nature*, vol. 432, no. 7014, p. 200, 2004.

[5] R. Chikkaraddy, B. de Nijs, F. Benz, S. J. Barrow, O. A. Scherman, E. Rosta, A. Demetriadou, P. Fox, O. Hess, and J. J. Baumberg, "Single-molecule strong coupling at room temperature in plasmonic nanocavities," *Nature*, vol. 535, no. 7610, p. 127, 2016.

[6] I. Carusotto and C. Ciuti, "Quantum fluids of light," *Rev. Mod. Phys.*, vol. 85, pp. 299–366, Feb 2013.

[7] D. Sanvitto and S. Kéna-Cohen, "The road towards polaritonic devices," *Nature Materials*, vol. 15, no. 10, pp. 1061–1073, 2016.

[8] R. M. Stevenson, V. N. Astratov, M. S. Skolnick, D. M. Whittaker, M. Emam-Ismail, A. I. Tartakovskii, P. G. Savvidis, J. J. Baumberg, and J. S. Roberts, "Continuous wave observation of massive polariton redistribution by stimulated scattering in semiconductor microcavities," *Phys. Rev. Lett.*, vol. 85, pp. 3680–3683, Oct 2000.

[9] P. G. Savvidis, J. J. Baumberg, R. M. Stevenson, M. S. Skolnick, D. M. Whittaker, and J. S. Roberts, "Angle-resonant stimulated polariton amplifier," *Phys. Rev. Lett.*, vol. 84, pp. 1547–1550, Feb 2000.

[10] J. J. Baumberg, P. G. Savvidis, R. M. Stevenson, A. I. Tartakovskii, M. S. Skolnick, D. M. Whittaker, and J. S. Roberts, "Parametric oscillation in a vertical microcavity: A polariton condensate or micro-optical parametric oscillation," *Phys. Rev. B*, vol. 62, pp. R16 247–R16 250, Dec 2000.

[11] A. Baas, J. P. Karr, H. Eleuch, and E. Giacobino, "Optical bistability in semiconductor microcavities," *Phys. Rev. A*, vol. 69, p. 023809, Feb 2004.

[12] S. Kéna-Cohen and S. Forrest, "Room-temperature polariton lasing in an organic single-crystal microcavity," *Nature Photonics*, vol. 4, no. 6, pp. 371–375, 2010.

[13] A. Das, J. Heo, M. Jankowski, W. Guo, L. Zhang, H. Deng, and P. Bhattacharya, "Room temperature ultralow threshold gan nanowire polariton laser," *Phys. Rev. Lett.*, vol. 107, p. 066405, Aug 2011.

[14] C. Schneider, A. Rahimi-Iman, N. Y. Kim, J. Fischer, I. G. Savenko, M. Amthor, M. Lermer, A. Wolf, L. Worschech, V. D. Kulakovskii *et al.*, "An electrically pumped polariton laser," *Nature*, vol. 497, no. 7449, p. 348, 2013.

[15] D. Ballarini, M. De Giorgi, E. Cancellieri, R. Houdré, E. Giacobino, R. Cingolani, A. Bramati, G. Gigli, and D. Sanvitto, "All-optical polariton transistor," *Nature communications*, vol. 4, p. 1778, 2013.

[16] T. Gao, P. S. Eldridge, T. C. H. Liew, S. I. Tsintzos, G. Stavrinidis, G. Deligeorgis, Z. Hatzopoulos, and P. G. Savvidis, "Polariton condensate transistor switch," *Phys. Rev. B*, vol. 85, p. 235102, Jun 2012.

[17] V. M. Menon, L. I. Deych, and A. A. Lisyansky, "Nonlinear optics: Towards polaritonic logic circuits," *Nature Photonics*, vol. 4, no. 6, p. 345, 2010.

[18] T. C. H. Liew, A. V. Kavokin, and I. A. Shelykh, "Optical circuits based on polariton neurons in semiconductor microcavities," *Phys. Rev. Lett.*, vol. 101, p. 016402, Jul 2008.

[19] F. Barachati, S. De Liberato, and S. Kéna-Cohen, "Generation of rabi-frequency radiation using exciton-polaritons," *Phys. Rev. A*, vol. 92, p. 033828, Sep 2015.

[20] F. Barachati, J. Simon, Y. A. Getmanenko, S. Barlow, S. R. Marder, and S. Kéna-Cohen, "Tunable third-harmonic generation from polaritons in the ultrastrong coupling regime," *ACS Photonics*, vol. 5, no. 1, pp. 119–125, 2018.

[21] G. Lerario, A. Fieramosca, F. Barachati, D. Ballarini, K. S. Daskalakis, L. Dominici, M. De Giorgi, S. A. Maier, G. Gigli, S. Kéna-Cohen *et al.*, "Room-temperature superfluidity in a polariton condensate," *Nature Physics*, vol. 13, no. 9, p. 837, 2017.

[22] F. Barachati, A. Fieramosca, S. Hafezian, J. Gu, B. Chakraborty, D. Ballarini, L. Martinu, V. Menon, D. Sanvitto, and S. Kéna-Cohen, "Interacting polariton fluids in a monolayer of tungsten disulfide," *Nature Nanotechnology*, 2018.

[23] G. Panzarini, L. C. Andreani, A. Armitage, D. Baxter, M. S. Skolnick, V. N. Astratov, J. S. Roberts, A. V. Kavokin, M. R. Vladimirova, and M. A. Kaliteevski, "Cavity-polariton dispersion and polarization splitting in single and coupled semiconductor microcavities," *Physics of the Solid State*, vol. 41, no. 8, pp. 1223–1238, Aug 1999.

[24] M. Richard, "The not-so-effective mass of photons in a planar optical cavity," 2015.

[25] A. Kavokin, J. J. Baumberg, G. Malpuech, and F. P. Laussy, "Microcavities, series on semiconductor science and technology," 2007.

[26] M. Steger, G. Liu, B. Nelsen, C. Gautham, D. W. Snoke, R. Balili, L. Pfeiffer, and K. West, "Long-range ballistic motion and coherent flow of long-lifetime polaritons," *Phys. Rev. B*, vol. 88, p. 235314, Dec 2013.

[27] S. Kéna-Cohen, S. A. Maier, and D. D. C. Bradley, "Ultrastrongly coupled exciton-polaritons in metal-clad organic semiconductor microcavities," *Advanced Optical Materials*, vol. 1, no. 11, pp. 827–833, 2013.

[28] P. Yeh, *Optical waves in layered media*. Wiley-Interscience, 2005, vol. 61.

[29] V. Shahnazaryan, I. Iorsh, I. A. Shelykh, and O. Kyriienko, "Exciton-exciton interaction in transition-metal dichalcogenide monolayers," *Phys. Rev. B*, vol. 96, p. 115409, Sep 2017.

[30] R. W. Boyd, *Nonlinear Optics*, 3rd ed. Academic Press, 2008.

[31] C. Cohen-Tannoudji, J. Dupont-Roc, and G. Grynberg, "Photons and atoms-introduction to quantum electrodynamics," *Photons and Atoms-Introduction to Quantum Electrodynamics, by Claude Cohen-Tannoudji, Jacques Dupont-Roc, Gilbert Grynberg, pp. 486. ISBN 0-471-18433-0. Wiley-VCH, February 1997.*, p. 486, 1997.

[32] C. Ciuti, G. Bastard, and I. Carusotto, "Quantum vacuum properties of the intersubband cavity polariton field," *Phys. Rev. B*, vol. 72, p. 115303, Sep 2005.

[33] S. De Liberato, "Light-matter decoupling in the deep strong coupling regime: The breakdown of the purcell effect," *Phys. Rev. Lett.*, vol. 112, p. 016401, Jan 2014.

[34] C. Ciuti, P. Schwendimann, and A. Quattropani, "Theory of polariton parametric interactions in semiconductor microcavities," *Semiconductor Science and Technology*, vol. 18, no. 10, p. S279, 2003.

[35] J. J. Hopfield, "Theory of the contribution of excitons to the complex dielectric constant of crystals," *Phys. Rev.*, vol. 112, pp. 1555–1567, Dec 1958.

[36] G. Scalari, C. Maissen, D. Turčinková, D. Hagenmüller, S. De Liberato, C. Ciuti, C. Reichl, D. Schuh, W. Wegscheider, M. Beck, and J. Faist, "Ultrastrong coupling of the cyclotron transition of a 2d electron gas to a thz metamaterial," *Science*, vol. 335, no. 6074, pp. 1323–1326, 2012.

[37] S. Gambino, M. Mazzeo, A. Genco, O. Di Stefano, S. Savasta, S. Patanè, D. Ballarini, F. Mangione, G. Lerario, D. Sanvitto, and G. Gigli, "Exploring light-matter interaction phenomena under ultrastrong coupling regime," *ACS Photonics*, vol. 1, no. 10, pp. 1042–1048, 2014.

[38] E. Eizner, J. Brodeur, F. Barachati, A. Sridharan, and S. Kéna-Cohen, "Organic photodiodes with an extended responsivity using ultrastrong light-matter coupling," *ACS Photonics*, vol. 5, no. 7, pp. 2921–2927, 2018.

[39] J. Feist, J. Galego, and F. J. Garcia-Vidal, "Polaritonic chemistry with organic molecules," *ACS Photonics*, vol. 5, no. 1, pp. 205–216, 2018.

[40] E. Orgiu, J. George, J. Hutchison, E. Devaux, J. Dayen, B. Doudin, F. Stellacci, C. Genet, J. Schachenmayer, C. Genes, G. Pupillo, T. Samorì, and T. Ebbesen, "Conductivity in organic semiconductors hybridized with the vacuum field," *Nature Materials*, 2015.

[41] J. A. Hutchison, T. Schwartz, C. Genet, E. Devaux, and T. W. Ebbesen, "Modifying chemical landscapes by coupling to vacuum fields," *Angewandte Chemie International Edition*, vol. 51, no. 7, pp. 1592–1596, 2012.

[42] N. Bobrovska, M. Matuszewski, K. S. Daskalakis, S. A. Maier, and S. Kéna-Cohen, "Dynamical instability of a nonequilibrium exciton-polariton condensate," *ACS Photonics*, vol. 5, no. 1, pp. 111–118, 2018.

[43] J. J. Baumberg and P. G. Lagoudakis, "Parametric amplification and polariton liquids in semiconductor microcavities," *physica status solidi (b)*, vol. 242, no. 11, pp. 2210–2223, 2005.

[44] P. G. Savvidis, C. Ciuti, J. J. Baumberg, D. M. Whittaker, M. S. Skolnick, and J. S. Roberts, "Off-branch polaritons and multiple scattering in semiconductor microcavities," *Phys. Rev. B*, vol. 64, p. 075311, Jul 2001.

[45] M. Wouters and I. Carusotto, "Parametric oscillation threshold of semiconductor microcavities in the strong coupling regime," *Phys. Rev. B*, vol. 75, p. 075332, Feb 2007.

[46] M. Saba, C. Ciuti, J. Bloch, V. Thierry-Mieg, R. André, L. S. Dang, S. Kundermann, A. Mura, G. Bongiovanni, J. Staehli *et al.*, "High-temperature ultrafast polariton parametric amplification in semiconductor microcavities," *Nature*, vol. 414, no. 6865, p. 731, 2001.

[47] I. Carusotto and C. Ciuti, "Spontaneous microcavity-polariton coherence across the parametric threshold: Quantum monte carlo studies," *Phys. Rev. B*, vol. 72, p. 125335, Sep 2005.

[48] J. Kasprzak, M. Richard, S. Kundermann, A. Baas, P. Jeambrun, J. Keeling, F. Marchetti, M. Szymańska, R. Andre, J. Staehli *et al.*, "Bose–einstein condensation of exciton polaritons," *Nature*, vol. 443, no. 7110, pp. 409–414, 2006.

[49] A. Imamoğlu, R. J. Ram, S. Pau, and Y. Yamamoto, "Nonequilibrium condensates and lasers without inversion: Exciton-polariton lasers," *Phys. Rev. A*, vol. 53, pp. 4250–4253, Jun 1996.

[50] K. Daskalakis, S. Maier, R. Murray, and S. Kéna-Cohen, "Nonlinear interactions in an organic polariton condensate," *Nature materials*, vol. 13, no. 3, pp. 271–278, 2014.

[51] J. D. Plumhof, T. Stöferle, L. Mai, U. Scherf, and R. F. Mahrt, "Room-temperature bose–einstein condensation of cavity exciton–polaritons in a polymer," *Nature materials*, vol. 13, no. 3, pp. 247–252, 2014.

[52] T. Guillet, M. Mexis, J. Levrat, G. Rossbach, C. Brimont, T. Bretagnon, B. Gil, R. Butté, N. Grandjean, L. Orosz, F. Réveret, J. Leymarie, J. Zúñiga-Pérez, M. Leroux, F. Semond, and S. Bouchoule, "Polariton lasing in a hybrid bulk zno microcavity," *Applied Physics Letters*, vol. 99, no. 16, p. 161104, 2011.

[53] G. Christmann, R. Butté, E. Feltin, J.-F. Carlin, and N. Grandjean, "Room temperature polariton lasing in a GaN/AlGaN multiple quantum well microcavity," *Applied Physics Letters*, vol. 93, no. 5, p. 051102, 2008.

[54] S. Christopoulos, G. B. H. von Högersthal, A. J. D. Grundy, P. G. Lagoudakis, A. V. Kavokin, J. J. Baumberg, G. Christmann, R. Butté, E. Feltin, J.-F. Carlin, and N. Grandjean, "Room-temperature polariton lasing in semiconductor microcavities," *Phys. Rev. Lett.*, vol. 98, p. 126405, Mar 2007.

[55] K. S. Daskalakis, P. S. Eldridge, G. Christmann, E. Trichas, R. Murray, E. Iliopoulos, E. Monroy, N. T. Pelekanos, J. J. Baumberg, and P. G. Savvidis, "All-dielectric gan microcavity: Strong coupling and lasing at room temperature," *Applied Physics Letters*, vol. 102, no. 10, p. 101113, 2013.

[56] R. Balili, V. Hartwell, D. Snoke, L. Pfeiffer, and K. West, "Bose-einstein condensation of microcavity polaritons in a trap," *Science*, vol. 316, no. 5827, pp. 1007–1010, 2007.

[57] P. Bhattacharya, T. Frost, S. Deshpande, M. Z. Baten, A. Hazari, and A. Das, "Room temperature electrically injected polariton laser," *Phys. Rev. Lett.*, vol. 112, p. 236802, Jun 2014.

[58] M. Sich, D. Krizhanovskii, M. Skolnick, A. V. Gorbach, R. Hartley, D. V. Skryabin, E. Cerda-Méndez, K. Biermann, R. Hey, and P. Santos, "Observation of bright polariton solitons in a semiconductor microcavity," *Nature photonics*, vol. 6, no. 1, p. 50, 2012.

[59] D. Sanvitto, F. Marchetti, M. Szymańska, G. Tosi, M. Baudisch, F. Laussy, D. Krizhanovskii, M. Skolnick, L. Marrucci, A. Lemaitre *et al.*, "Persistent currents and quantized vortices in a polariton superfluid," *Nature Physics*, vol. 6, no. 7, p. 527, 2010.

[60] C. Ciuti and I. Carusotto, "Quantum fluid effects and parametric instabilities in microcavities," *physica status solidi (b)*, vol. 242, no. 11, pp. 2224–2245, 2005.

[61] A. Baas, J.-P. Karr, M. Romanelli, A. Bramati, and E. Giacobino, "Optical bistability in semiconductor microcavities in the nondegenerate parametric oscillation regime: Analogy with the optical parametric oscillator," *Phys. Rev. B*, vol. 70, p. 161307, Oct 2004.

[62] J. P. Karr, A. Baas, R. Houdré, and E. Giacobino, "Squeezing in semiconductor microcavities in the strong-coupling regime," *Phys. Rev. A*, vol. 69, p. 031802, Mar 2004.

[63] I. Carusotto and C. Ciuti, "Probing microcavity polariton superfluidity through resonant rayleigh scattering," *Phys. Rev. Lett.*, vol. 93, p. 166401, Oct 2004.

[64] A. Amo, J. Lefrère, S. Pigeon, C. Adrados, C. Ciuti, I. Carusotto, R. Houdré, E. Giacobino, and A. Bramati, "Superfluidity of polaritons in semiconductor microcavities," *Nature Physics*, vol. 5, no. 11, pp. 805–810, 2009.

[65] J. Schmutzler, M. Aßmann, T. Czerniuk, M. Kamp, C. Schneider, S. Höfling, and M. Bayer, "Nonlinear spectroscopy of exciton-polaritons in a gaas-based microcavity," *Phys. Rev. B*, vol. 90, p. 075103, Aug 2014.

[66] T. Chervy, J. Xu, Y. Duan, C. Wang, L. Mager, M. Frerejean, J. A. W. Münninghoff, P. Tinnemans, J. A. Hutchison, C. Genet, A. E. Rowan, T. Rasing, and T. W. Ebbesen, "High-efficiency second-harmonic generation from hybrid light-matter states," *Nano Letters*, vol. 16, no. 12, pp. 7352–7356, 2016, pMID: 27960510.

[67] S. Gambino, M. Mazzeo, A. Genco, O. Di Stefano, S. Savasta, S. Patanè, D. Ballarini, F. Mangione, G. Lerario, D. Sanvitto, and G. Gigli, "Exploring light-matter interaction phenomena under ultrastrong coupling regime," *ACS Photonics*, vol. 1, no. 10, pp. 1042–1048, 2014.

[68] T. Schwartz, J. A. Hutchison, C. Genet, and T. W. Ebbesen, "Reversible switching of ultrastrong light-molecule coupling," *Phys. Rev. Lett.*, vol. 106, p. 196405, May 2011.

[69] S. De Liberato, C. Ciuti, and C. C. Phillips, "Terahertz lasing from intersubband polariton-polariton scattering in asymmetric quantum wells," *Phys. Rev. B*, vol. 87, p. 241304, Jun 2013.

[70] N. Shammah, C. C. Phillips, and S. De Liberato, "Terahertz emission from ac stark-split asymmetric intersubband transitions," *Phys. Rev. B*, vol. 89, p. 235309, Jun 2014.

[71] I. G. Savenko, I. A. Shelykh, and M. A. Kaliteevski, "Nonlinear terahertz emission in semiconductor microcavities," *Phys. Rev. Lett.*, vol. 107, p. 027401, Jul 2011.

[72] K. V. Kavokin, M. A. Kaliteevski, R. A. Abram, A. V. Kavokin, S. Sharkova, and I. A. Shelykh, "Stimulated emission of terahertz radiation by exciton-polariton lasers," *Applied Physics Letters*, vol. 97, no. 20, pp. –, 2010.

[73] A. V. Kavokin, I. A. Shelykh, T. Taylor, and M. M. Glazov, "Vertical cavity surface emitting terahertz laser," *Phys. Rev. Lett.*, vol. 108, p. 197401, May 2012.

[74] T. C. H. Liew, M. M. Glazov, K. V. Kavokin, I. A. Shelykh, M. A. Kaliteevski, and A. V. Kavokin, "Proposal for a bosonic cascade laser," *Phys. Rev. Lett.*, vol. 110, p. 047402, Jan 2013.

[75] A. Rodriguez, M. Soljacic, J. D. Joannopoulos, and S. G. Johnson, "$\chi^{(2)}$ and $\chi^{(3)}$ harmonic generation at a critical power in inhomogeneous doubly resonant cavities," *Opt. Express*, vol. 15, no. 12, pp. 7303–7318, Jun 2007.

[76] I. B. Burgess, Y. Zhang, M. W. McCutcheon, A. W. Rodriguez, J. Bravo-Abad, S. G. Johnson, and M. Lončar, "Design of an efficient terahertz source using triply resonant nonlinear photonic crystal cavities," *Opt. Express*, vol. 17, no. 22, pp. 20 099–20 108, Oct 2009.

[77] K. Rivoire, S. Buckley, and J. Vučković, "Multiply resonant high quality photonic crystal nanocavities," *Applied Physics Letters*, vol. 99, no. 1, pp. –, 2011.

[78] K. Rivoire, S. Buckley, and J. Vučković, "Multiply resonant photonic crystal nanocavities for nonlinear frequency conversion," *Opt. Express*, vol. 19, no. 22, pp. 22 198–22 207, Oct 2011.

[79] Y. Zhang, M. W. McCutcheon, I. B. Burgess, and M. Lončar, "Ultra-high-q te/tm dual-polarized photonic crystal nanocavities," *Opt. Lett.*, vol. 34, no. 17, pp. 2694–2696, Sep 2009.

[80] M. W. McCutcheon, P. B. Deotare, Y. Zhang, and M. Lončar, "High-q transverse-electric/transverse-magnetic photonic crystal nanobeam cavities," *Applied Physics Letters*, vol. 98, no. 11, pp. –, 2011.

[81] R. Houdré, C. Weisbuch, R. P. Stanley, U. Oesterle, and M. Ilegems, "Nonlinear emission of semiconductor microcavities in the strong coupling regime," *Phys. Rev. Lett.*, vol. 85, pp. 2793–2796, Sep 2000.

[82] D. M. Whittaker, "Classical treatment of parametric processes in a strong-coupling planar microcavity," *Phys. Rev. B*, vol. 63, p. 193305, Apr 2001.

[83] D. S. Bethune, "Optical harmonic generation and mixing in multilayer media: analysis using optical transfer matrix techniques," *J. Opt. Soc. Am. B*, vol. 6, no. 5, pp. 910–916, May 1989.

[84] X. Liu, A. Rose, E. Poutrina, C. Ciracì, S. Larouche, and D. R. Smith, "Surfaces, films, and multilayers for compact nonlinear plasmonics," *J. Opt. Soc. Am. B*, vol. 30, no. 11, pp. 2999–3010, Nov 2013.

[85] S. Larouche and D. R. Smith, "A retrieval method for nonlinear metamaterials," *Optics Communications*, vol. 283, no. 8, pp. 1621–1627, 2010, nonlinear Optics in Metamaterials.

[86] A. Rose, S. Larouche, D. Huang, E. Poutrina, and D. R. Smith, "Nonlinear parameter retrieval from three- and four-wave mixing in metamaterials," *Phys. Rev. E*, vol. 82, p. 036608, Sep 2010.

[87] P. Yeh, *Optical waves in layered media*. Wiley New York, 1988, vol. 95.

[88] M. Born and E. Wolf, *Principles of optics: electromagnetic theory of propagation, interference and diffraction of light*. Cambridge university press, 1999.

[89] L. A. A. Pettersson, L. S. Roman, and O. Inganäs, "Modeling photocurrent action spectra of photovoltaic devices based on organic thin films," *Journal of Applied Physics*, vol. 86, no. 1, pp. 487–496, 1999.

[90] N. Bloembergen and P. S. Pershan, "Light waves at the boundary of nonlinear media," *Phys. Rev.*, vol. 128, pp. 606–622, Oct 1962.

[91] J.-H. Song, Y. He, A. V. Nurmikko, J. Tischler, and V. Bulovic, "Exciton-polariton dynamics in a transparent organic semiconductor microcavity," *Phys. Rev. B*, vol. 69, p. 235330, Jun 2004.

[92] P. G. Savvidis, L. G. Connolly, M. S. Skolnick, D. G. Lidzey, and J. J. Baumberg, "Ultrafast polariton dynamics in strongly coupled zinc porphyrin microcavities at room temperature," *Phys. Rev. B*, vol. 74, p. 113312, Sep 2006.

[93] L. R. Dalton, P. A. Sullivan, and D. H. Bale, "Electric field poled organic electro-optic materials: State of the art and future prospects," *Chemical Reviews*, vol. 110, no. 1, pp. 25–55, 2010.

[94] A. D. Rakić, A. B. Djurišić, J. M. Elazar, and M. L. Majewski, "Optical properties of metallic films for vertical-cavity optoelectronic devices," *Appl. Opt.*, vol. 37, no. 22, pp. 5271–5283, Aug 1998.

[95] C. Ciuti, P. Schwendimann, B. Deveaud, and A. Quattropani, "Theory of the angle-resonant polariton amplifier," *Phys. Rev. B*, vol. 62, pp. R4825–R4828, Aug 2000.

[96] Y. R. Shen, *Principles of nonlinear optics*. Wiley-Interscience, New York, NY, USA, 1984.

[97] S. Buckley, M. Radulaski, K. Biermann, and J. Vučković, "Second harmonic generation in photonic crystal cavities in (111)-oriented gaas," *Applied Physics Letters*, vol. 103, no. 21, pp. –, 2013.

[98] S. Buckley, M. Radulaski, J. L. Zhang, J. Petykiewicz, K. Biermann, and J. Vučković, "Multimode nanobeam cavities for nonlinear optics: high quality resonances separated by an octave," *Opt. Express*, vol. 22, no. 22, pp. 26 498–26 509, Nov 2014.

[99] Y. Chen, A. Tredicucci, and F. Bassani, "Bulk exciton polaritons in gaas microcavities," *Phys. Rev. B*, vol. 52, pp. 1800–1805, Jul 1995.

[100] S. Adachi, "Gaas, alas, and alxga1-xas: Material parameters for use in research and device applications," *Journal of Applied Physics*, vol. 58, no. 3, pp. R1–R29, 1985.

[101] J. A. Fülöp, L. Pálfalvi, G. Almási, and J. Hebling, "Design of high-energy terahertz sources based on optical rectification," *Opt. Express*, vol. 18, no. 12, pp. 12 311–12 327, Jun 2010.

[102] I. B. Burgess, A. W. Rodriguez, M. W. McCutcheon, J. Bravo-Abad, Y. Zhang, S. G. Johnson, and M. Lončar, "Difference-frequency generation with quantum-limited efficiency in triply-resonant nonlinear cavities," *Opt. Express*, vol. 17, no. 11, pp. 9241–9251, May 2009.

[103] D. M. Ramirez, A. W. Rodriguez, H. Hashemi, J. D. Joannopoulos, M. Soljačić, and S. G. Johnson, "Degenerate four-wave mixing in triply resonant kerr cavities," *Phys. Rev. A*, vol. 83, p. 033834, Mar 2011.

[104] Z. Lin, T. Alcorn, M. Lončar, S. G. Johnson, and A. W. Rodriguez, "High-efficiency degenerate four-wave mixing in triply resonant nanobeam cavities," *Phys. Rev. A*, vol. 89, p. 053839, May 2014.

[105] F. Herrera and F. C. Spano, "Cavity-controlled chemistry in molecular ensembles," *Phys. Rev. Lett.*, vol. 116, p. 238301, Jun 2016.

[106] J. Galego, F. J. Garcia-Vidal, and J. Feist, "Cavity-induced modifications of molecular structure in the strong-coupling regime," *Phys. Rev. X*, vol. 5, p. 041022, Nov 2015.

[107] J. M. Hales, J. Matichak, S. Barlow, S. Ohira, K. Yesudas, J.-L. Brédas, J. W. Perry, and S. R. Marder, "Design of polymethine dyes with large third-order optical nonlinearities and loss figures of merit," *Science*, vol. 327, no. 5972, pp. 1485–1488, 2010.

[108] S. Barlow, J.-L. Bredas, Y. A. Getmanenko, R. L. Gieseking, J. M. Hales, H. Kim, S. R. Marder, J. W. Perry, C. Risko, and Y. Zhang, "Polymethine materials with solid-state third-order optical susceptibilities suitable for all-optical signal-processing applications," *Mater. Horiz.*, vol. 1, pp. 577–581, 2014.

[109] S. Hafezian, K. Maloney, J. Lefebvre, L. Martinu, and S. Kéna-Cohen, "Continuous ultrathin silver films deposited on sio2 and sinx using a self-assembled monolayer," *Applied Physics Letters*, vol. 109, no. 12, p. 121603, 2016.

[110] P. A. Hobson, W. L. Barnes, D. G. Lidzey, G. A. Gehring, D. M. Whittaker, M. S. Skolnick, and S. Walker, "Strong exciton-photon coupling in a low-q all-metal mirror microcavity," *Applied Physics Letters*, vol. 81, no. 19, pp. 3519–3521, 2002.

[111] S. Kéna-Cohen and S. R. Forrest, "Giant davydov splitting of the lower polariton branch in a polycrystalline tetracene microcavity," *Phys. Rev. B*, vol. 77, p. 073205, Feb 2008.

[112] R. Houdré, R. P. Stanley, and M. Ilegems, "Vacuum-field rabi splitting in the presence of inhomogeneous broadening: Resolution of a homogeneous linewidth in an inhomogeneously broadened system," *Phys. Rev. A*, vol. 53, pp. 2711–2715, Apr 1996.

[113] M. R. Shcherbakov, D. N. Neshev, B. Hopkins, A. S. Shorokhov, I. Staude, E. V. Melik-Gaykazyan, M. Decker, A. A. Ezhov, A. E. Miroshnichenko, I. Brener, A. A. Fedyanin, and Y. S. Kivshar, "Enhanced third-harmonic generation in silicon nanoparticles driven by magnetic response," *Nano Letters*, vol. 14, no. 11, pp. 6488–6492, 2014, pMID: 25322350.

[114] G. Ramos-Ortiz, M. Cha, S. Thayumanavan, J. C. Mendez, S. R. Marder, and B. Kippelen, "Third-order optical autocorrelator for time-domain operation at telecommunication wavelengths," *Applied Physics Letters*, vol. 85, no. 2, pp. 179–181, 2004.

[115] G. Grinblat, Y. Li, M. P. Nielsen, R. F. Oulton, and S. A. Maier, "Enhanced third harmonic generation in single germanium nanodisks excited at the anapole mode," *Nano Letters*, vol. 16, no. 7, pp. 4635–4640, 2016, pMID: 27331867.

[116] S. Salinas, *Introduction to Statistical Physics*, ser. Graduate Texts in Contemporary Physics. Springer New York, 2010.

[117] M. H. Anderson, J. R. Ensher, M. R. Matthews, C. E. Wieman, and E. A. Cornell, "Observation of bose-einstein condensation in a dilute atomic vapor," *Science*, vol. 269, no. 5221, pp. 198–201, 1995.

[118] C. P. Dietrich, A. Steude, L. Tropf, M. Schubert, N. M. Kronenberg, K. Ostermann, S. Höfling, and M. C. Gather, "An exciton-polariton laser based on biologically produced fluorescent protein," *Science Advances*, vol. 2, no. 8, 2016.

[119] T. J. S. Evans, A. Schlaus, Y. Fu, X. Zhong, T. L. Atallah, M. S. Spencer, L. E. Brus, S. Jin, and X.-Y. Zhu, "Continuous-wave lasing in cesium lead bromide perovskite nanowires," *Advanced Optical Materials*, vol. 6, no. 2, p. 1700982, 2018.

[120] R. Su, C. Diederichs, J. Wang, T. C. H. Liew, J. Zhao, S. Liu, W. Xu, Z. Chen, and Q. Xiong, "Room-temperature polariton lasing in all-inorganic perovskite nanoplatelets," *Nano Letters*, vol. 17, no. 6, pp. 3982–3988, 2017.

[121] K. S. Daskalakis, S. A. Maier, and S. Kéna-Cohen, "Spatial coherence and stability in a disordered organic polariton condensate," *Phys. Rev. Lett.*, vol. 115, p. 035301, Jul 2015.

[122] S. Orfanidis, "Electromagnetic waves and antennas; sophocles j," 2004.

[123] K. F. Mak and J. Shan, "Photonics and optoelectronics of 2d semiconductor transition metal dichalcogenides," *Nature Photonics*, vol. 10, no. 4, pp. 216–226, 2016.

[124] M. Sidler, P. Back, O. Cotlet, A. Srivastava, T. Fink, M. Kroner, E. Demler, and A. Imamoglu, "Fermi polaron-polaritons in charge-tunable atomically thin semiconductors," *Nature Physics*, vol. 13, no. 3, p. 255, 2017.

[125] L. C. Flatten, D. M. Coles, Z. He, D. G. Lidzey, R. A. Taylor, J. H. Warner, and J. M. Smith, "Electrically tunable organic–inorganic hybrid polaritons with monolayer WS_2," *Nature communications*, vol. 8, p. 14097, 2017.

[126] Z. Sun, J. Gu, A. Ghazaryan, Z. Shotan, C. R. Considine, M. Dollar, B. Chakraborty, X. Liu, P. Ghaemi, S. Kéna-Cohen *et al.*, "Optical control of room-temperature valley polaritons," *Nature Photonics*, vol. 11, no. 8, p. 491, 2017.

[127] S. Dufferwiel, S. Schwarz, F. Withers, A. Trichet, F. Li, M. Sich, O. Del Pozo-Zamudio, C. Clark, A. Nalitov, D. Solnyshkov *et al.*, "Exciton-polaritons in van der waals heterostructures embedded in tunable microcavities," *Nature communications*, vol. 6, 2015.

[128] X. Liu, T. Galfsky, Z. Sun, F. Xia, E.-c. Lin, Y.-H. Lee, S. Kéna-Cohen, and V. M. Menon, "Strong light-matter coupling in two-dimensional atomic crystals," *Nature Photonics*, vol. 9, no. 1, pp. 30–34, 2015.

[129] L. C. Flatten, Z. He, D. M. Coles, A. A. Trichet, A. W. Powell, R. A. Taylor, J. H. Warner, and J. M. Smith, "Room-temperature exciton-polaritons with two-dimensional WS_2," *Scientific reports*, vol. 6, 2016.

[130] S. Wang, S. Li, T. Chervy, A. Shalabney, S. Azzini, E. Orgiu, J. A. Hutchison, C. Genet, P. Samorì, and T. W. Ebbesen, "Coherent coupling of WS_2 monolayers with metallic photonic nanostructures at room temperature," *Nano Letters*, vol. 16, no. 7, pp. 4368–4374, 2016, pMID: 27266674.

[131] W. Liu, B. Lee, C. H. Naylor, H.-S. Ee, J. Park, A. T. C. Johnson, and R. Agarwal, "Strong exciton-plasmon coupling in MoS_2 coupled with plasmonic lattice," *Nano Letters*, vol. 16, no. 2, pp. 1262–1269, 2016, pMID: 26784532.

[132] N. Lundt, S. Klembt, E. Cherotchenko, S. Betzold, O. Iff, A. V. Nalitov, M. Klaas, C. P. Dietrich, A. V. Kavokin, S. Höfling *et al.*, "Room-temperature tamm-plasmon exciton-polaritons with a WSe_2 monolayer," *Nature communications*, vol. 7, 2016.

[133] L. Zhang, R. Gogna, W. Burg, E. Tutuc, and H. Deng, "Photonic-crystal exciton-polaritons in monolayer semiconductors," *Nature communications*, vol. 9, no. 1, p. 713, 2018.

[134] Y. Li, A. Chernikov, X. Zhang, A. Rigosi, H. M. Hill, A. M. van der Zande, D. A. Chenet, E.-M. Shih, J. Hone, and T. F. Heinz, "Measurement of the optical dielectric function of monolayer transition-metal dichalcogenides: MoS_2, $MoSe_2$, WS_2, and WSe_2," *Phys. Rev. B*, vol. 90, p. 205422, Nov 2014.

[135] H. R. Gutiérrez, N. Perea-López, A. L. Elías, A. Berkdemir, B. Wang, R. Lv, F. López-Urías, V. H. Crespi, H. Terrones, and M. Terrones, "Extraordinary room-temperature photoluminescence in triangular WS_2 monolayers," *Nano Letters*, vol. 13, no. 8, pp. 3447–3454, 2013, pMID: 23194096.

[136] B. Zhu, X. Chen, and X. Cui, "Exciton binding energy of monolayer WS_2," *Scientific reports*, vol. 5, 2015.

[137] C. Cong, J. Shang, Y. Wang, and T. Yu, "Optical properties of 2d semiconductor WS_2," *Advanced Optical Materials*, vol. 6, no. 1, pp. 1 700 767–n/a, 2018, 1700767.

[138] L. Yuan and L. Huang, "Exciton dynamics and annihilation in WS_2 2d semiconductors," *Nanoscale*, vol. 7, pp. 7402–7408, 2015.

[139] Y. Hoshi, T. Kuroda, M. Okada, R. Moriya, S. Masubuchi, K. Watanabe, T. Taniguchi, R. Kitaura, and T. Machida, "Suppression of exciton-exciton annihilation in tungsten disulfide monolayers encapsulated by hexagonal boron nitrides," *Phys. Rev. B*, vol. 95, p. 241403, Jun 2017.

[140] G. Scuri, Y. Zhou, A. A. High, D. S. Wild, C. Shu, K. De Greve, L. A. Jauregui, T. Taniguchi, K. Watanabe, P. Kim, M. D. Lukin, and H. Park, "Large excitonic reflectivity of monolayer mose$_2$ encapsulated in hexagonal boron nitride," *Phys. Rev. Lett.*, vol. 120, p. 037402, Jan 2018.

[141] A. Amo, T. Liew, C. Adrados, R. Houdré, E. Giacobino, A. Kavokin, and A. Bramati, "Exciton–polariton spin switches," *Nature Photonics*, vol. 4, no. 6, p. 361, 2010.

[142] T. Espinosa-Ortega and T. C. H. Liew, "Complete architecture of integrated photonic circuits based on and and not logic gates of exciton polaritons in semiconductor microcavities," *Phys. Rev. B*, vol. 87, p. 195305, May 2013.

[143] C. Sturm, D. Tanese, H. Nguyen, H. Flayac, E. Galopin, A. Lemaître, I. Sagnes, D. Solnyshkov, A. Amo, G. Malpuech *et al.*, "All-optical phase modulation in a cavity-polariton mach–zehnder interferometer," *Nature communications*, vol. 5, p. 3278, 2014.

[144] A. Angelini, E. Barakat, P. Munzert, L. Boarino, N. De Leo, E. Enrico, F. Giorgis, H. P. Herzig, C. F. Pirri, and E. Descrovi, "Focusing and extraction of light mediated by bloch surface waves," *Scientific reports*, vol. 4, 2014.

[145] M. Held, A. Graf, Y. Zakharko, P. Chao, L. Tropf, M. C. Gather, and J. Zaumseil, "Ultrastrong coupling of electrically pumped near-infrared exciton-polaritons in high mobility polymers," *Advanced Optical Materials*, vol. 6, no. 3, p. 1700962.

[146] A. Graf, M. Held, Y. Zakharko, L. Tropf, M. C. Gather, and J. Zaumseil, "Electrical pumping and tuning of exciton-polaritons in carbon nanotube microcavities," *Nature materials*, vol. 16, no. 9, p. 911, 2017.

[147] L. Karvonen, A. Säynätjoki, S. Mehravar, R. D. Rodriguez, S. Hartmann, D. R. Zahn, S. Honkanen, R. A. Norwood, N. Peyghambarian, K. Kieu *et al.*, "Investigation of second-and third-harmonic generation in few-layer gallium selenide by multiphoton microscopy," *Scientific reports*, vol. 5, p. 10334, 2015.

[148] A. Autere, H. Jussila, A. Marini, J. R. M. Saavedra, Y. Dai, A. Säynätjoki, L. Karvonen, H. Yang, B. Amirsolaimani, R. A. Norwood, N. Peyghambarian, H. Lipsanen, K. Kieu, F. J. G. de Abajo, and Z. Sun, "Optical harmonic generation in monolayer group-vi transition metal dichalcogenides," *Phys. Rev. B*, vol. 98, p. 115426, Sep 2018.

[149] H. G. Rosa, H. Y. Wei, I. Verzhbitskiy, M. J. Rodrigues, T. Taniguchi, K. Watanabe, G. Eda, V. M. Pereira, and J. C. Gomes, "Characterization of the second-and

third-harmonic optical susceptibilities of atomically thin tungsten diselenide," *Scientific reports*, vol. 8, p. 10035, 2018.

[150] Y.-Y. Lai, Y.-H. Chou, Y.-P. Lan, T.-C. Lu, S.-C. Wang, and Y. Yamamoto, "Crossover from polariton lasing to exciton lasing in a strongly coupled zno microcavity," *Scientific reports*, vol. 6, p. 20581, 2016.

[151] P. Cristofolini, G. Christmann, S. I. Tsintzos, G. Deligeorgis, G. Konstantinidis, Z. Hatzopoulos, P. G. Savvidis, and J. J. Baumberg, "Coupling quantum tunneling with cavity photons," *Science*, vol. 336, no. 6082, pp. 704–707, 2012.

[152] A. V. Nalitov, D. D. Solnyshkov, N. A. Gippius, and G. Malpuech, "Voltage control of the spin-dependent interaction constants of dipolaritons and its application to optical parametric oscillators," *Phys. Rev. B*, vol. 90, p. 235304, Dec 2014.

[153] E. Calman, M. Fogler, L. Butov, S. Hu, A. Mishchenko, and A. Geim, "Indirect excitons in van der waals heterostructures at room temperature," *Nature communications*, vol. 9, no. 1, p. 1895, 2018.

[154] V. Walther, R. Johne, and T. Pohl, "Giant optical nonlinearities from rydberg excitons in semiconductor microcavities," *Nature communications*, vol. 9, no. 1, p. 1309, 2018.

[155] W. Bao, X. Liu, F. Zheng, Y. Xia, M. Zhao, J. Kim, S. Yang, Y. Wang, Y. Wang, L.-W. Wang *et al.*, "Observation of solid state rydberg exciton polariton and its condensate in a perovskite cavity," *arXiv preprint arXiv:1803.07282*, 2018.

[156] J. Gu, A. Boehmke, R. Koots, and V. M. Menon, "Observation of rydberg exciton-polaritons in 2d transition metal dichalcogenides," in *Conference on Lasers and Electro-Optics*. Optical Society of America, 2018, p. FM2F.6.

APPENDIX A EXPERIMENTAL SETUP

A simplified schematic of the experimental setup is shown in Figure A.1. Steering mirrors and positioning stages have been omitted for clarity.

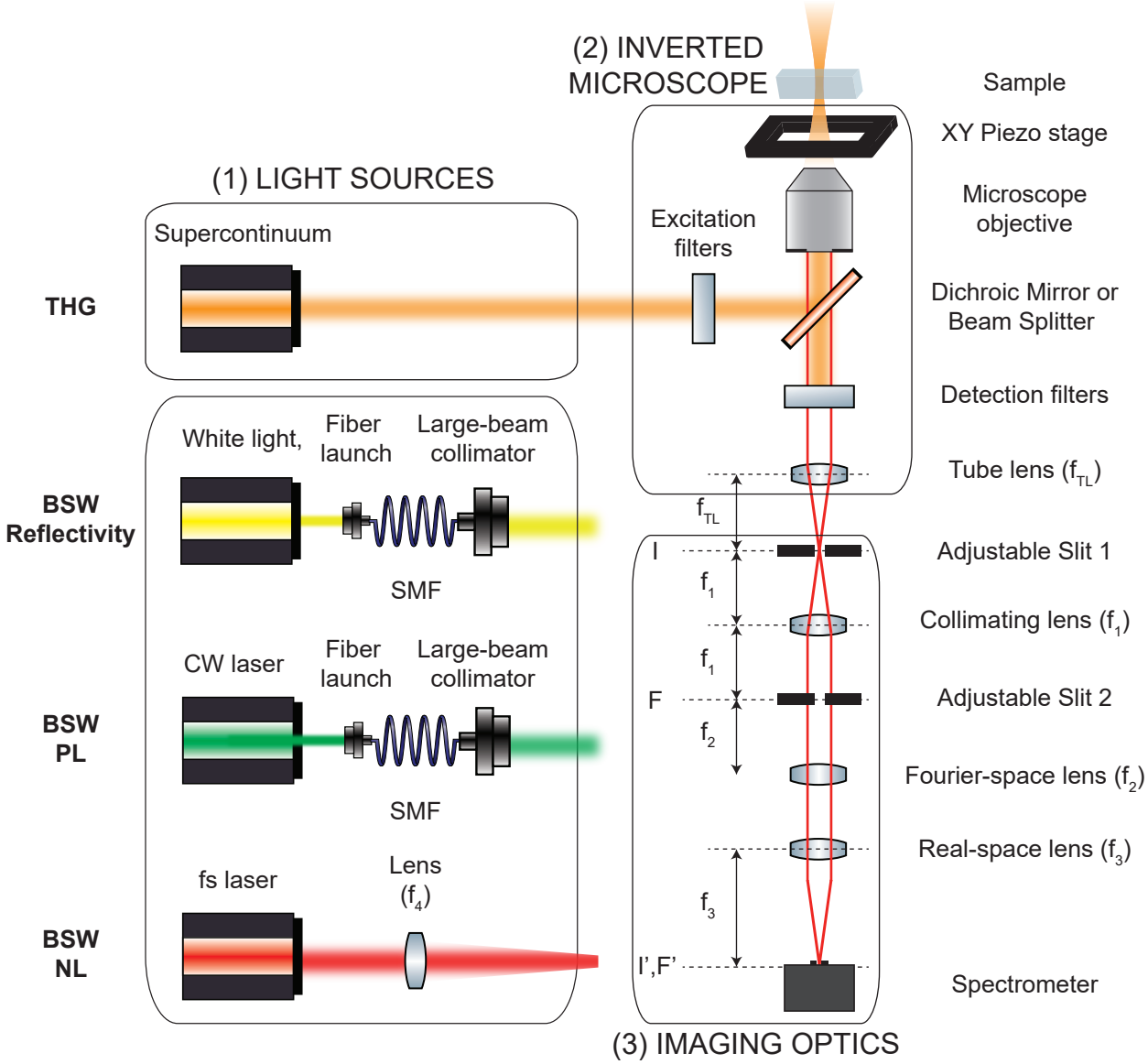

Figure A.1 Experimental setup. Steering mirrors and positioning stages not shown.

As indicated by rounded boxes in Fig. A.1, the experimental setup can be split into three sections based on their individual purposes: (1) light source, (2) inverted microscope and (3)

imaging optics. First, we will describe the configurations common to all experiments. Then, we will focus on specific details for the measurements described in Chapter 4 (third-harmonic generation) and in Chapter 6 (Bloch surface wave polaritons). Unless indicated otherwise, all optical components were purchased from Thorlabs.

A.1 General experimental setup

A.1.1 Light source

Large-beam collimator: Where indicated, a large area Gaussian collimator (SLT, LB20) was used following spatial filtering. The collimator has low wavefront aberration ($< \lambda/10$) and a large beam diameter of 13 mm ($1/e^2$ in intensity).

A.1.2 Inverted microscope

Unless indicated otherwise, an Olympus IX-81 inverted microscope was used. Tube lens focal length is $f_{TL} = 18$ cm. The sample is mounted on a computer controlled precision XY piezo stage (P-545.2C7, PInano) with a lateral scanning range of 200 μm $\times$ 200 μm and sub-nanometer resolution. This stage is itself mounted on an open-frame microscope stage with a manual linear travel range of 25 mm $\times$ 25 mm. A custom made LabVIEW software is responsible for controlling the movement of the stage when needed.

A.1.3 Imaging optics

A two-inch achromatic doublet lens ($f_1 = 20$) was used as a collimating lens. It was placed one focal length away from the first image plane (I) and generated the first Fourier plane (F) one focal length afterward. A two-inch achromatic doublet lens ($f_3 = 30$ cm) was then used to recreate the image plane (I') onto the slit of an imaging spectrometer (IsoPlane 160, Princeton Instruments). The spectrometer is equipped with a CCD camera (PIXIS400, Princeton Instruments) with 1340$\times$400 pixels (20 μm $\times$ 20 μm) and offers a high spectral resolution of 0.15 nm. Grating: 300 gr/mm and blaze wavelength of 500 nm. Where indicated, adjustable slits for real- and momentum-space imaging were placed on their respective first focal planes.

A.2 Third-harmonic measurements

A.2.1 Light source

A supercontinuum laser (Fianium FemtoPower 1060, 40 MHz) was used as the broad infrared light source. The pulse duration was measured with a streak camera (Hamamatsu C10910) and found to be 48 ps.

A.2.2 Inverted microscope

Objective: Olympus LUCPlanFl 40× 0.6 NA with the correction collar set to zero.

Filters: A different set of excitation, beam splitter and detection filters was used for each fundamental wavelength. 1320 nm: Excitation: LP1250, BP1320-12, SP1500 (Edmund Optics), 1 cm quartz cuvette with toluene; Beam splitter: BSW29R; Detection: SP950, BP430-20 (Chroma), 1 cm quartz cuvette with water. 1550 nm: Excitation: LP1250, LP1500, BP1550-12, 1 cm quartz cuvette with toluene; Beam splitter: BSW29R; Detection: SP1500. 1650 nm: Excitation: LP1250, LP1500, BP1650-12; Beam splitter: FF538-FDi01 (Semrock); Detection: 1 cm cuvette with toluene. The transmission of all detection filters was measured and used to calibrate the measured powers.

A.3 Bloch surface wave measurements

A.3.1 Light source

BSW Reflectivity: White light source: EQ-99X (Energetiq); Single-mode fiber: P1-630A-FC.

BSW PL: CW Laser: 514 nm diode (L520P50/LTC56B); Single-mode fiber: P1-405B-FC.

BSW NL: A tunable femtosecond laser (estimated pulse width of 145 fs, repetition rate 10 kHz) was focused onto the BFP of the microscope objective with a long focal length lens ($f_4 = 75$ cm).

A.3.2 Inverted microscope

Microscope For resonant and nonlinear measurements, a home built microscope was used with the same lenses as before, except for a 20 cm tube lens.

Objective: For reflectivity and non-resonant measurements: Olympus PlanAPO N 60× 1.42 NA. For resonant and nonlinear measurements: Olympus APO N 60× 1.49 NA.

Filters: For reflectivity measurements: Excitation: LP550; Beam splitter: BSW29R; Detection: SP700. For PL measurements: Excitation: RPE520SP (Omega); Dichroic: FF538-FDi01 (Semrock); Detection: FELH0550.

A.3.3 Imaging optics

Momentum-space imaging: A two-inch achromatic doublet lens ($f_2 = 7.5$ cm) was inserted one focal length in front of the first Fourier plane.

Slits: For propagation measurements, adjustable slit (2) were placed in the BFP to select only the lower polariton mode and adjustable slit (1) in the image plane to block the excitation spot (in the resonant case only).

APPENDIX B THIRD-HARMONIC POWER CALIBRATION

Third-harmonic measurements were performed from the excitation side (in reflection) with the CCD camera. The calibration procedure was performed with a 532 nm laser (supercontinuum followed by BP532-3, SP700, SP1500, 1 cm cuvette with toluene). The laser was focused on a 75 nm thick silver mirror and the reflected light was measured at the side-port of the microscope with a power meter (S120VC/PM100D). Neutral-density filters with measured transmission values at 532 nm were inserted in the excitation path so that the powers at the side-port of the microscope could be adjusted in the range of $10^{-13} - 10^{-10}$ W.

For each power value, a series of images was acquired with the CCD camera and the corresponding integrated counts on two adjacent 30×30 pixel regions were obtained, the first one including the laser spot and the second one only background light. The procedure was repeated for different integration times and the detector response was obtained by fitting the background-corrected counts over the known input power to a fourth-degree polynomial in integration time.

The CCD quantum efficiency is taken to remain constant in the range of THG wavelengths from 440 nm to 550 nm. The collection efficiency of the objective from the excitation side based on the detection solid angle was estimated to be $\eta = 1 - \cos\left[\sin^{-1}(NA)\right] = 0.2$. This value only affects absolute powers, but not the enhancement factors.

APPENDIX C LIST OF PUBLICATIONS AND CONFERENCES

C.1 Publications

1. **F. Barachati**, A. Fieramosca, S. Hafezian, J. Gu, B. Chakraborty, D. Ballarini, L. Martinu, V. Menon, D. Sanvitto, and S. Kéna-Cohen. "Interacting polariton fluids in a monolayer of tungsten disulfide", Nature Nanotechnology, 2018. doi:10.1038/s41565-018-0219-7.

2. J. Brodeur, R. Arguel, S. Hafezian, **F. Barachati**, and S. Kéna-Cohen. "Nearly 40% outcoupling efficiency in OLEDs with all-metal electrodes", Applied Physics Letters, 113, 041105, 2018.

3. E. Eizner, J. Brodeur, **F. Barachati**, A. Sridharan, and S. Kéna-Cohen. "Organic photodiodes with an extended responsivity using ultrastrong light-matter coupling", ACS Photonics, 5 (7), p. 2921-2927, 2018.

4. G. Lerario, A. Fieramosca, **F. Barachati**, D. Ballarini, K. S. Daskalakis, L. Dominici, M. De Giorgi, S. A. Maier, G. Gigli, S. Kéna-Cohen, and D. Sanvitto. "Room-temperature superfluidity in a polariton condensate", Nature Physics, vol. 13, no. 9, p. 837, 2017.

5. **F. Barachati**, J. Simon, Y. A. Getmanenko, S. Barlow, S. R. Marder, and S. Kéna-Cohen. "Tunable third-harmonic generation from polaritons in the ultrastrong coupling regime", ACS Photonics, vol. 5, no. 1, pp. 119–125, 2018.

6. **F. Barachati**, S. De Liberato, and S. Kéna-Cohen. "Generation of rabi-frequency radiation using exciton-polaritons", Phys. Rev. A, vol. 92, p. 033828, Sep 2015.

C.2 Conferences: contributed talks

1. **F. Barachati**, A. Fieramosca, S. Hafezian, J. Gu, B. Chakraborty, D. Ballarini, L. Martinu, V. Menon, D. Sanvitto, and S. Kéna-Cohen. "Interacting polariton fluids in a monolayer of tungsten disulfide", 9th International Conference on Spontaneous Coherence on Excitonic Systems (ICSCE9), Montréal, CA, 2018.

2. **F. Barachati**, A. Fieramosca, S. Hafezian, J. Gu, B. Chakraborty, D. Ballarini, L. Martinu, V. Menon, D. Sanvitto, and S. Kéna-Cohen. "Interacting polariton fluids in

a monolayer of tungsten disulfide", Conference on Lasers and Electro-Optics (CLEO), San José, USA, 2018.

3. **F. Barachati**, J. Simon, Y. Getmanenko, S. Barlow, S. R. Marder, and S. Kéna-Cohen. "Tunable third-harmonic generation from polaritons in the ultrastrong coupling regime", 12th International Conference on Optical Probes of Organic and Hybrid Semiconductors, Québec city, Canada, 2017.

C.3 Conferences: posters

1. **F. Barachati**, J. Simon, Y. Getmanenko, S. Barlow, S. R. Marder, and S. Kéna-Cohen. "Ultrastrong coupling in a nonlinear organic microcavity", 1st International Workshop on Strong Coupling with Organic Molecules, San Sebastian, Spain, 2016.

2. **F. Barachati**, S. Liberato, and S. Kéna-Cohen. "Generation of Rabi frequency radiation using exciton-polaritons", 1st International Workshop on Strong Coupling with Organic Molecules, San Sebastian, Spain, 2016.

3. **F. Barachati**, S. Liberato, and S. Kéna-Cohen. "Generation of Rabi frequency radiation using exciton-polaritons", RQMP Annual Meeting on Quantum Materials and Quantum Information, Sherbrooke, Canada, 2016.

4. **F. Barachati**, S. Liberato, and S. Kéna-Cohen. "Generation of Rabi frequency radiation using exciton-polaritons", 11th International Conference on Excitonic and Photonic Processes in Condensed Matter and Nano Materials, Montréal, Canada, 2015.